UNICAMP

UNIVERSIDADE ESTADUAL DE CAMPINAS

Faculdade de Engenharia Mecânica

CARLOS AZAEL ALVAREZ ZAMBRANO

Genesis and formation of subaqueous barchan dunes: from a morphological characterization to a description at the grain scale

Gênese e formação de dunas barcanas subaquáticas: de uma caracterização morfológica a uma descrição na escala dos grãos

CAMPINAS
2020

CARLOS AZAEL ALVAREZ ZAMBRANO

Genesis and formation of subaqueous barchan dunes: from a morphological characterization to a description at the grain scale

Gênese e formação de dunas barcanas subaquáticas: de uma caracterização morfológica a uma descrição na escala dos grãos

Thesis presented to the School of Mechanical Engineering of the University of Campinas in partial fulfillment of the requirements for the degree of Doctor in Mechanical Engineering in the area of Thermal and Fluids.

Tese apresentada à Faculdade de Engenharia Mecânica da Universidade Estadual de Campinas como parte dos requisitos exigidos para a obtenção do título de Doutor em Engenharia Mecânica, na Área de Térmica e Fluidos.

Supervisor: Prof. Dr. Erick de Moraes Franklin

ESTE EXEMPLAR CORRESPONDE À VERSÃO FINAL DA TESE DEFENDIDA PELO ALUNO CARLOS AZAEL ALVAREZ ZAMBRANO, E ORIENTADO PELO PROF. DR. ERICK DE MORAES FRANKLIN

....

ASSINATURA DO ORIENTADOR

CAMPINAS
2020

Ficha catalográfica
Universidade Estadual de Campinas
Biblioteca da Área de Engenharia e Arquitetura
Luciana Pietrosanto Milla - CRB 8/8129

AL86g	Alvarez Zambrano, Carlos Azael, 1982- Genesis and formation of subaqueous barchan dunes : from a morphological characterization to a description at the grain scale / Carlos Azael Alvarez Zambrano. – Campinas, SP : [s.n.], 2020. Orientador: Erick de Moraes Franklin. Tese (doutorado) – Universidade Estadual de Campinas, Faculdade de Engenharia Mecânica. 1. Escoamento turbulento. 2. Materiais granulares. 3. Dunas. 4. Processamento de imagens. I. Franklin, Erick de Moraes, 1974-. II. Universidade Estadual de Campinas. Faculdade de Engenharia Mecânica. III. Título.

Informações para Biblioteca Digital

Título em outro idioma: Gênese e formação de dunas barcanas subaquáticas : de uma caracterização morfológica a uma descrição na escala dos grãos
Palavras-chave em inglês:
Turbulent flow
Granular materials
Dunes
Image processing
Área de concentração: Térmica e Fluídos
Titulação: Doutor em Engenharia Mecânica
Banca examinadora:
Erick de Moraes Franklin [Orientador]
Hans Jürgen Herrmann
Francisco Ricardo da Cunha
Guilherme Henrique Fiorot
Marcelo Souza de Castro
Data de defesa: 06-03-2020
Programa de Pós-Graduação: Engenharia Mecânica

Identificação e informações acadêmicas do(a) aluno(a)
- ORCID do autor: https://orcid.org/0000-0002-7270-5240
- Currículo Lattes do autor: http://lattes.cnpq.br/8971522184232237

UNIVERSIDADE ESTADUAL DE CAMPINAS

FACULDADE DE ENGENHARIA MECÂNICA

TESE DE DOUTORADO

Genesis and formation of subaqueous barchan dunes: from a morphological characterization to a description at the grain scale

Gênese e formação de dunas barcanas subaquáticas: de uma caracterização morfológica a uma descrição na escala dos grãos

Autor: Carlos Azael Alvarez Zambrano
Orientador: Erick de Moraes Franklin

A Banca Examinadora composta pelos membros abaixo aprovou esta Tese:

Prof. Dr. Erick de Moraes Franklin
DE/FEM/UNICAMP

Prof. Dr. Hans Jürgen Herrmann
PMMH/École Supérieure de Physique et de Chimie Industrielles - ESPCI

Prof. Dr. Francisco Ricardo da Cunha
ENM/FT/UnB

Prof. Dr. Guilherme Henrique Fiorot
DEMEC/EE/UFRGS

Prof. Dr. Marcelo Souza de Castro
DE/FEM/UNICAMP

A ata da defesa com as respectivas assinaturas dos membros encontra-se no processo de vida acadêmica do aluno.

Campinas, 06 de Março de 2020.

Dedication

To my dear parents Carlos and Jenny
To my siblings Gina and Jimmy.
To my nephews Emilito and Brunito.
To my little friend Rocky(†).

Carlos

Acknowledgments

I am very grateful to many important people and institutions without whom this thesis might not have been completed.

My deepest gratitude goes to my family. To my parents Carlos and Jenny, to my sister Gina and to my brother Jimmy for showing me that the family is the most essential in life.

To my supervisor Prof. Dr. Erick M. Franklin, not only for the opportunity to work with him but also for leading me to confirm that science is my passion and future. I truly appreciate his mentoring and friendship.

To *Secretaría de Educación Superior, Ciencia, Tecnología e Innovación* (SENESCYT, Ecuador) for the Grant No. 2013-AR2Q2850.

To *Conselho Nacional de Desenvolvimento Científico e Tecnológico* (CNPq, Brazil) for the Grant No. 140773/2016-9.

To *Fundação de Amparo à Pesquisa do Estado de São Paulo* (FAPESP, Brazil), to *Coordenação de Aperfeiçoamento de Pessoal de Nível Superior* (CAPES, Brazil), and to *Fundo de Apoio ao Ensino, à Pesquisa e Extensão* (FAEPEX/UNICAMP) for the financial support provided.

To Prof. Dr. J. M. Floryan for his mentoring during my internship at the University of Western Ontario.

To *Emerging Leaders in the Americas Program* (ELAP), Global Affairs Canada, for the scholarship provided.

To the members of the Thesis Defense Committee for their valuable and knowledgeable feedback.

To the reviewers of our published papers for their invested comments.

To José Luis Dávila, an extraordinary friend, for his invaluable friendship and continuous support.

To my friends and labmates David, Gabriel Meletti, and Karlo for their help and valuable suggestions.

To Brazil's people for taking me in as one more of them.

Resumo

Na morfodinâmica das dunas com forma crescente, conhecidas como barcanas, muitos aspectos complexos estão envolvidos. Esta tese analisa o crescimento das dunas do tipo barcana sob escoamentos turbulentos de água. Abordagens experimentais e numéricas são empregadas para identificar algumas características intrínsecas desses padrões granulares. Os resultados experimentais mostram a existência de tempos característicos para o surgimento e o equilíbrio das barcanas. Essas dunas são encontradas na natureza e na indústria. As escalas de comprimento e tempo vão do quilômetro e milênio em Marte, passando pelos 100 m e 1 ano nos desertos, até 10 cm e 1 minuto para as barcanas subaquáticas. Em todos os casos, a dinâmica é semelhante, mas as escalas são totalmente diferentes. Devido a que a característica única da duna barcana é a presença de suas extremidades, chamadas *horns*, este trabalho associa a escala de tempo para o aparecimento delas à formação da barcana inteira. Baseado em argumentos dimensionais, propõe-se uma escala de tempo para o crescimento das dunas. Posteriormente, usando um método de rastreamento na escala do grão, é demonstrado que a maioria dos grãos que formaram os *horns* vieram de regiões à montante, com um deslocamento médio da ordem do tamanho da duna. Os grãos que viajam para os *horns* têm deslocamentos transversais, por rolamento e deslizamento, que não são desprezíveis. Por fim, as descobertas obtidas experimentalmente são reproduzidas numericamente empregando as mesmas condições de contorno. Os resultados numéricos capturaram adequadamente a evolução da pilha inicial até uma duna barcana nas ambas escalas; do leito e do grão, com os mesmos tempos e comprimentos característicos observados nos experimentos. Todos os novos aspectos apresentados neste trabalho mudam a forma como tinha sido explicado o crescimento das barcanas subaquáticas, e representam um passo significativo na compreensão da formação das dunas barcanas.

Palavras-chave: Leito móvel, escoamento turbulento, duna barcana, graõs finos.

Abstract

In the morphodynamics of crescent-shaped dunes, known as barchans, many complex aspects are involved. This thesis addresses the growing of barchan dunes under turbulent water flows. Experimental and numerical approaches are employed to identify some intrinsic features of these bedforms. The experimental results show the existence of characteristic times for the appearance and equilibrium of the barchans. These dunes are found in both nature and industry. The length and time scales go from the kilometer and millennium on Mars, passing by the 100 m and 1 year on deserts, down to 10 cm and 1 minute for sand barchans in water. In all cases, the dynamics are similar, but the scales are entirely different. Because the unique feature of a barchan dune is its extremities, called horns, this work associates the time scale for the appearance of them to the formation of the whole barchan. Based on dimensional arguments, it is proposed a time scale for the growth of the dunes. Afterward, using a tracking method at the grain scale, it is demonstrated that most of the grains that formed the horns came from upstream regions with an average displacement of the order of the bedform size. The grains traveling to the horns have transverse displacements by rolling and sliding that are not negligible. In the last part, the findings retrieved from the experimental frame are reproduced numerically employing the same boundary conditions. The numerical results captured well the evolution of the initial pile toward a barchan dune in both the bedform and grain scales, with the same characteristic time and lengths observed in the experiments. All the new aspects presented in this work change how has been explained the growth of subaqueous barchans and represent a significant step toward understanding the formation of barchan dunes.

Keywords: Bed load, turbulent flow, barchan dune, fine grains.

Illustrations List

Table List

List of Symbols, Acronyms and Abbreviations

Latin characters

A	Coefficient for threshold velocity
B	Log Law constant
C	Dune celerity
C_D	Drag coefficient
C_s	Smagorinsky's constant
d	Grain diameter
F_{drag}	Drag force
g	Acceleration of gravity
Im	Impact number
Ga	Galileo number
k	Turbulent kinetic energy
L_h	Horn length
L_{drag}	Inertial length
L_{sat}	Saturation length
m_p	Particle mass
p	Pressure
px	Pixels
q_{sat}	Saturated flux
q	Sediment flux
R	Radius of initial pile
Re_*	Reynolds number based on friction velocity u_*
Re	Reynolds number
r_0	Initial position of the pile centroid
r_c	Instantaneous position of the pile centroid
S_{ij}	Strain-rate tensor
t	Time
t_c	Characteristic time

u_*	Friction velocity
u_{th}	Fluid threshold velocity
u_p	Particle velocity
V_p	Particle volume
W	Dune width

Greeks characters

δ_{ij}	Kronecker's delta
δ	Half–channel height
δ_ν	Viscous length scale
μ	Dynamic viscosity
ν	Raising torque
μ_T	Turbulent or eddy viscosity
ρ and ρ_f	Fluid density
ρ_s	Grain density
κ	von Kármán constant
σ	Poison ratio
τ	Shear stress
θ	Shields number
Δ	Filter size

Superscripts

$()'$	Reynolds fluctuation
$()^+$	Property normalized by viscous scales
$\vec{\vec{()}}$	Tensor
$\vec{()}$	Vector

Acronyms and Abbreviations

CCD	Charged Coupled Device
CFD	Computational Fluid Dynamics
CMOS	Complementary Metal Oxide Semiconductor
DEM	Discrete Element Method
DNS	Direct Numerical Simulations
LED	Light Emitting Diode
LES	Large Eddy Simulation
LIGGGHTS	LAMMPS Improved for General Granular and Granular Heat Transfer Simulations
OpenFOAM	Open-source Field Operation And Manipulation
PDF	Probabilistic Density Function
PIV	Particle Image Velocimetry
PTV	Particle Tracking Velocimetry
RANS	Reynolds-Averaged Navier-Stokes
SGS	Subgrid Scale
WALE	Wall-Adapting Local Eddy-Viscosity
2D	Two Dimensional

CONTENTS

1 INTRODUCTION

This chapter presents a general overview of the sediment transport and of a type of sand dune, called barchan. Moreover, the research objectives are defined. Finally, the outline of the thesis is presented.

1.1 Background

The term *sediment* is employed either in natural sciences or engineering applications. In the first one, sediment refers to loose granular material at the Earth's surface that results from the weathering of rocky material entrained by wind or water or ice. In the engineering context, the word sediment is used to refer to particulate material transported in some system or flow device. The study of the transport of sediments in both natural and industrial applications is a complex subject, still poorly understood despite the longstanding effort of several researchers during the past few decades. Many patterns formed on the Earth are the direct result of the interaction fluid-sediment and can appear in different environments such as fluvial, coastal and aeolian. In engineering applications, it is common to observe particles entrained by fluids, for instance, in petroleum pipelines, or sewing and dredging systems.

As a result of the interaction between turbulent flows and a sand-covered surface, sand dunes can emerge and depending on the flow parameters and sand properties the formed patterns reach different sizes and shape (Sotiropoulos & Khosronejad, 2016). If the fluid flow provokes moderate shear stress on a granular bed, some grains are displaced by rolling, sliding, or by small jumps maintaining contact with the fixed part of the bed. The moving grains form then a mobile granular layer known as bed load. *Barchan* dunes are a special type of sand forms, which appear when the bed load occurs over a nonerodible surface under a flow mainly one-directional (Bagnold, 1941; Herrmann & Sauermann, 2000; Hersen, 2004). The crescentic shape of barchans is a distinctive characteristic of these dunes. The extremities of the barchan, called horns, differentiate it from other bedforms (see Figure 1.1). Devote effort to study them is highly relevant because barchan dunes are observed in a wide variety of environments, such as deserts on Earth (Bagnold, 1941), rivers, water channels (Hersen *et al.*, 2002; Franklin &

Charru, 2011), and even over the surface of other planets, like Mars and Venus (Claudin & Andreotti, 2006; Parteli & Herrmann, 2007), for example.

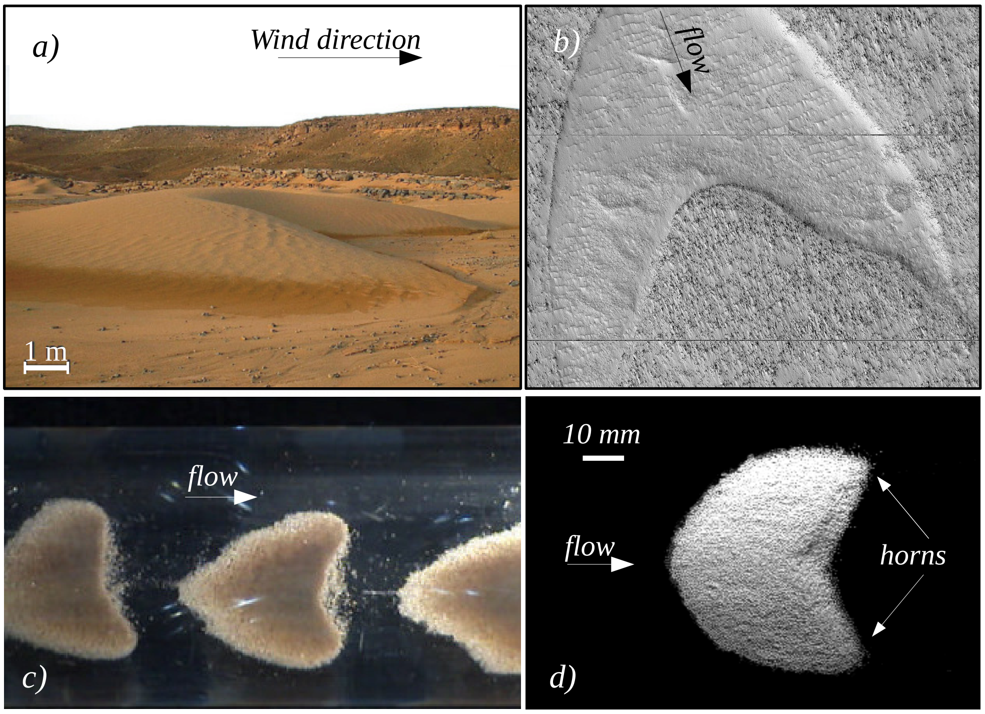

Fig. 1.1: Aeolian and aquatic barchan dunes. a) Photograph of a barchan in Erfoud, Morocco (Groh *et al.*, 2009). b) Martian dune, its size is of the order of kilometers (NASA/JPL-Caltech/University of Arizona). c) Dunes in a pipe (Al-Lababidi *et al.*, 2008). d) Barchan in a closed-conduit channel from the present experiments.

Large length and time scales are involved in the sand dunes under air flows. In Earth deserts, we find dunes of the order of 10^2 m and that took many years to develop (Bagnold, 1941). For aeolian Martian dunes, the scales reach the kilometer and millennium. In industrial pipe flows (Al-Lababidi *et al.*, 2008) and dredging systems barchans can appear, but with much shorter lengths than the aeolian case. Isolated dunes may cause an increase in pressure drop and potential damages in industrial pipe flows (Al-Lababidi *et al.*, 2012). Barchan dunes under aquatic conditions have many similitudes with those formed by air flows; consequently, it is possible to take advantage of that and study these sand patterns without the evident complications present in field measurements. Figure 1.1 shows dunes formed in aeolian and aquatic environments, namely air or water; the arrows indicate the most probable fluid direction. In Figs. 1.1(a), 1.1(c) and 1.1(d) the flow is from left to right. The crescentic shape is remarkable regardless of the environment where the dunes are present, and in all cases, the horns are formed. The interaction between the particle transport and the fluid motion, on the dynamic of the barchans, presents two interesting facts: (i) the grains are transported from upstream regions of the crest and deposited downstream because the fluid accelerates on the windward slope and decelerates on the lee side (Charru *et al.*, 2013), and (ii) the migrating velocity inversely scales to the dune height (Bagnold, 1941).

The horns pointing downstream is the main feature of a barchan. For this reason, the growing of a barchan dune can be related to the appearance and growing of its horns. Barchan dunes have been investigated by experimental, analytical, and numerical means; however, a full description is far to be reached. The general picture of barchan dune formation from the sand pile has been described with the lateral slices of the pile, of smaller height, moving faster, and this leads to the barchan shape with horns advanced downwind concerning the remaining of the dune body (Bagnold, 1941; Andreotti *et al.*, 2002a; Kroy *et al.*, 2002b). Although this description has been referred to during decades to explain dune formation in air and water, it has not been fully verified, at least experimentally. In this context, experimental studies become relevant, especially to develop accurate three-dimensional theoretical and computational models for barchan dunes. Additionally, understanding the morphology and dynamics of barchans has implications in different areas of physics and other disciplines.

1.2 Objectives

1.2.1 General objective

This work is devoted to studying the genesis and formation of subaqueous barchan dunes, from a morphological characterization to a description at the grain scale.

1.2.2 Specific objectives

- Analyze the formation of subaqueous barchan dunes from heaps initially conical undergoing turbulent water flows through an experimental approach.
- Determine the time scales for the appearance and equilibrium of dune horns, which can be associated with the birth of a barchan.

- Study the trajectories of grains going to horns for the cases of both evolving and developed dunes.

- Measure the transverse and streamwise components of the velocities of grains that form the horns of a barchan.

- Reproduce the evolution of the barchans numerically, from their initiation until they have reached a stable shape, at description levels from the bedform scale to the dynamic of the grain.

- Provide, from the subaqueous case, new insights into the physical mechanisms underlying the shape of barchan dunes, which might potentially be extrapolated to bedforms found on terrestrial deserts and other planetary environments through further investigations.

1.3 Outline of the thesis

This thesis is organized as follows: **Chapter 1** shows an overview of the barchan dunes and the objectives of this thesis. **Chapter 2** presents a literature review focused on fundamental concepts to allow understanding the aspects involved in the barchan dunes formation. Furthermore, this chapter provides fundamental concepts that are relevant to this study. **Chapter 3** presents a study on the appearance of a dune from piles initially conical and it is proposed a time scale that characterizes the birth of a subaqueous barchan. **Chapter 4** presents a description at the grain scale of the movement of grains going to the horns for both evolving and developed dunes. **Chapter 5** is devoted to the study of the evolution of subaqueous barchans employing a numerical approach. Finally, the general concluding remarks and suggestions for future works are shown in **Chapter 6**. The list of peer-review publications that this work has produced is presented as an annex. Supplementary information is provided in the appendices.

2 LITERATURE REVIEW

This chapter has the intention of presenting some fundamental concepts to allow the reader to familiarizes themselves with the background on the barchan dunes. First, a summarized description of the flow through a rectangular channel is addressed. Afterward, the parameters involved in the sediment transport are presented, namely the transport threshold, the saturated flux, and the saturation length. Finally, a brief description of the large eddy simulation is discussed.

2.1 Theoretical formulation

2.1.1 Governing equations for an incompressible flow

A flow with negligible changes in the density, as is considered in the present study, is known as an incompressible flow. Moreover, if thermal effects and substance concentrations are also considered negligible, the viscosity can be approximated by a constant. The continuity and momentum transfer equations for an incompressible flow can be expressed as

$$\frac{\partial U_j}{\partial x_j} = 0,$$
$$\rho\left(\frac{\partial U_i}{\partial t} + U_j\frac{\partial U_i}{\partial x_j}\right) = -\frac{\partial p}{\partial x_j}\delta_{ij} + \mu\frac{\partial^2 U_i}{\partial x_j \partial x_j}, \tag{2.1}$$

where U_i is the i_{th} component of the velocity vector, p is the pressure, δ_{ij} is the Kronecker delta, and ρ and μ are the density and the dynamic viscosity of the fluid, respectively. Additionally, an external force term can be considered in the momentum equation. The set of Eqs. 2.1, usually referred to as the Navier-Stokes equations, describes the behavior of the fluid flow; however, an analytic solution is not available for the general case. Thus, numerical approaches are required and the solutions are determined by discretization of the equations. In this context, numerical toolboxes such as OpenFOAM (www.openfoam.org), an open-source software, rise and are employed to simulate the behavior of fluids in several situations efficiently. OpenFOAM uses the finite volume method (FVM) for the discretization and the solution of partial differential equations. In this work, we take advantage of this software to solve the fluid flow in a rectangular channel as will be shown in **Chapter 5**.

2.1.2 Turbulence in channel flows

In this section, we present some fundamental concepts of turbulent flows in rectangular channels. Consider the flow through a rectangular channel, as sketched in Fig. 2.1, of height 2δ, length L and dimension b in the spanwise direction, where the mean velocity varies mainly in the cross-stream (y) direction, and the extension of the channel b in the spanwise direction (z) is large compared with δ. Thus, the flow is statistically independent of z. The velocities in the three coordinate directions are U, V, and W with fluctuations u, v and w. The velocity fluctuations are defined according to $u = U - \langle U \rangle$, $v = V - \langle V \rangle$, and $w = W - \langle W \rangle$, where $\langle U \rangle$, $\langle V \rangle$, $\langle W \rangle$ denote the time-averaged velocity. The mean cross-stream velocity $\langle W \rangle$ is zero.

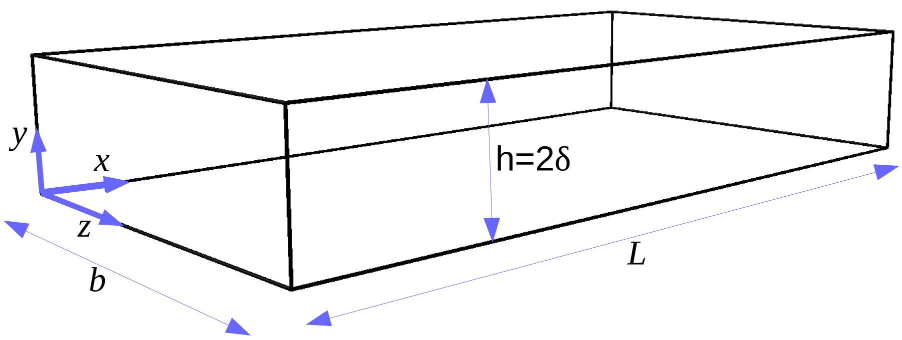

Fig. 2.1: Sketch of a rectangular channel with dimensions L in the streamwise direction, $h = 2\delta$ in the cross-stream direction, and b in the spanwise direction.

For the study of channel flows in a turbulent regime in steady conditions, it is considered that the flow is statistically stationary and statistically one-dimensional, with velocity statistics depending only on y (Pope, 2000). The Reynolds numbers employed to characterize the flow are given by Eqs 2.2 and 2.3.

$$Re \equiv \rho(2\delta)U/\mu, \tag{2.2}$$

$$Re_0 \equiv \rho U_0 \delta/\mu, \tag{2.3}$$

where U is the cross-section mean velocity, U_0 is the mean centerline velocity at $y = \delta$.

2.1.3 The balance of mean forces

Since $\langle W \rangle$ is zero and U is independent of x, the mean continuity equation reduces to

$$\frac{d\langle V \rangle}{dy} = 0, \tag{2.4}$$

integrating Eq. 2.4, with $\langle V \rangle$ = 0 on y = 0 and 2δ gives $\langle V \rangle$ = 0 for all y. Under these circumstances, the mean-flow momentum equations are:

$$0 = -\frac{\partial}{\partial y}\left(\langle p \rangle + \rho\langle v^2 \rangle\right), \tag{2.5}$$

$$0 = \nu\frac{d^2\langle U \rangle}{dy^2} - \frac{d}{dy}\langle uv \rangle - \frac{1}{\rho}\frac{\partial\langle p \rangle}{\partial x}, \tag{2.6}$$

using the boundary condition that the variance of the vertical fluctuation is zero at the wall $(y = 0)$, Eq. 2.5 integrates to

$$\langle v^2 \rangle + \langle p \rangle/\rho = p_w(x)/\rho, \tag{2.7}$$

where p and $p_w = \langle p(x{,}0{,}0) \rangle$ stand for the pressure and the mean pressure on the bottom wall, respectively, and $\nu = \mu/\rho$ is the kinematic viscosity. Equation 2.7 shows that the mean streamwise pressure gradient is uniform across the flow, i.e., it is only a function of x:

$$\frac{\partial \langle p \rangle}{\partial x} = \frac{dp_w}{dx} = f(x). \tag{2.8}$$

On the other hand, Eq. 2.6 can be expressed as

$$\frac{d\tau}{dy} = \frac{dp_w}{dx}, \tag{2.9}$$

where the total shear stress $\tau(y)$ is

$$\tau = \rho\nu \frac{d\langle U \rangle}{dy} - \rho\langle uv \rangle, \tag{2.10}$$

$\rho\nu d\langle U \rangle/dy$ is the viscous stress and $-\rho\langle uv \rangle$ corresponds to the Reynolds stress.

Thus, the only way for Eq. 2.9 to be valid is for d_τ/d_y and dp_w/dx to each be constant. Away from the wall, τ is due mostly to the Reynolds stress, close to the wall the viscous distribution dominates and at the wall the stress is entirely viscous (Kundu *et al.*, 2016).

The solutions for δ_y and dp_w/dx can be expressed in terms of the wall shear stress $\tau_w \equiv \tau(0)$, and considering that by symmetry $\tau(\delta)$ is zero, the solution to Eq. 2.9 is

$$\frac{\tau_w}{\delta} = -\frac{dp_w}{dx}, \tag{2.11}$$

and τ along y is expressed as

$$\tau(y) = \tau_w \left(1 - \frac{y}{\delta}\right), \tag{2.12}$$

normalizing τ_w by a reference velocity, we obtain the friction coefficient $C_f \equiv \tau_w/0.5\rho U^2$.

2.1.4 Scales in the near-wall region

As stated above, at the wall, the Reynolds stresses are zero, so the wall shear stress is due entirely to the viscous contribution. Close to the wall τ_w, ρ, and ν are the appropriate parameters to define viscous scales for the velocity and the length. One of these is the friction velocity

$$u_* \equiv \sqrt{\frac{\tau_w}{\rho}}, \tag{2.13}$$

another one is the viscous length scale

$$\delta_\nu = \nu/u_*. \tag{2.14}$$

Additionally, the friction Reynolds number can be defined as

$$Re_* \equiv \frac{u_*\delta}{\nu}, \tag{2.15}$$

and the distance in wall units is given by

$$y^+ \equiv y/\nu = \frac{u_* y}{\nu}. \tag{2.16}$$

The turbulent flow in a rectangular channel can be analyzed in different regions defined along the y direction on the basis of y^+. So we have the viscous wall region for y^+ < 50, in this region the molecular viscosity domains. Conversely, in the outer layer y^+ > 50 the effect of the viscosity is negligible. There is a viscous sublayer for y^+ < 5, where the Reynolds shear stress is negligible compared with the viscous stress. For y^+ > 30 is defined a region governed by a logarithmic law, which is simply known as *log-law* region. Between the viscous sublayer (y^+ < 5) and the *log-law* region (y^+ > 30) it is defined the buffer layer. It is a transition region between the viscosity-dominated and the turbulence-dominated parts of the flow (Pope, 2000).

For the viscous sublayer it is kept the linear relation $u^+ = y^+$, and the *log-law* is given by $u^+ = \kappa^{-1} \ln y^+ + B$, where κ is the von Kármán constant and B is a constant. Generally, the values assigned for the *log-law* constants are $\kappa = 0.41$ and $B = 5.2$.

2.1.5 Mixing length theory

In the context of turbulent shear flow past a wall, the fluid can sustain more shear stress due to the turbulence fluctuations and eddies compared to the laminar case. This effect can be modeled introducing a turbulent viscosity μ_T or a turbulence shear stress τ_T (the latter corresponds to the Reynolds shear stress $-\rho\langle uv\rangle$), so τ_T can be expressed as (Hinrichsen & Wolf, 2006; White, 2006)

$$\tau_T = -\rho\langle uv\rangle = \mu_T \left(\frac{dU}{dy}\right). \tag{2.17}$$

Prandtl (1935) proposed an expression for the turbulent viscosity μ_T, it was defined as

$$\mu_T = \rho l^2 \left(\frac{dU}{dy}\right), \tag{2.18}$$

μ_T has the same dimensions as μ, but it is not a fluid property, varying instead with flow conditions and geometry. In Eq. 2.18 the mixing length l is some function of the flow and/or position. This length can be interpreted as being a length in a direction transverse to the flow that an eddy must displace for its velocity to reach that of the mean flow (Schlichting, 2000). Prandtl (1935) assumed that the mixing length varies linearly with the distance from the wall, $l = \kappa y$. Under this consideration, the turbulence shear stress can be expressed by

$$\tau_T = \rho\kappa^2 y^2 \left(\frac{dU}{dy}\right)^2. \tag{2.19}$$

By integrating Eq. 2.19 from y_0 to y and assuming that the turbulent shear stress is the overall shear stress τ (because the flow is considered fully turbulent), one can solve Eq. 2.19 for U to obtain

$$U = \frac{1}{\kappa}\sqrt{\frac{\tau_w}{\rho}}\, ln\left(\frac{y}{y_0}\right), \tag{2.20}$$

where it was made the further assumption that τ is constant and equal to the wall stress τ_w. It was also defined y_0 as a roughness length above the wall at which the velocity is zero. Equation 2.20 shows that the mean velocity profile is logarithmic with distance from the wall. The roughness length is either defined by the thickness of the viscous sublayer or by the size of the surface perturbations.

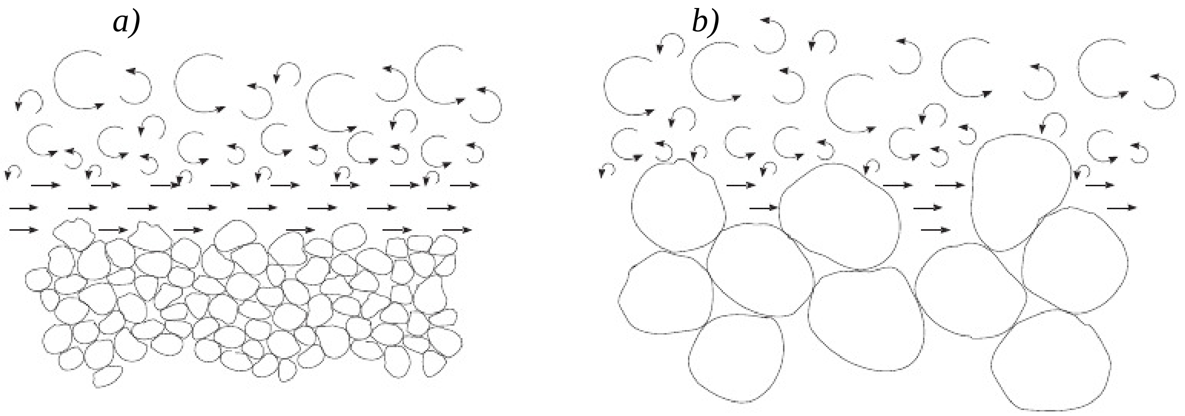

Fig. 2.2: Hydraulically smooth and rough surfaces depending on the grain sizes. Figure retrieves from Sauermann (2001).

In Fig. 2.2 the perturbations are caused by particles interacting with the fluid flow. Figure 2.2(a) shows grains immersed in the viscous sublayer, which creates a hydraulically smooth surface. On the other hand, in Fig. 2.2(b) the grains are larger than the viscous sublayer and create a hydraulically rough surface. The turbulent viscosity can be obtained from an algebraic relation, such as the mixing length model, or it can be obtained from modeling and/or turbulence simulation. In section 2.2, the main aspects involved in large eddy simulation are presented.

2.1.6 Sediment transport

The transport of granular matter can be addressed at two levels: (i) focusing on the dynamics at the grain scale, and (ii) averaging the fluxes of mass. Depending on the mode of transport and on the flow regime, the link between these two levels exists or is still incomplete (Andreotti *et al.*, 2013). Gravity, hydrodynamic forces, and contact forces are exerted on the particles, and depending on them different modes of sediment transport are produced. Suspension is a mode depending, mainly, on hydrodynamic forces, independently of the hydrodynamic regime, namely viscous, laminar o turbulent, this mode is associated with the transport of fine particles.

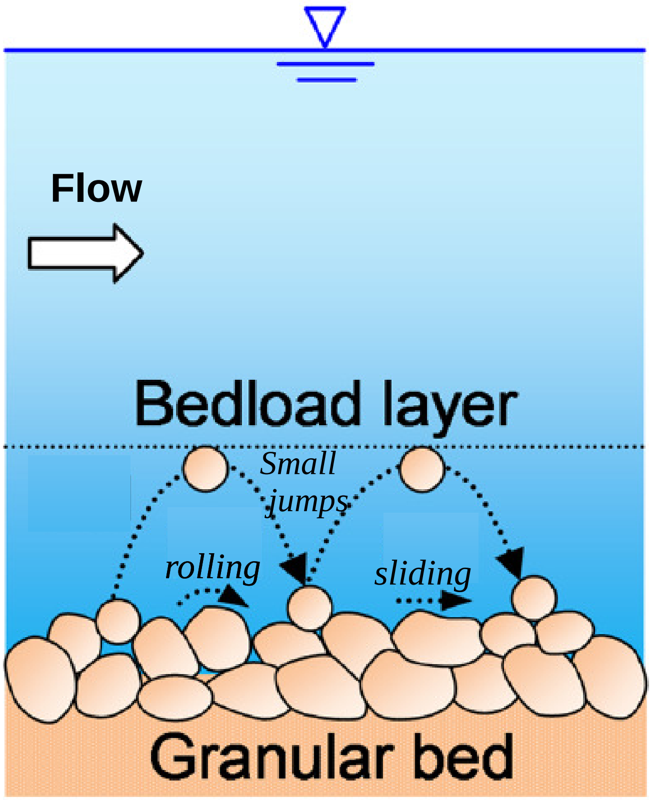

Fig. 2.3: Schematic diagram illustrating the mode of transport called bed load (adapted from Ali & Dey (2018)).

When the effect of gravity is large enough to confine transport to a thin layer at the surface of the sand bed, the transport mode is called bed load (Fig. 2.3). In this case, the grains, entrained by the fluid, move by rolling, sliding, or by small jumps, in this mode, the three forces act simultaneously.

The mode of transport when the particles make successions of jumps is called saltation. In air, they rise several hundred or thousand-grain diameters and moving downstream even longer distances, in water the height of rising is a few grain diameters, but the motion appears to be essentially the same, the saltation term, however, is used for the motion of sand in air. The grains transported in saltation and colliding with the fixed bed with enough energy cause the transport known as reptation (Bagnold, 1941; Andreotti *et al.*, 2013). Contact forces and gravity dominate the reptation mode. Different bedforms such as dunes and ripples depend on how the sediment flux and the fluid flow are interacting for these modes of transport.

2.1.7 The Shields number

Considering that a grain start to move when a driving force F_{drag} is equal to its apparent weight, one can quantitatively define a criterion for the entrainment from the ratio $F_{drag}/([\rho_s - \rho]gd^3)$, where ρ_s is the density of grains, ρ is the fluid density, d is the grain diameter, and g is the acceleration of gravity. The driving force is the hydrodynamic force exerted by the fluid on a flat surface and it is dimensionally proportional to τd^2, τ being the shear stress at the interface between the grains and fluid. Therefore, the onset of particle motion and transport are controlled by the dimensionless number, denominated Shields number (Shields, 1936), and defined by

$$\theta = \frac{\tau}{(\rho_s - \rho)gd} = \theta(Re_*). \tag{2.21}$$

The entrainment of grains as bed load takes place in the range $0.01 \leq \theta \leq 1$; below there is no transport and above there is transport by suspension (see Fig. 2.4). A schematic illustration of the origin of the sediment-transport threshold at the grain scale is presented in Fig. 2.5, where d is the grain diameter subject to the driving force F_{drag}, and P is the submerged weight of the grain.

As we have seen, the entrainment threshold is controlled by the threshold Shields number θ_{th}, which depends on the shear stress τ. The later is related to the fluid velocity at grain scale u_* by $\tau = \rho\, u_*^2$. This parameter characterizes the flow and is known as the friction velocity or shear velocity.

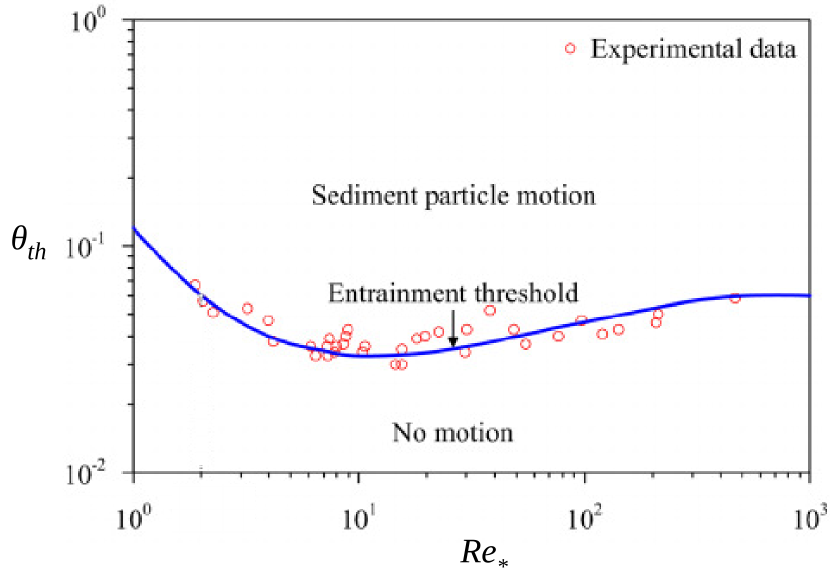

Fig. 2.4: The Shields number θ_{th} above which a flow can entrain grains of size d (adapted from Dey & Ali (2018)).

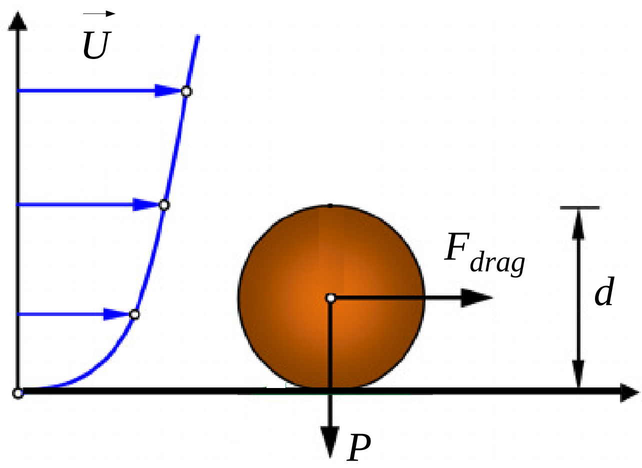

Fig. 2.5: Sketch of the origin of the sediment-transport threshold at the scale of the grain (adapted from Dey & Ali (2018)).

2.1.8 The saturated flux and saturation length

After a certain time, a steady flow acting on a sediment bed reaches the equilibrium between the particle transport and the flow; it is characterized by a flux $q = q_{sat}$ denominated saturated flux. In this state, there exists a balance between the particles deposited and particles eroded from the bed (Andreotti *et al.*, 2013). The process of saturation of the transport does not occur instantly, but it requires a delay in time and space (Bagnold, 1941; Sauermann *et al.*, 2001; Andreotti *et al.*, 2002a; Charru, 2006; Andreotti *et al.*, 2013). Moreover, q_{sat} is controlled by the local value of the shear stress τ. The delay scales of the flux correspond to the saturation time and saturation length L_{sat}, the first one is short compared with the time for bedform growth time, and it is generally neglected. In one dimension and along the direction x, the differential equation that links L_{sat} to q_{sat} is:

$$L_{sat}\frac{\partial q}{\partial x} = q_{sat} - q. \tag{2.22}$$

Figure 2.6 presents schematically the behavior of the particle flux q as a function of horizontal distance x.

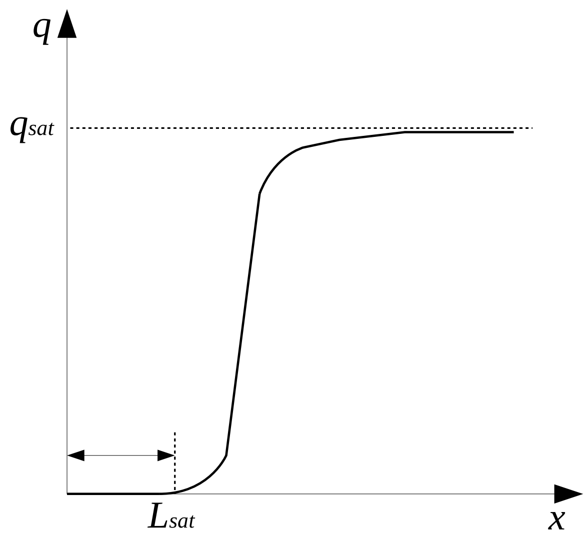

Fig. 2.6: Particle flux as a function of space. The characteristic distance to reach the saturated flux q_{sat} is called saturation length L_{sat}.

The empirical formula proposed by Meyer-Peter & Müller (1948) can be used to determine the saturation flux in the case of bed-load transport:

$$q_{sat} \sim 8\sqrt{\frac{\rho_s - \rho}{\rho_s} g d^3}(\theta - \theta_{th})^{3/2}, \tag{2.23}$$

where θ_{th} is the threshold Shields number for setting the grains in motion. Charru & Hinch (2006) proposed that the saturation transient is limited by the erosion and deposition mechanisms, and for the bed-load case, they found that saturation length can be calculated as

$$L_{sat} \propto \frac{u_*}{u_{fall}} d, \tag{2.24}$$

where u_* is the fluid velocity at the grain scale and u_{fall} is settling velocity of a grain, however, at least for the bed-load case L_{sat} has not been measured directly (Charru *et al.*, 2013).

For saltation in air, the saturation transient is limited by grain inertia, thus L_{sat} scales with the length needed for a grain accelerate and reach the wind velocity (Hersen, 2004; Claudin & Andreotti, 2006; Andreotti *et al.*, 2010; Charru *et al.*, 2013). L_{sat} can be expressed as:

$$L_{sat} \propto \frac{\rho_s}{\rho} d, \tag{2.25}$$

the saturation length, therefore, is proportional to an inertial length L_{drag} and independent of u_*. The sand flux gets saturated after a distance scaling with L_{drag}, and only depends on the grain inertia in the surrounding fluid.

2.1.9 Threshold velocity to move grains on the bed

A grain will set in motion only if the $F_{drag} = \tau d^2$ is larger than its weight; then, there exists a threshold velocity u_{th} below which a bed of grains cannot be eroded by the fluid:

$$u_{th} = A\sqrt{\frac{\rho_s - \rho}{\rho} gd}. \tag{2.26}$$

For air, the coefficient A, experimentally determined, is equal to 0.1 and for water is found to be around 0.2 (Bagnold, 1941; Andreotti *et al.*, 2002a). Fluid velocity values higher than u_{th} cause that the grains start rolling at the surface, and some of them can take off the bed.

2.2 Large eddy simulation

In large eddy simulation (LES), the larger scales, which can be three dimensional and unsteady, are directly computed, whereas the small subgrid scales are modeled. LES is based on the assumption that the small scales tend to be more isotropic than the large ones. Thus, it is thought that it should be possible to parametrize them using simpler and more universal models than standard Reynolds stress models.

LES is based on the methodology of applying a filtering procedure to the Navier-Stokes equations; thus, the time and space dependence of the fluid motions are resolved down to some defined length scale. The filtering process eliminates scales smaller than the prescribed length-scale. The eliminated scales are called subgrid-scale (SGS) (see Pope (2000) for precise definitions). Applying a filtering process into Eqs. 2.1, one obtains the LES equations for incompressible flows

$$\frac{\partial \overline{U}_j}{\partial x_j} = 0,$$
$$\rho \left(\frac{\partial \overline{U}_i}{\partial t} + \bar{U}_j \frac{\partial \overline{U}_i}{\partial x_j} \right) = -\frac{\partial \overline{p}}{\partial x_j}\delta_{ij} + \mu \frac{\partial^2 \overline{U}_i}{\partial x_j \partial x_j} - \frac{\partial \tau_{ij}^{sgs}}{\partial x_j}, \tag{2.27}$$

the SGS stress tensor τ_{ij}^{sgs} is defined according to

$$\tau_{ij}^{sgs} = \overline{U_i U_j} - \overline{U_i}\,\overline{U_j}, \tag{2.28}$$

τ_{ij}^{sgs} is originated from the filtering process of the nonlinear terms $\overline{U_i U_j}$. However, Eq. 2.28 is unclosed since τ_{ij}^{sgs} must be expressed in terms of features of the filtered (resolved) velocity field $\overline{U}_i$.

For the incompressible flows, eddy viscosity models based on the Boussinesq hypothesis are employed. In such models, only the deviatoric part of the stress tensor is relevant since the gradient of its trace may be absorbed into an effective pressure field. The subgrid-scale stress tensor is given as follows:

$$\tau_{ij}^{sgs} - \frac{1}{3}\tau_{kk}^{sgs}\delta_{ij} = -2\mu_T\overline{S_{ij}}. \tag{2.29}$$

Smagorinsky (1963) developed a subgrid-scale (SGS) stress model based on the assumption of an eddy (turbulent) viscosity μ_T. In his model, it is assumed that the small scales are in equilibrium, i.e., the dissipation and the energy production are in balance. Equation 2.30 shows the expression proposed by Smagorinsky (1963) for the eddy viscosity

$$\mu_T = (C_s\Delta)^2|\overline{S}|, \tag{2.30}$$

where the overbar denotes the grid filtering operation, C_s is the Smagorinsky constant, Δ is the filter size, and $|\overline{S}| = \sqrt{2\overline{S_{ij}}\ \overline{S_{ij}}}$ is the magnitude of the large-scale strain-rate tensor (Germano *et al.*, 1991), where $\overline{S_{ij}}$ is defined as

$$\overline{S_{ij}} = \frac{1}{2}\left(\frac{\partial\overline{U_i}}{\partial x_j} + \frac{\partial\overline{U_j}}{\partial x_i}\right), \tag{2.31}$$

with $\overline{U_i}$ being the large-scale velocity. Δ is proportional to the grid size, in this thesis the box filter is employed, which is given by $\Delta = (V_{cell})^{1/3}$, V_{cell} representing the cell volume and the filter size being taken as its cubic root. In some works, after Smagorinsky (1963), the coefficient C_s has been assumed as a constant value ranging between 0.1 and 0.3, or as a dynamical value depending on the local flow conditions (Germano *et al.*, 1991).

In wall-bounded flows, the classical Smagorinsky model has been found to not represent the eddy viscosity μ_T profile correctly. To recover the correct behavior of μ_T near the wall, there have been proposed some SGS models, from simple explicit damping to more elaborate models. The Wall-Adapting Local Eddy-Viscosity, WALE, model (Nicoud & Ducros, 1999) has been found to produce the correct profile of the eddy viscosity in the proximity of the wall at a low computational cost. WALE is one of the SGS models available in OpenFOAM; for its excellent results for channel flows, it has been chosen to be used in this work. There is a vast literature on the modeling of dune formation. An extensive literature review of the state-of-the-art of the aspects involved in the morphology and dynamics of the barchans is undertaken in the introduction sections of the next chapters.

3 BIRTH OF A SUBAQUEOUS BARCHAN DUNE†

*The present chapter reports the formation of subaqueous barchan dunes from initially conical heaps in a rectangular channel. Because the most unique feature of a barchan dune is its horns, we associate the time scale for the appearance of horns to the formation of a barchan dune. A granular heap initially conical was placed on the bottom wall of a closed conduit and it was entrained by a water flow in turbulent regime. Here, we demonstrate that, after a certain time, horns appear and grow, until an equilibrium length is reached. Our results show the existence of the time scales 0.5*t_c *and 2.5*t_c *for the appearance and equilibrium of horns, respectively, where* t_c *is a characteristic time that scales with the grains diameter, gravity acceleration, densities of the fluid and grains, and shear and threshold velocities.*

3.1 Introduction

Sand dunes are frequently found in both nature and industry, being present in deserts, rivers (Bagnold, 1941), and petroleum pipelines (Schaflinger *et al.*, 1995; Stevenson *et al.*, 2001; Al-Lababidi *et al.*, 2012), for example. Those forms result from the transport of sand entrained by a fluid flow and, depending on many factors, such as the flow direction, the strength of the flow, the amount of available sand, and the sand cover, different kinds of dunes are observed. When the fluid flow causes moderate shear stress on a granular bed, some grains are displaced by rolling, sliding, or by small jumps maintaining contact with the fixed part of the bed. The moving grains form then a mobile granular layer known as bed load. If it takes place over a nonerodible ground or with limited sediment supply under a one-directional flow, they form dunes of crescentic shape, known as barchan dunes (Bagnold, 1941; Herrmann & Sauermann, 2000; Hersen, 2004). Under those conditions, barchan dunes are strong attractors that can appear in water and oil pipelines, on the bed of rivers and deserts, and on the surface of other planets (Claudin & Andreotti, 2006; Parteli & Herrmann, 2007), for example. The main feature of a barchan dune that differentiates it from other bedforms is its horns pointing downstream. For this reason, the growing of a barchan dune from a granular heap can be related to the appearance

† This chapter is based on C. A. Alvarez and E. M. Franklin, Phys. Rev. E. 96, 062906 (2017). (Alvarez & Franklin, 2017a)

and growing of horns.

Over the past few decades, many works were devoted to the equilibrium and minimum size of barchan dunes (Sauermann *et al.*, 2000; Hersen *et al.*, 2002; Andreotti *et al.*, 2002a; Hersen *et al.*, 2004; Hersen, 2004; Kroy *et al.*, 2005; Parteli *et al.*, 2007; Franklin & Charru, 2011; Kidanemariam & Uhlmann, 2017) and to instabilities giving rise to barchans (Kroy *et al.*, 2002b; Guignier *et al.*, 2013; Parteli *et al.*, 2011; Khosronejad & Sotiropoulos, 2017). These works investigated the length, width, height, and horn scales, the ratios among them, their relation with the saturation length, and the celerity of barchans for both stable and evolving dunes. The saturation length L_{sat} is the length for the stabilization of sand flux, i.e., it is the length necessary for the sand flux to reach equilibrium conditions with a varying fluid flow (Andreotti *et al.*, 2002a; Charru *et al.*, 2013). It has been argued that L_{sat} is proportional to an inertial length in the aeolian case (Hersen *et al.*, 2002; Sauermann *et al.*, 2001), $L_{drag} = (\rho_s/\rho)d$, and to a relaxation length in the aquatic case (Franklin & Charru, 2011; Charru *et al.*, 2013; Charru, 2006), $l_d = (u_*/U)d$ or $l_{fall} = (u_*/u_{fall})d$, where ρ is the fluid density, ρ_s is the density of grains, d is the grain diameter, u_* is the shear velocity, u_{fall} is the settling velocity of one grain, and U is the cross-section mean velocity of the fluid. Pähtz *et al.* (2013) derived a theoretical expression for the saturation length that combines (ρ_s/ρ), d and the fluid velocity. Their expression, which is valid for both aeolian and subaqueous bed load, is in agreement with experimental measurements varying (ρ_s/ρ) over five orders of magnitude. On the other hand, Claudin & Andreotti (2006) showed that the wavelength of dunes scales with L_{drag} over five decades. Therefore, although the fluid flow conditions affect L_{sat}, we consider in this study that L_{sat} is proportional to L_{drag}.

Among the studies devoted to the formation of a barchan dune from an initial heap or flat bed, few investigated the behavior of the horns. One of them is Khosronejad & Sotiropoulos (2017), which numerically investigated transverse waves propagating over the horns of already-existing barchan dunes and giving rise to new barchans, and showed that the amplitude and wavelength of transverse waves and generated barchans are related. However, none of them investigated the time evolution of growing horns from an initially conical heap. The evolution of the horns for a single barchan dune from an initial conical pile can shed some light on the time scales for the growth of individual barchans and then characterize the instant corresponding to the appearance of a barchan dune. This question, which has yet to be fully understood, is important to improve our knowledge on the formation of barchans under more complex scenarios, such as sand bars, large sand fields, sand fields over complex topographies, etc.

3.2 Experimental setup and methods

The present experimental results on the formation of subaqueous barchan dunes from conical heaps show the existence of characteristic times for the growth and equilibrium of horns. The term equilibrium refers to the crescentic shape of barchan dunes, with horns pointing downstream, which are characteristic of barchan dunes.

3.2.1 Experimental setup

The experimental device consisted of a water reservoir, two centrifugal pumps, a flow straightener, a 5-m-long closed-conduit channel, a settling tank, and a return line. The flow straightener was a divergent-convergent nozzle filled with d = 3 mm glass spheres, the function of which was to homogenize the flow profile at the channel inlet. The channel had a rectangular cross section (width = 160 mm and height 2δ = 50 mm) and was made of transparent material. The channel test section was 1 m long and started 40 hydraulic diameters (3 m) downstream of the channel inlet; therefore, the turbulent flow was completely developed in the test section. Figure 3.1 shows the layout of the experimental device. The grains were placed in the test section, which was previously filled with water, and they settled forming a conical heap on the channel bottom wall. Next, a water flow was imposed in the channel, and the heap deformed into a barchan dune. With this procedure, each experiment concerns one single isolated dune. The evolution of the dune was recorded with a charged coupled device (CCD) camera placed above the channel and mounted on a traveling system. Figure 3.2 presents one example of top view image, where the characteristic lengths of a barchan dune, namely its length L, width W, and horn length L_h, are shown. Because usually barchan dunes are slightly asymmetric, we consider L_h as the average of both horns. The fluid flow was measured with an electromagnetic flow meter and a two-dimensional particle image velocimetry (2D-PIV) device.

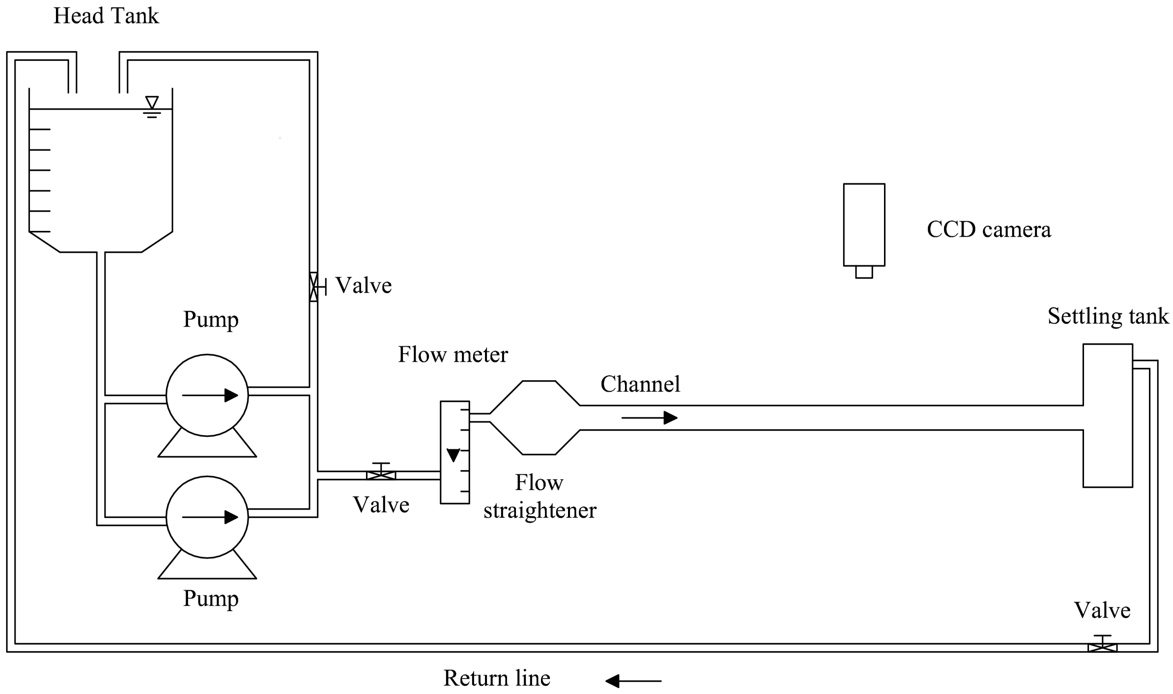

Fig. 3.1: Layout of the experimental device.

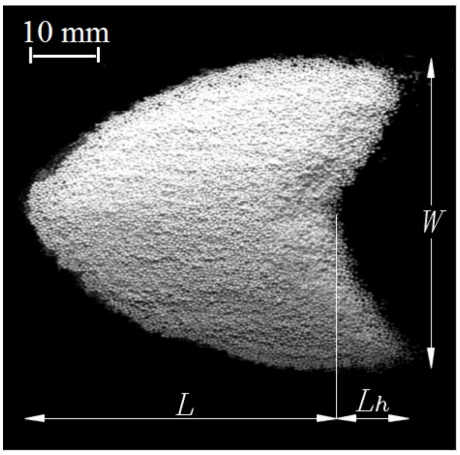

Fig. 3.2: Top view of a barchan dune and its characteristic lengths: length L, width W, and horn length L_h.

In the tests, the cross-section mean velocities U were 0.234, 0.294, and 0.333 m/s, corresponding to Reynolds numbers based on the channel height $Re = \rho U 2\delta/\mu$ of 1.16 $\times 10^4$, 1.47 $\times 10^4$, and 1.67 $\times 10^4$, respectively, where μ is the dynamic viscosity of the fluid. The employed fluid was tap water at temperatures within 24 and 26 ^{o}C, and the employed grains were round glass beads (ρ_s = 2500 kg/m^3 and bulk density of 1500 kg/m^3) with 0.25 mm $\leq d \leq$ 0.50 mm and 0.40 mm $\leq d \leq$ 0.60 mm, angular glass beads with 0.21 mm $\leq d \leq$ 0.30 mm, and round zirconium beads (ρ_s = 4100 kg/m^3 and bulk density of 2400 kg/m^3) with 0.40 mm

Table 3.1: Different tested conditions: ρ_s/ρ, state of the grains surface, d, Re, Re_*, θ, and the total mass of each heap.

Condition ...	ρ_s/ρ ...	Surface ...	d (mm)	Re ...	Re_* ...	θ ...	mass (g)
a	2.5	round	0.25 – 0.50	1.16×10^4	5	0.04	10.5
b	2.5	round	0.25 – 0.50	1.47×10^4	7	0.06	10.5
c	2.5	round	0.25 – 0.50	1.67×10^4	7	0.07	10.5
d	2.5	round	0.40 – 0.60	1.16×10^4	7	0.03	10.5
e	2.5	round	0.40 – 0.60	1.47×10^4	9	0.04	10.5
f	2.5	round	0.40 – 0.60	1.67×10^4	10	0.05	10.5
g	2.5	angular	0.21 – 0.30	1.16×10^4	2	0.09	10.5
h	2.5	angular	0.21 – 0.30	1.47×10^4	3	0.13	10.5
i	2.5	angular	0.21 – 0.30	1.67×10^4	3	0.16	10.5
j	4.1	round	0.40 – 0.60	1.47×10^4	9	0.02	10.5
k	4.1	round	0.40 – 0.60	1.67×10^4	10	0.03	10.5
l	4.1	round	0.40 – 0.60	1.47×10^4	9	0.02	16.5
m	4.1	round	0.40 – 0.60	1.67×10^4	10	0.03	16.5

$\leq d \leq$ 0.60 mm (see Appendix A for the images of the scanning electron microscopy of the used beads). The shear velocities on the channel walls were computed from the velocity profiles acquired by the PIV device and were found to follow the Blasius correlation (Schlichting, 2000). They correspond to 0.0143, 0.0177, and 0.0195 m/s for the two flow rates employed. The initial heaps were formed with 10.5 g of glass beads, and with 16.5 g and 10.5 g of zirconium beads, corresponding to initial volumes of 7.0, 6.9, and 4.4 cm^3, respectively. Table 3.1 presents the parameters of different flow and grains used in the experiments. For each of the conditions listed, between two and four test runs were performed and are shown next. In this table, two additional parameters are presented, the particle Reynolds number, $Re_* = \rho u_* d/\mu$, and the Shields number, $\theta = (\rho u_*^2)/[(\rho_s - \rho)gd]$, where g is the acceleration of gravity. The particle Reynolds number is the Reynolds number at the grain scale, and the Shields number is the ratio between the entraining force, which is given by the drag caused by the fluid on each grain, and the resisting force, given by the weight of each grain.

3.3 Results and discussion

3.3.1 Width and length measurements

With the conical heap in the channel, the water flow was imposed at a constant rate. Before being displaced over a measurable distance, the pile was deformed and adopted a crescentic shape as shown in Fig. 3.3. In all cases, a slip face was formed. Although far from the threshold for incipient motion of grains ($\theta \geq$ 0.03), barchan dunes have robust ratios among their length L, width W, and height h both for the aeolian and subaqueous cases (Hersen *et al.*, 2002), we found that the ratio W/L may diverge close to incipient bed load conditions (0.02 $\leq \theta \leq$ 0.03). From Figs. 3.3(b) and 3.3(c), we note the differences in the W/L ratios during the development of barchan dunes under different flow conditions. The larger values of W/L close to threshold conditions persist when barchans have reached equilibrium. As shown in Fig. 3.4, which presents the time evolution of W/L, the dunes consisting of 0.40 mm $\leq\ d\ \leq$ 0.60 mm zirconium beads under Re = 1.47 $\times 10^4$ (cases j and l of Table 3.1) have W/L values around twice the values presented by dunes farther from the threshold. The cases listed in the key are presented in Table 3.1 (see Appendix A for W/L versus time of all the test runs). In Fig. 3.4, the time was normalized by a characteristic time t_c computed as the length of the bedform divided by its celerity C, the latter obtained from the flux rate of grains, q, divided by L_{sat} Claudin & Andreotti (2006). Because we are interested in subaqueous barchans, we considered q given by the Meyer-Peter & Müller (1948) equation, and $L_{sat} \propto L_{drag}$. In this manner, t_c is a characteristic time for the displacement of barchans, computed by Eq. 3.1,

$$t_c = \frac{L_{eq}}{C} = \frac{L_{eq}\left(\rho_s/\rho\right)\left(\rho_s/\rho - 1\right)gd}{\left(u_*^2 - u_{th}^2\right)^{3/2}}, \tag{3.1}$$

where u_{th} is the fluid threshold velocity for incipient motion of grains, L_{eq} is the barchan length at equilibrium, and g is the acceleration of gravity. The threshold velocity was computed in accordance to Andreotti *et al.* (2002a). In this way, the commonly reported value $W/L \approx 1$ (Hersen *et al.*, 2002; Franklin & Charru, 2011) is not a good indication of the formation and equilibrium of a barchan dune close to threshold conditions [see Fig. 3.3(c)]. As noted by Kroy

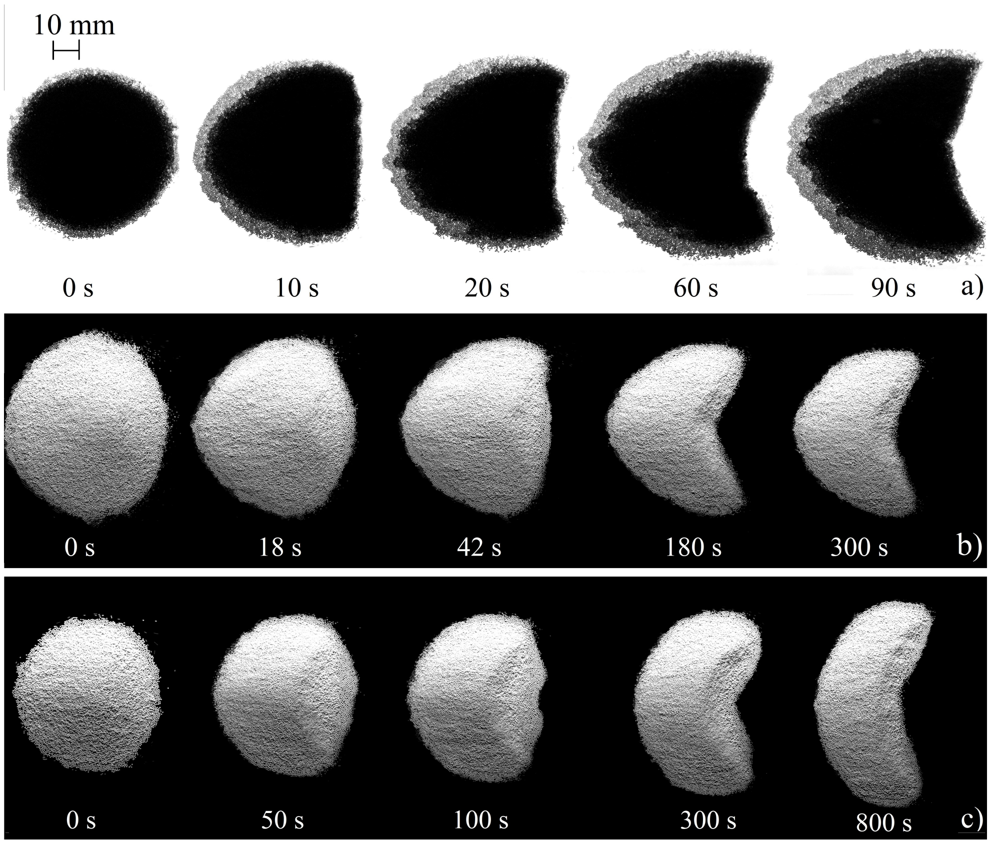

Fig. 3.3: Top views of initially conical heaps deformed by the water flow at different times; the water flow is from left to right. (a) Re = 1.47 $\times 10^4$, ρ_s = 2500 kg/m^3, and 0.40 mm $\leq d \leq$ 0.60 mm. (b) Re = 1.67 $\times 10^4$, ρ_s = 4100 kg/m^3, and 0.40 mm $\leq d \leq$ 0.60 mm. (c) Re = 1.47 $\times 10^4$, ρ_s = 4100 kg/m^3, and 0.40 mm $\leq d \leq$ 0.60 mm.

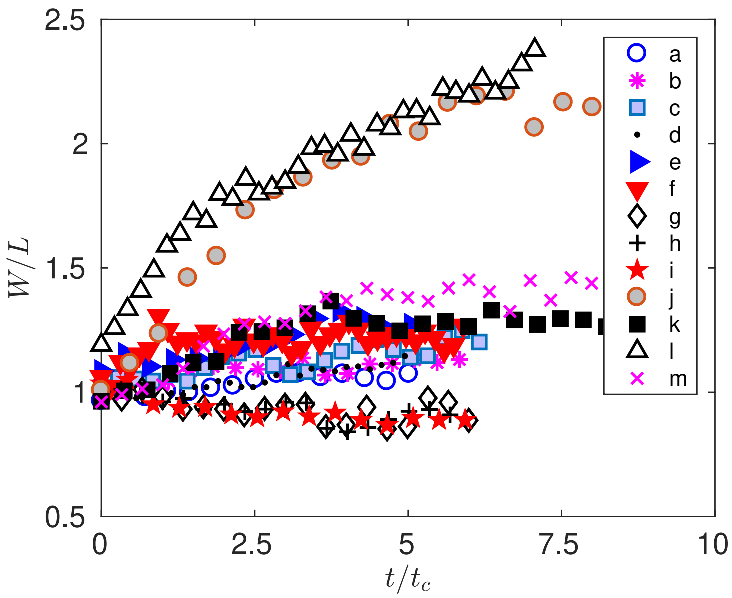

Fig. 3.4: W/L versus t/t_c for different flow conditions and solid particles. The cases listed in the key are presented in Table 3.1. This figure shows every n measurements for each experimental condition, where $5 \leq n \leq 15$.

& Guo (2004), there is evidence that the scale invariance of barchan dunes is broken in the longitudinal direction and, in order to test similarity and scaling laws, the longitudinal scales shall be addressed.

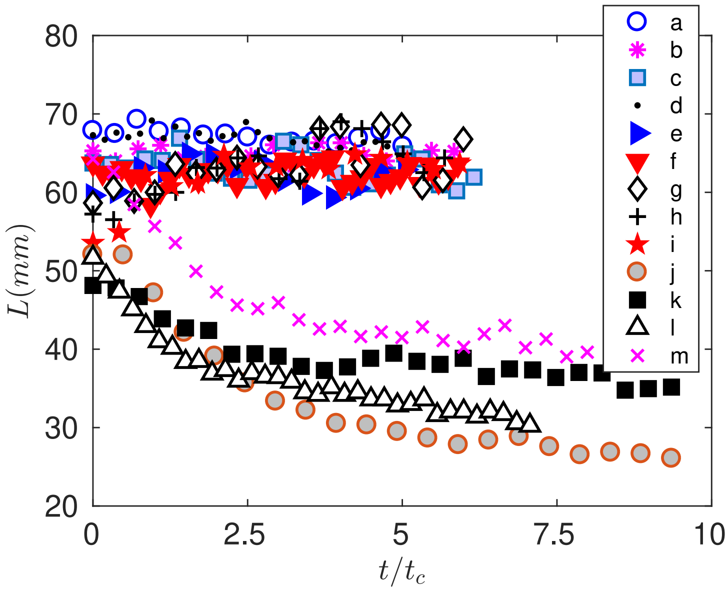

(a)

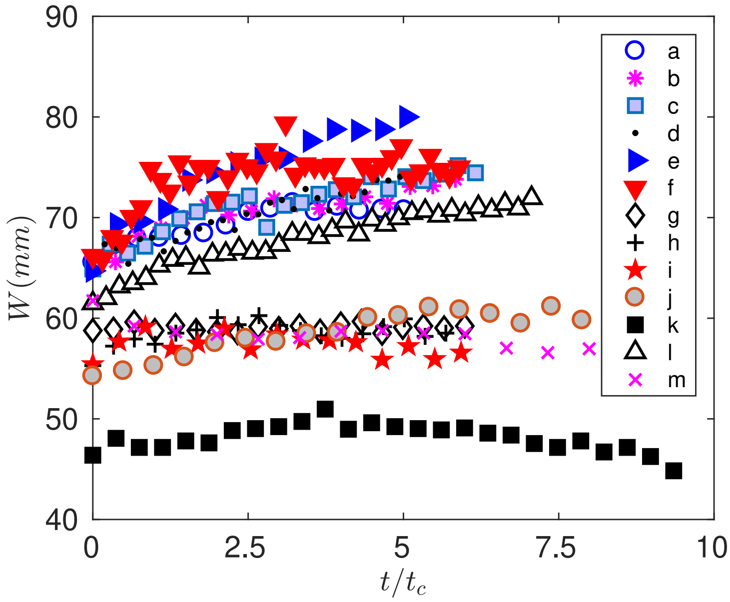

(b)

Fig. 3.5: (a) L versus t/t_c and (b) W versus t/t_c for different flow conditions and solid particles. The cases listed in the key are presented in Table 3.1. This figure shows every n measurements for each experimental condition, where $5 \leq n \leq 15$.

Figures 3.5(a) and 3.5(b) present the time evolutions of the length and width of dunes, L and W versus t/t_c, respectively, for different flow conditions and solid particles. The cases listed in the key are presented in Table 3.1 (see Appendix A for L and W versus time of all the test runs). From Fig. 3.5(a), we observe different behaviors from the initial piles, with the heaps consisting of heavier zirconium beads decreasing over time while those of glass beads remain constant or increase slightly. The time scales to attain the crescentic shape are very different, being around $2.5t_c$ for the glass beads and $6.0t_c$ for the zirconium beads. In the case of W, Fig. 3.5(b) shows that for the different grains and flow conditions the behavior is distinct and a specific timescale cannot be determined. Although close to threshold W/L diverges and equilibrium times based on L and W are very different, in all cases the conical pile evolves to a crescentic shape with the growing of horns. Therefore, we investigate the time evolution of horns in order to determine when a barchan dune appears and when it reaches equilibrium. In the next section, we address the study of the horns.

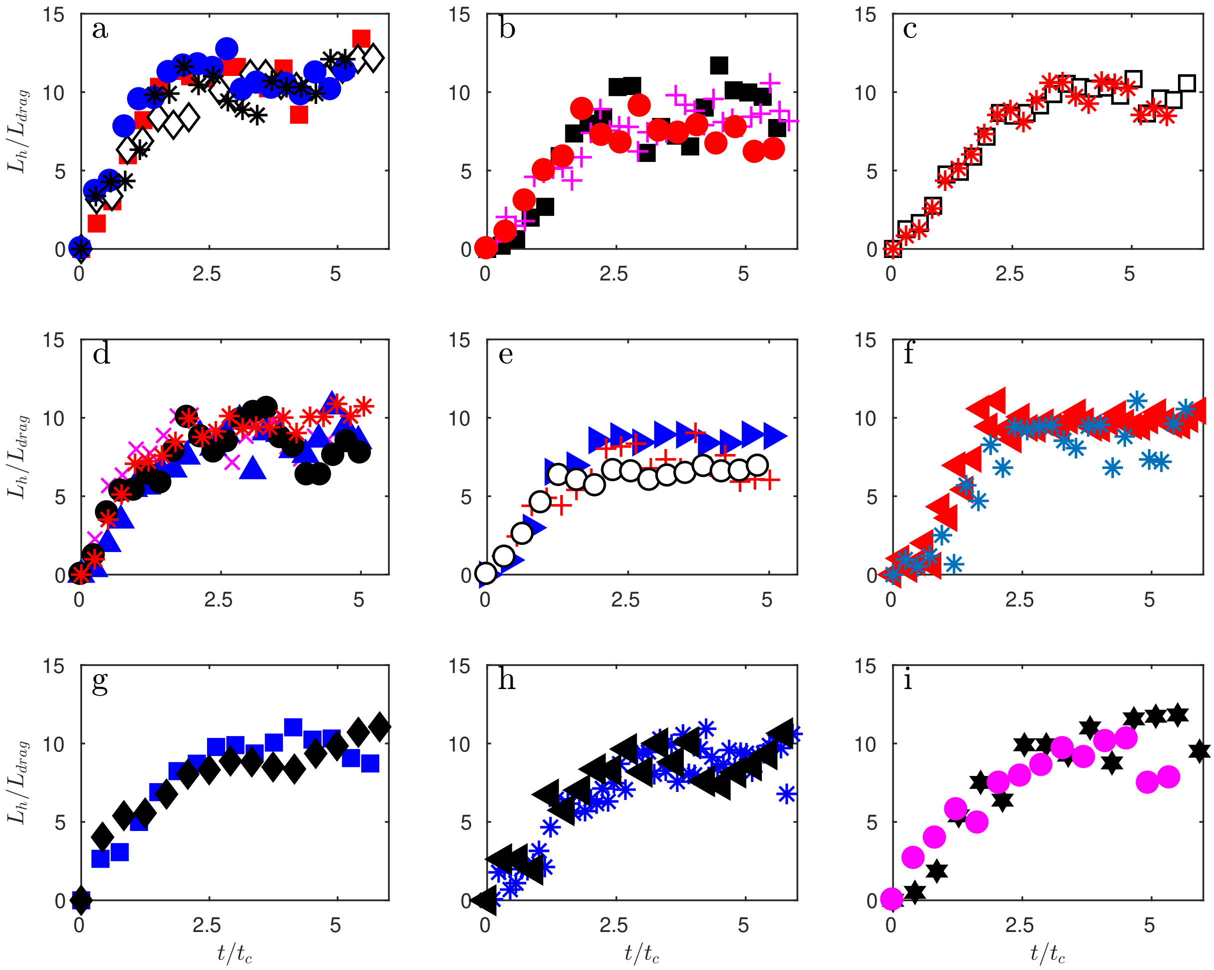

Fig. 3.6: L_h/L_{drag} versus t/t_c for glass beads under different flow conditions over the entire duration of test runs. This figure shows every n measurements for each experimental condition, where $5 \leq n \leq 15$. The cases (a) to (i) are summarized in Table 3.1, and each different symbol in each graphic corresponds to a different test run.

3.3.2 Horn length measurements

Figures 3.6 to 3.9 present the time evolution of horns for different flow conditions and solid particles. The cases (a) to (m) are summarized in Table 3.1, and each different symbol in each graphic correspond to a different test run. Figures 3.6 and 3.8 present L_h/L_{drag} versus t/t_c over the entire duration of test runs and Figs. 3.7 and 3.9 present L_h/L_{drag} versus t/t_c from the beginning of test runs until $1.5t_c$.

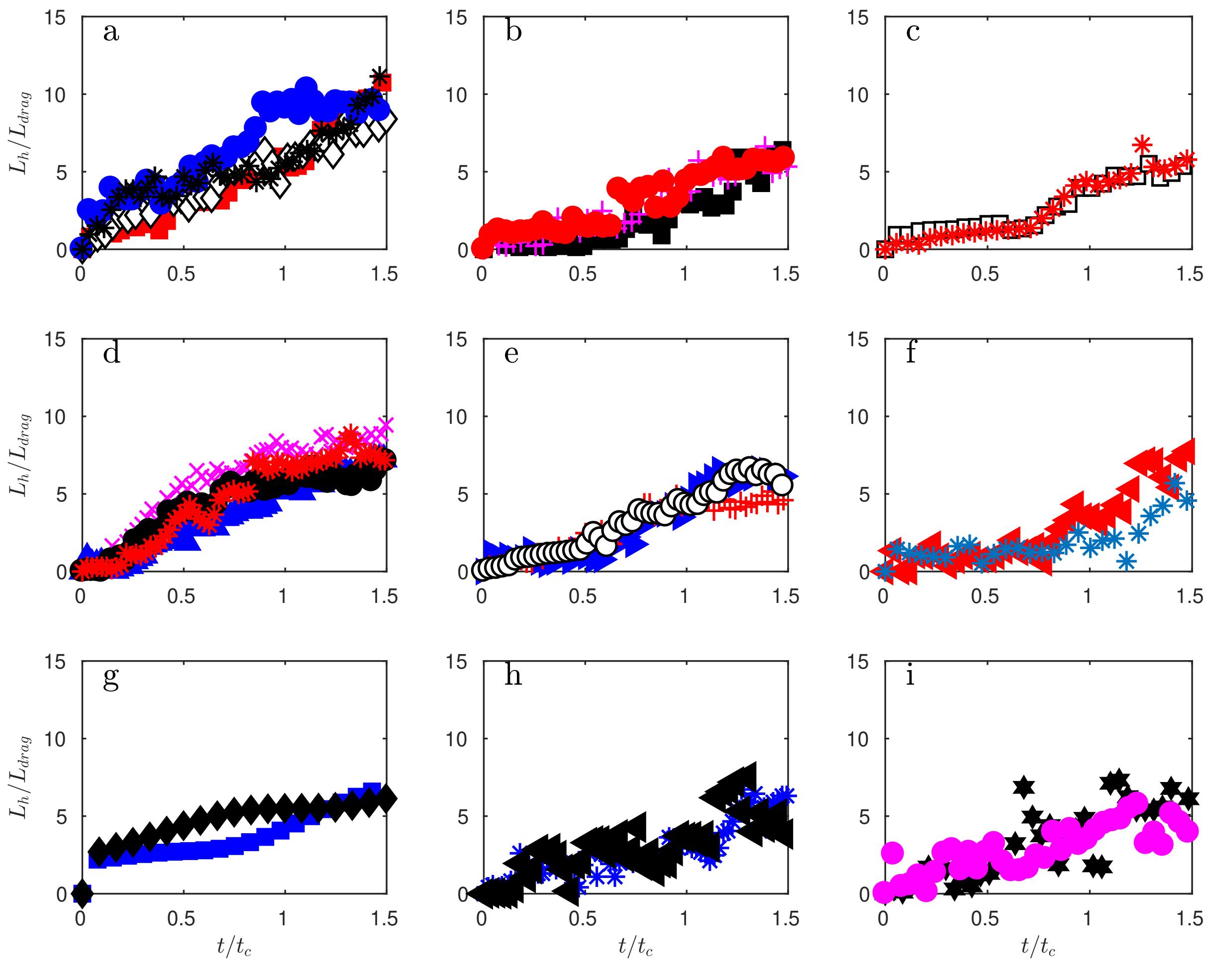

Fig. 3.7: Detail for $0 \leq\ t/t_c\ \leq 1.5$ of L_h/L_{drag} versus t/t_c for glass beads under different flow conditions. This figure shows every measurement points within this time interval. The cases (a) to (i) are summarized in Table 3.1, and each different symbol in each graphic corresponds to a different test run

.

By using L_{drag} as the characteristic length, $L_h/L_{drag} \geq 1$ is the minimum condition to search for the presence of a horn. For the present experiments, $2.5d \leq\ L_{drag}\ \leq 4.1d$, and, by considering a particle fraction of 50%, $L_h/L_{drag} \geq 1$ corresponds to structures consisting of 15 to 66 grains as the minimum structures forming a horn. In that case, the appearance of horns, and then the birth of a barchan from the initially conical heap, occurs at $t/t_c \approx 0.5$. From this moment, the horns continue to grow until $t/t_c \approx 2.5$, when they reach an equilibrium length. This is the instant when the barchan reaches its characteristic crescentic shape.

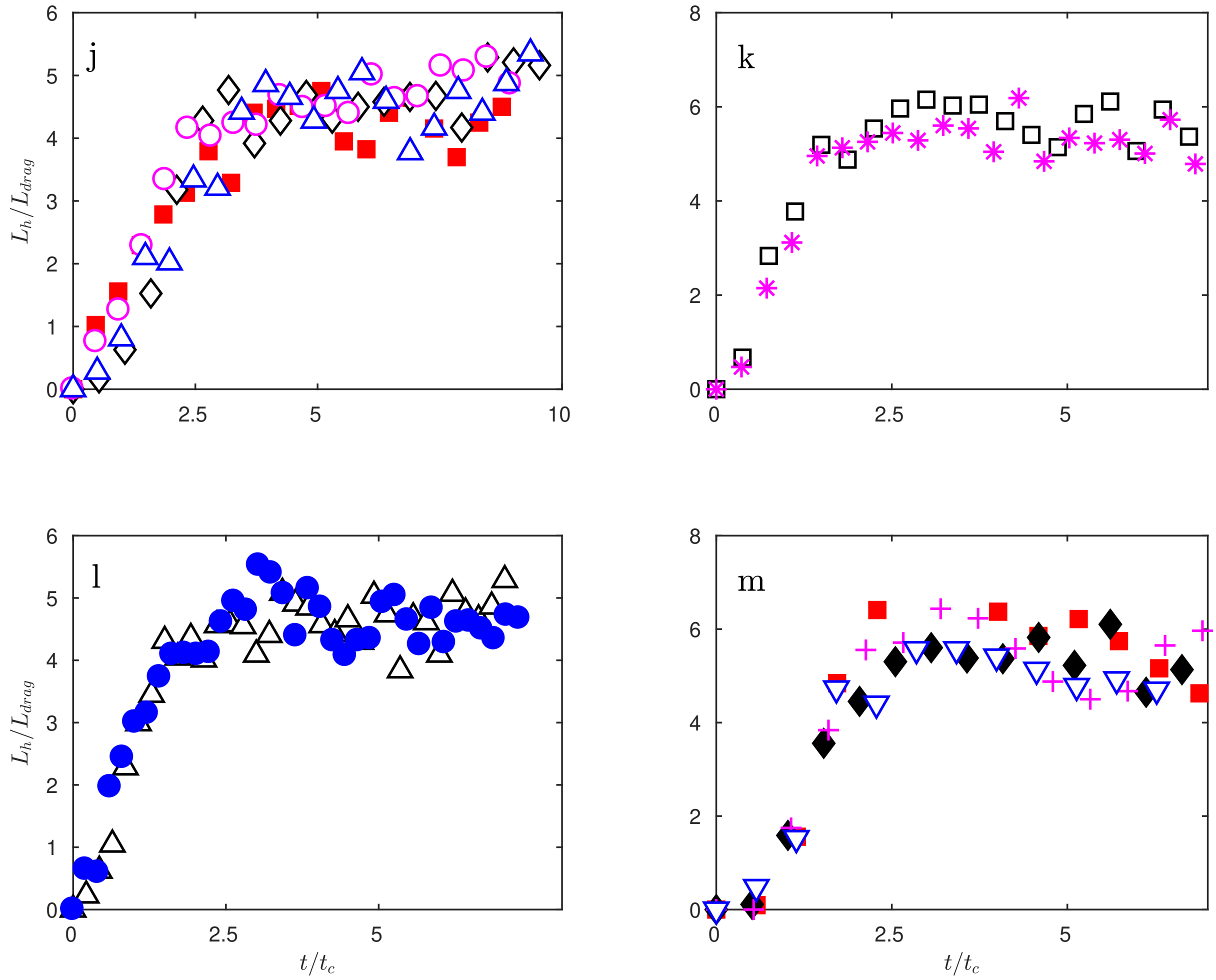

Fig. 3.8: L_h/L_{drag} versus t/t_c for zirconium beads under different flow conditions over the entire duration of test runs. This figure shows every n measurements for each experimental condition, where $5 \leq n \leq 15$. The cases (j) to (m) are summarized in Table 3.1, and each different symbol in each graphic corresponds to a different test run.

3.4 Chapter summary

In conclusion, the rise and equilibrium of a barchan dune is well described by the growing of its horns. From Figs. 3.6 to 3.9, we note that the time evolution of horns on a single dune presents a similar behavior in all cases, with the beginning of growth and the equilibrium shape occurring at the normalized times of approximately 0.5 and 2.5, respectively. Therefore, we pro-

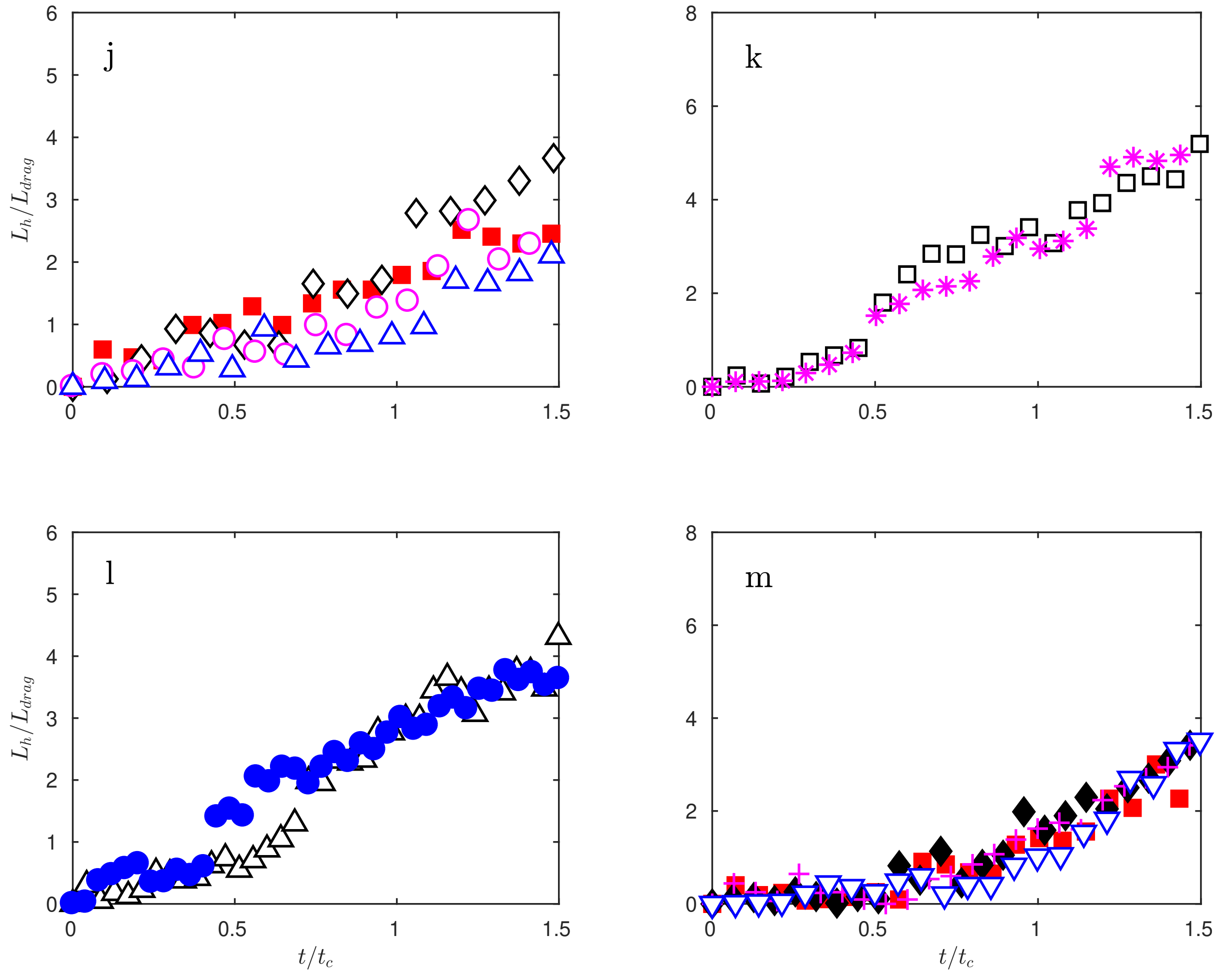

Fig. 3.9: Detail for $0 \leq t/t_c \leq 1.5$ of L_h/L_{drag} versus t/t_c for zirconium beads under different flow conditions. This figure shows every measurement points within this time interval. The cases (j) to (m) are summarized in Table 3.1, and each different symbol in each graphic corresponds to a different test run.

pose that the characteristic time given by Eq. 3.1 is the time scale for the beginning and growing of single barchan dunes. This time scale, obtained for single dunes under controlled conditions, is important to increase our knowledge about the formation of barchan dunes under more complex scenarios such as sand bars, large sand fields, sand fields over complex topographies, etc.

4 HORNS OF SUBAQUEOUS BARCHAN DUNES: A STUDY AT THE GRAIN SCALE†

The present chapter reports measurements of the growth of horns at the grain scale. We identified the trajectories of the grains that migrated to the horns and found that most of them came from upstream regions, with an average displacement of the order of the bedform size. In addition, we show that individual grains had transverse displacements by rolling and sliding that are not negligible, with many of them going around the dune. Finally, for these grains, we demonstrate that the distributions of transverse and streamwise components of velocities are well described by exponential functions, with the probability density functions of their magnitudes being similar to results obtained from previous studies on flat beds. Our results provide new insights into the physical mechanisms underlying the shape of barchan dunes.

4.1 Introduction

Sand dunes are the result of complex physical interactions between a fluid flow and an extended area of sand (Bagnold, 1941; Hersen *et al.*, 2002), their shape and dynamics depending on certain conditions such as the direction and strength of the flow and the available amount of sand. Under one-directional fluid flow with moderate shear stresses, so that bed load is the main mode of sand transport, barchans grow (Bagnold, 1941; Herrmann & Sauermann, 2000; Hersen, 2004). Barchan dunes are characterized by their crescentic shape with horns pointing downstream, and are frequently found in both nature and industry, some examples being barchans found in deserts, rivers, and petroleum pipelines, and even on the surface of Mars (Claudin & Andreotti, 2006; Parteli & Herrmann, 2007). Because of their robust shape on considerably different scales and the large number of environments where they are found, barchan dunes have been studied over the last century by a great number of scientists attracted by the problem. To list but a few examples: Bagnold (1941), Herrmann & Sauermann (2000), Sauermann *et al.* (2001), Hersen *et al.* (2002), Andreotti *et al.* (2002a,b), Kroy *et al.* (2002a,b), Kroy *et al.* (2005), Groh *et al.* (2008), Franklin & Charru (2011), Lämmel *et al.* (2012), Parteli *et al.* (2014), Khos-

† This chapter is based on C. A. Alvarez and E. M. Franklin, Phys. Rev. Lett. 121, 164503 (2018), and on C. A. Alvarez and E. M. Franklin, Phys. Rev. E 100, 042904 (2019). (Alvarez & Franklin, 2018b, 2019)

ronejad & Sotiropoulos (2017), Alvarez & Franklin (2017a, 2018a,b, 2019), Wang & Anderson (2018), and Gadal *et al.* (2019) have investigated the problem analytically, experimentally, or numerically. However, given the high complexity of grain-fluid interactions and the different scales involved, the problem is still open and several aspects need to be understood before a complete understanding is achieved.

Previous analytical studies, based on mechanistic approaches and stability analyses, increased our understanding of the growth and dynamics of barchan dunes, explaining, for example, the dependence of the barchan velocity on the inverse of its size (Bagnold, 1941) and that the fluid flow is the unstable mechanism for the growth of dunes (Engelund, 1970; Engelund & Fredsoe, 1982). Experimental data showed, among other things, that, indeed, these conclusions are true (Hersen *et al.*, 2002; Andreotti *et al.*, 2002a,b; Elbelrhiti *et al.*, 2005). However, despite the large number of experimental works available, only a few of them have presented measurements at the grain scale (Alvarez & Franklin, 2018b, 2019). Numerical works, for the great part, have used information from analytical and experimental studies to model granular matter as a continuum medium in order to allow the simulation of real dunes consisting of a large number of grains (Sauermann *et al.*, 2001; Herrmann & Sauermann, 2000; Kroy *et al.*, 2002a,b, 2005; Schwämmle & Herrmann, 2005; Parteli *et al.*, 2014). In those continuum models, given the lack of experimental measurements at the grain scale, the flow of grains is supposed to be mainly longitudinal, with some lateral diffusion. Although some recent numerical studies simulate the grains as a discrete medium by using, for example, the discrete element method (DEM) (Kidanemariam & Uhlmann, 2017), continuum models are still important to simulate large barchan fields, for which the number of grains does not allow discrete simulations at present. In continuum models, information such as typical trajectories and characteristic lengths and times are essential to fit adjustable constants. In the case of simulations employing the discrete element method, they are computationally expensive and comparisons with experiments are still necessary to validate their results.

Concerning the horns, there is a small number of studies devoted to their growth and stability. Khosronejad & Sotiropoulos (2017) presented a numerical investigation of the instabilities on the surface of horns of existing barchans. They found that transverse waves propagating over the horns give rise to new barchans, and that their amplitudes and wavelengths are related.

Hersen (2004), and Schwämmle & Herrmann (2005) investigated numerically the formation of aeolian barchans from different initial shapes using continuum models, in which lateral diffusion was included to account for part of the transverse displacements of grains. According to Hersen (2004), the physical origin of the lateral diffusion included in these models is reptation caused by the impact of salting grains. In particular, Hersen (2004) proposed that aeolian barchans can be modeled as longitudinal two-dimensional slices that exchange mass among them mainly by lateral diffusion, but also by air entrainment and slope effects. Within this picture, the celerity of each slice varying with the inverse of its size (Bagnold, 1941; Kroy *et al.*, 2002b; Andreotti *et al.*, 2002a), horns grow mainly with grains originally in the lateral flanks of the initial heap. Although this description is generally accepted for aeolian dunes, it has never been experimentally verified in the aeolian case. In the subaqueous case, Alvarez & Franklin (2018b) showed a different picture, described in the next paragraph. In the **Chapter 3**, we showed that horns grow from an initial instant, given by $0.5t_c$, until they reach a final length at $2.5t_c$, where t_c is a characteristic time for the displacement of barchans, computed as the length of the bedform divided by its celerity.

Few experimental measurements at the grain scale are reported for subaqueous bed load. For plane granular beds, Seizilles *et al.* (2014) investigated bed load under laminar flows; and Lajeunesse *et al.* (2010), and Penteado & Franklin (2016) investigated the turbulent case. As common results, these works showed that the displacements of individual grains are intermittent and that distributions of grain velocities can be adjusted by exponential functions. Lajeunesse *et al.* (2010), and Penteado & Franklin (2016) showed that the streamwise velocities scale with the excess of shear stress, and that transverse velocities are distributed around a zero mean value. Seizilles *et al.* (2014) proposed that transverse displacements on flat beds are caused by a Fickian diffusion mechanism with a characteristic length of 0.030d, where d is the mean grain diameter. In a recent paper (Alvarez & Franklin, 2018b), we investigated experimentally bed load during the growth of barchans from initial piles of conical shape. We measured the trajectories of grains migrating to the growing horns and showed that most of them came from upstream regions on the periphery of the initial pile, with transverse displacements by rolling and sliding that were considerable. This evidence diverges from the general description for aeolian dunes, where transverse displacements are due mainly to the diffusive effect of reptons, and therefore, horns are expected to grow mainly with grains originally in the lateral flanks of the initially conical pile.

Figure 4.1 shows top views of an initially conical heap deformed into a crescentic shape by the water flow, where R is the radius of the initial pile. It was defined as the maximum radius with origin at the centroid and that does not contain void regions. The experimental conditions and times are described in the figure caption.

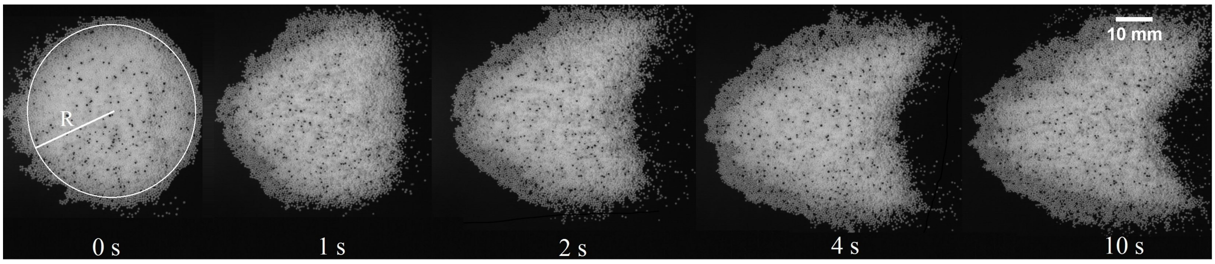

Fig. 4.1: Top views of an initially conical heap deformed by the water flow at different times (shown below each frame). The water flow is from left to right, R is the radius of the initial pile, and black spots are the tracers. Re = 1.82×10^4 and the heap initial mass was 6.2 g.

In this chapter, we present a thorough investigation of the trajectories of grains going to horns of subaqueous barchans. In the present experiments, subaqueous dunes were formed from initial piles of conical shape, and we measured the trajectories of grains going to horns for the cases of both evolving dunes (growing horns), $0.5t_c \leq t \leq 2.5t_c$, and developed dunes (stable horns), $t > 2.5t_c$. The present results show that the general assertions for aeolian dunes that horns grow and are sustained mainly by grains originally in the transverse extremities of the bedform do not apply for subaqueous barchans. Furthermore, we show that the distributions of transverse and streamwise components of grain velocities are well described by exponential functions, and we find the typical residence time and traveled distance of moving grains whose initial positions were on the horns. Our results change the way in which horns formation and stability and bed load are explained for subaqueous barchans.

4.2 Experimental setup and methods

We used the same experimental device presented in the **Chapter 3**, which consisted basically of a water reservoir, centrifugal pumps, a 5-m-long closed-conduit channel, a settling tank, and a return line. The channel, made of transparent material, had a rectangular cross section 160 mm wide by 50 mm high (2δ = 50 mm), and the test section started 3 m (40 hydraulic diameters) downstream of the channel entrance. Prior to each test, with the channel previously filled with water, controlled grains were poured into the test section, forming a single conical pile at the bottom wall. Afterward, for each test run, a turbulent water flow was imposed, deforming the conical pile into a barchan dune. With this procedure, each experiment concerned one single barchan that loosed grains by its horns, decreasing slowly in size while migrating. Figure 4.2(a) presents a photograph of the experimental setup displaying, among other elements, the test section and the initial pile. Figure 4.2(b) shows a top view of an initially conical heap, where R is the radius of the initial pile, and r_0 is the initial position of the pile centroid.

The tests were performed with tap water at temperatures between 24 and 26 ^{o}C and round glass beads (density of grains ρ_s = 2500 kg/m^3 and bulk density of 1500 kg/m^3) with 0.15 mm $\leq$ d $\leq$ 0.25 mm and 0.40 mm $\leq$ d $\leq$ 0.60 mm. In order to facilitate the tracking of moving grains, 2$\%$ of them were tracers (grains of different color but the same density, diameter, and surface characteristics as the other grains). The cross-sectional mean velocities of water U were 0.243, 0.294, and 0.364 m/s, corresponding to Reynolds numbers based on the channel height Re = $\rho U 2\delta/\mu$ of 1.21×10^4, 1.47×10^4, and 1.82×10^4, respectively, where ρ is the density and μ the dynamic viscosity of the fluid. The shear velocities on the channel walls u_* were computed from the velocity profiles measured with a two-dimensional particle image velocimetry device (2D-PIV), and were found to follow the Blasius correlation (Schlichting, 2000). Using the hydraulic diameter of the channel, they correspond to 0.0141, 0.0168, and 0.0202 m/s for the three flow rates employed. The initial heaps were formed with 6.2 and 10.3 g of glass beads, corresponding to initial volumes of 4.1 and 6.9 cm^3, and to R values of 2.6 and 3.2 cm, respectively.

Table 4.1 summarizes the tested conditions, for which we performed between three and five independent runs for each experimental condition. In Table 4.1, the column dune condition refers to whether the measurements concern an evolving or a developed barchan. The table lists also the mass of the initial pile m_0, the grain diameter d, the channel Reynolds number Re, the Reynolds number at the grain scale Re_* = $\rho u_* d/\mu$, and the Shields number $\theta = (\rho u_*^2)/[(\rho_s - \rho)gd]$.

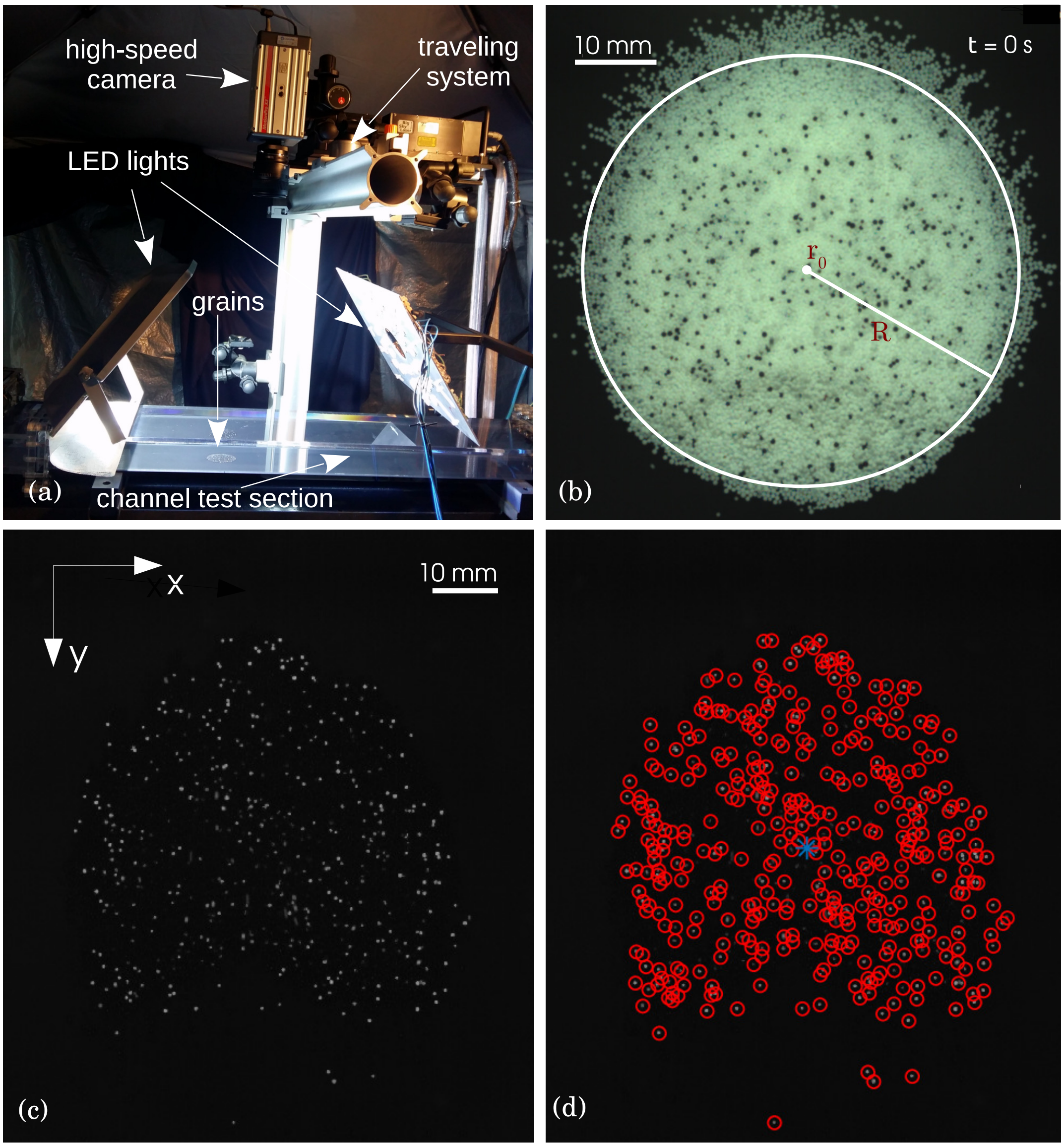

Fig. 4.2: Experimental setup, definition of geometrical parameters, and particle detection. (a) Photograph of the experimental setup showing the test section, high-speed camera, traveling system, light-emitting diode lights, and grains placed on the bottom wall of the channel. (b) Top view of an initially conical heap of radius R at time t= 0 s, where r_0 is the initial position of the pile centroid and black spots are tracers. (c) Top-view image of a dune in gray scale showing the tracers. Flow is from top to bottom. (d) Example of a treated image showing the detected particles. Red circles are surrounding the tracers identified in (c), and the asterisk corresponds to the instantaneous position of the dune centroid. Re = 1.82 $\times$ 10^4 and the heap initial mass was 6.2 g.

A high-speed camera of complementary metal-oxide-semiconductor type (CMOS) was placed above the channel to record the bed evolution [Fig. 4.2(a)]. We used a camera with a spatial resolution of 1280 $\times$ 1024 px at frequencies up to 1000 Hz, controlled by a computer. In our tests, we set the frequency to values within 50 and 200 Hz, depending on the average velocity of grains, and we used a lens of 60-mm focal distance and F2.8 maximum aperture.

Table 4.1: Label of tested cases, grain diameter d, dune condition during measurements, channel Reynolds number Re, Reynolds number at the grain scale Re_*, Shields number θ, and mass of the initial heap m_0.

Case $\cdots$	d (mm)	Dune condition $\cdots$	Re $\cdots$	Re_* $\cdots$	θ $\cdots$	m_0 (g)
a	0.15 - 0.25	Evolving	1.21×10^4	3	0.07	6.2
b	0.15 - 0.25	Evolving	1.47×10^4	3	0.10	6.2
c	0.15 - 0.25	Evolving	1.82×10^4	4	0.14	6.2
d	0.40 - 0.60	Evolving	1.21×10^4	7	0.03	6.2
e	0.40 - 0.60	Evolving	1.47×10^4	8	0.04	6.2
f	0.40 - 0.60	Evolving	1.82×10^4	10	0.06	6.2
g	0.40 - 0.60	Evolving	1.21×10^4	7	0.03	10.3
h	0.40 - 0.60	Evolving	1.47×10^4	8	0.04	10.3
i	0.40 - 0.60	Evolving	1.82×10^4	10	0.06	10.3
j	0.15 - 0.25	Developed	1.21×10^4	3	0.07	6.2
k	0.15 - 0.25	Developed	1.47×10^4	3	0.10	6.2
l	0.15 - 0.25	Developed	1.82×10^4	4	0.14	6.2
m	0.40 - 0.60	Developed	1.21×10^4	7	0.03	6.2
n	0.40 - 0.60	Developed	1.47×10^4	8	0.04	6.2
o	0.40 - 0.60	Developed	1.82×10^4	10	0.06	6.2
p	0.40 - 0.60	Developed	1.21×10^4	7	0.03	10.3
q	0.40 - 0.60	Developed	1.47×10^4	8	0.04	10.3
r	0.40 - 0.60	Developed	1.82×10^4	10	0.06	10.3

Lamps of light-emitting diodes were branched to a continuous current source in order to supply the required light while avoiding beating between the camera and the light frequencies. Prior to the beginning of tests, a calibration procedure which consisted of taking one picture from a scale placed in the channel (filled with water) was performed, allowing the conversion from pixels to a physical system of units. We set the region of interest to 800 px $\times$ 1024 px to better fit a field of view of 80.0 mm $\times$ 102.4 mm; therefore, the area covered by each grain in the acquired images varied within 2 to 28 px. Once the images were obtained, the centroids of tracers and those of barchans were identified [Figs. 4.2(c), 4.2(d)] with an image processing code written in the course of this work based on Alvarez (2016); Alvarez & Franklin (2017b) and Kelley & Ouellette (2011). To compute the trajectories of tracers, the code uses a particle tracking velocimetry approach (PTV) that follows each centroid along time.

4.3 Results and discussion

4.3.1 Pathlines of migrating grains

Figure 4.3(a) shows the pathlines of moving tracers during the growth of a barchan dune from an initial conical pile consisting of 0.15 mm $\leq d \leq$ 0.25 mm glass beads. The initial mass of the pile, m_0, was 6.2 g, which corresponded to R = 2.6 cm. The abscissa and ordinate correspond, respectively, to the transverse and streamwise coordinates, x and y, normalized by R. In Fig. 4.3, the dashed black circle displays the initial pile and the color of pathlines varies according to the position of the pile centroid, which moves while the barchan grows. In this way, the blue (upper) and red (lower) pathlines correspond to the initial and final positions of the pile centroid, respectively, the scaling bar showing the values of $r_c - r_0$ normalized by R, where r_c is the instantaneous position of the pile centroid and r_0 the initial one (see Appendix B for some trajectories superposed with a photograph of the barchan). Figure 4.3(b) shows the pathlines of the tracers that migrated to horns during their growth (see Appendix B for trajectories of other test runs concerning the 0.15 mm $\leq d \leq$ 0.25 mm beads).

Figure 4.4(a) shows the pathlines of moving tracers during the growth of a barchan dune from an initial conical pile consisting of 0.40 mm $\leq d \leq$ 0.60 mm glass beads. The initial mass of the pile, m_0, was 6.2 g, which corresponded to R = 2.6 cm. Figure 4.4(b) shows the pathlines of the tracers that migrated to horns during their growth (see Appendix B for trajectories of other test runs concerning the 0.40 mm $\leq d \leq$ 0.60 mm beads). From Figs. 4.3 and 4.4 we note that grains experience significant transverse displacements, many of them describing circular paths while migrating toward the horns. It is noticeable that a significant part of grains going to horns was originally in the upstream region of the pile periphery.

In addition to evolving barchans, we address the dynamics of grains migrating to horns after the dune has reached its crescentic shape. For that, we identified and tracked the tracers from the moment the dune centroid reached a coordinate $1.0R$ downstream of its origin, which means that the dune had migrated a distance equivalent to its size, and therefore, all grains within the dune had been displaced.

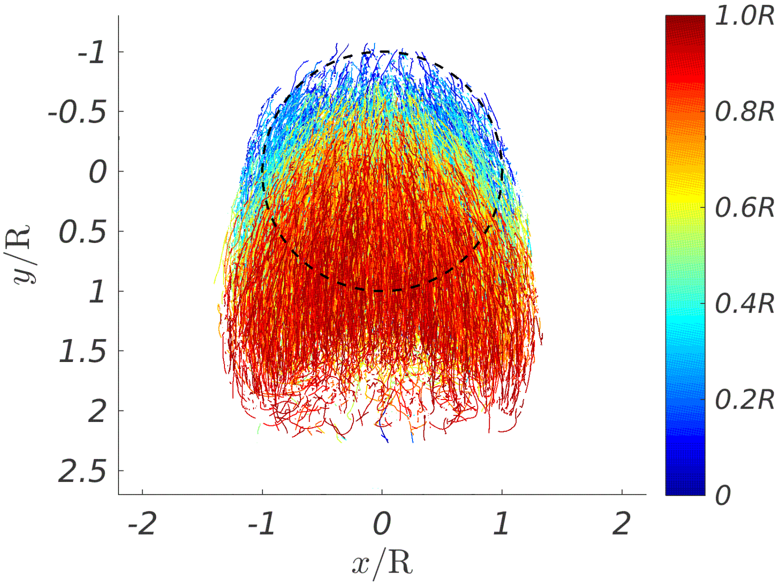

(a)

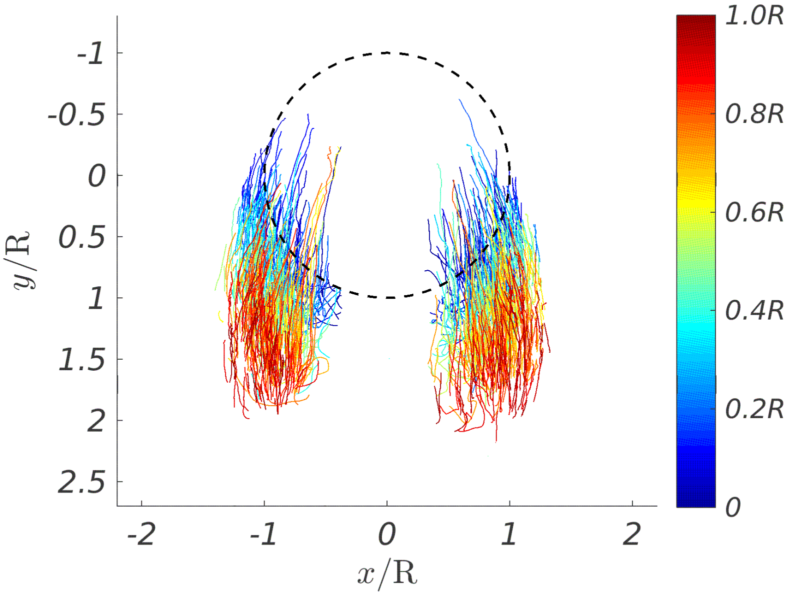

(b)

Fig. 4.3: Pathlines of tracers over an evolving dune made of 0.15 mm $\leq d \leq$ 0.25 mm glass beads. (a) All moving tracers during the growth of a barchan dune. (b) Tracers that migrated to horns during the growth of the barchan dune. The dashed black circle represents the initial pile of radius R, and the scaling bar shows the values of $r_c - r_0$ normalized by R. Water flow is from top to bottom, Re = 1.82 $\times 10^4$, m_0 = 6.2 g, and R = 2.6 cm.

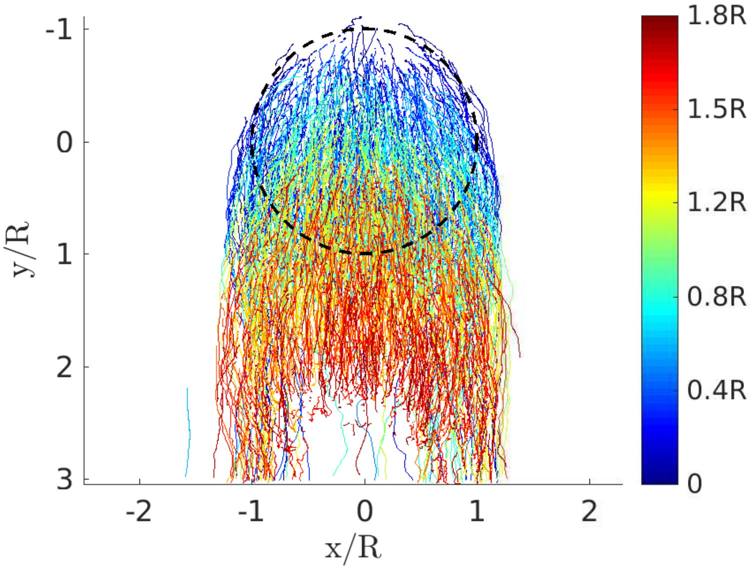

(a)

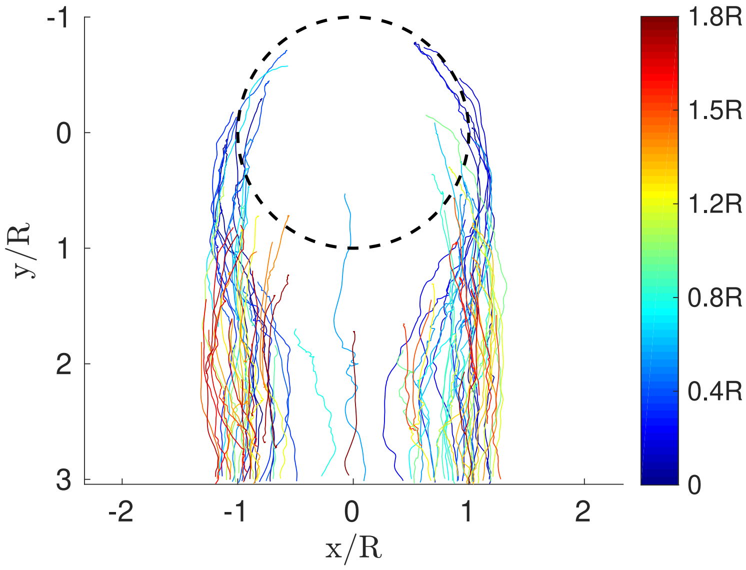

(b)

Fig. 4.4: Pathlines of tracers over an evolving dune made of 0.40 mm $\leq$ d $\leq$ 0.60 mm glass beads. (a) All moving tracers during the growth of a barchan dune. (b) Tracers that migrated to horns during the growth of the barchan dune. The dashed black circle represents the initial pile of radius R, and the scaling bar shows the values of $r_c - r_0$ normalized by R. Water flow is from top to bottom, Re = 1.82 $\times 10^4$, m_0 = 6.2 g, and R = 2.6 cm.

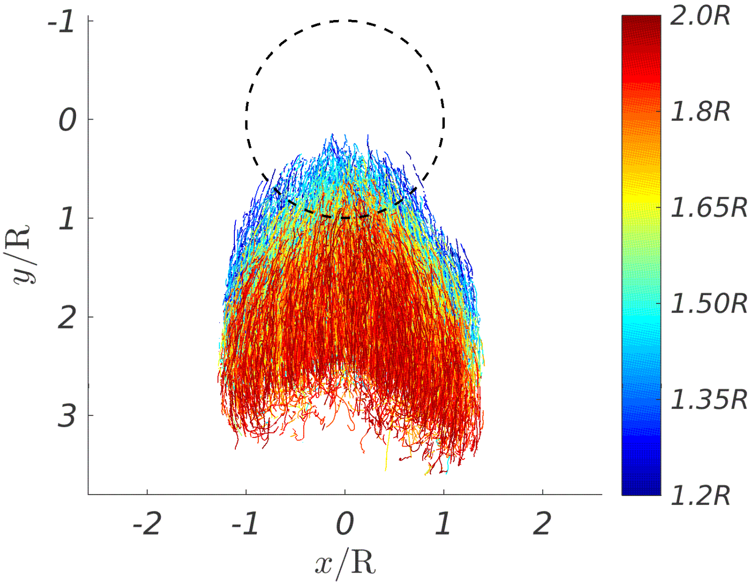

(a)

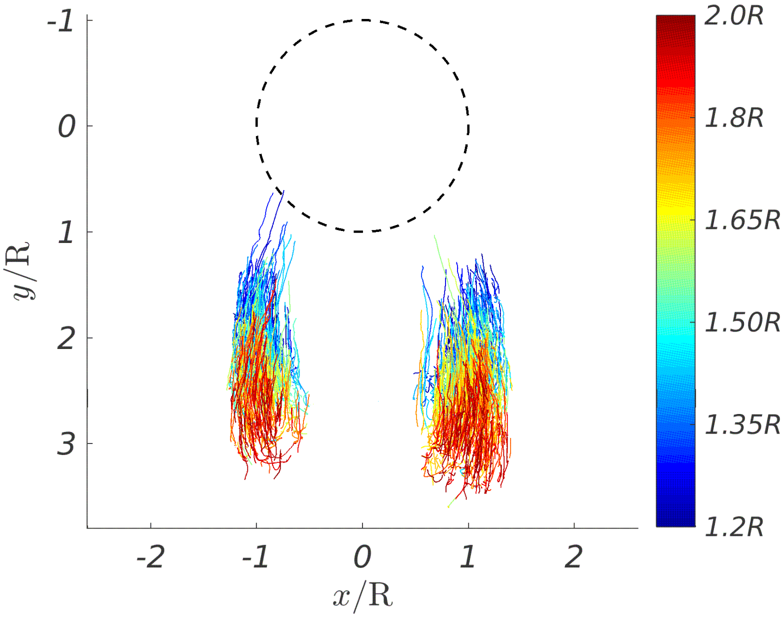

(b)

Fig. 4.5: Pathlines of tracers over a developed dune made of 0.15 mm $\leq d \leq$ 0.25 mm glass beads. (a) All moving tracers over the barchan dune. (b) Tracers that migrated to the barchan horns. The dashed black circle represents the initial pile of radius R, and the scaling bar shows the values of $r_c - r_0$ normalized by R. Water flow is from top to bottom, Re = 1.82 $\times 10^4$, m_0 = 6.2 g, and R = 2.6 cm.

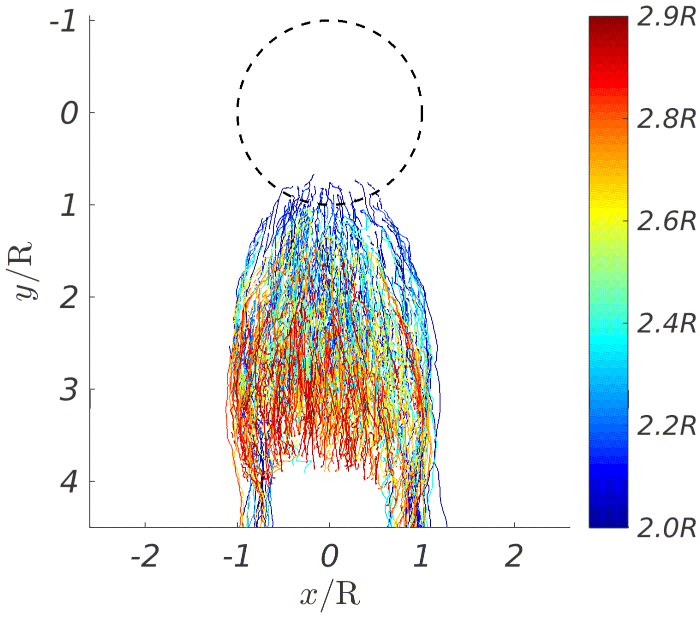

(a)

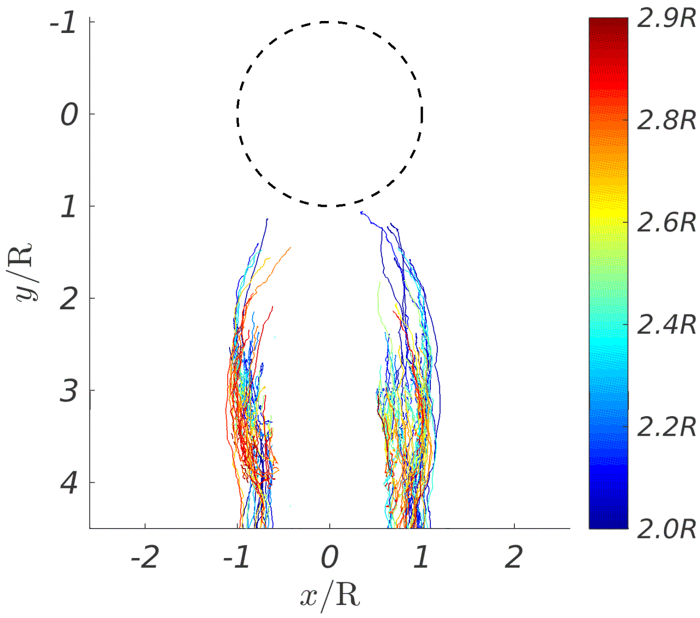

(b)

Fig. 4.6: Pathlines of tracers over a developed dune made of 0.40 mm $\leq\ d\ \leq$ 0.60 mm glass beads. a) All moving tracers over the barchan dune. b) Tracers that migrated to the barchan horns. The dashed black circle represents the initial pile of radius R, and the scaling bar shows the values of $r_c - r_0$ normalized by R. Water flow is from top to bottom, Re = 1.47 $\times 10^4$, m_0 = 6.2 g, and R = 2.6 cm.

Figure 4.5 shows the pathlines of moving tracers over a grown barchan consisting of 0.15 mm $\leq\ d\ \leq$ 0.25 mm glass beads. In this figure, m_0 = 6.2 g, which corresponds to R = 2.6 cm, and the colors and legends are the same as in Fig. 4.3. Figure 4.5(a) presents the pathlines of all moving tracers, while Fig. 4.5(b) presents the pathlines of traces migrating to the horns. Figure 4.6 shows the developed case for m_0 = 6.2 g, 0.40 mm $\leq\ d\ \leq$ 0.60 mm, and Re = 1.47 $\times 10^4$, and the pathlines of the other test runs are available in the Appendix B.

In Figs. 4.5 and 4.6 we observe a behavior similar to that observed for growing barchans, i.e., many of the moving grains describe circular paths while migrating toward the horns, which implies local transverse components that are significant. These grains come from regions upstream of the dune centroid, moving around the central region of the barchan before reaching the horns. We note also small asymmetries in Figs. 4.5 and 4.6, which are due to dispersions in our experiments.

We compare next the mean distance L_{mean} traveled by tracers migrating to horns in the evolving and developed cases. The mean distance was obtained by computing the total distance traveled by each tracer that migrated to the horns, and then taking the arithmetic mean for each tested case. By considering the cases listed in Table 4.1, we found for the evolving barchans

$$14 < L_{mean}/L_{drag} < 30 \tag{4.1}$$

for the 6.2-g piles and

$$18 < L_{mean}/L_{drag} < 22 \tag{4.2}$$

for the 10.3-g piles, while for the developed barchans we found

$$14 < L_{mean}/L_{drag} < 28 \tag{4.3}$$

for the 6.2-g piles and

$$22 < L_{mean}/L_{drag} < 30 \tag{4.4}$$

for the 10.3-g piles, where $L_{drag} = (\rho_s/\rho)d$ is an inertial length scaling with the length for sand flux saturation (Hersen *et al.*, 2002). The normalized traveled distances are similar for both evolving and developed barchans, corroborating the similar behavior observed from pathlines plotted in Figs. 4.3 to 4.6 and in the Appendix B. Their values are three orders of magnitude greater than the diffusion length ℓ_d proposed by Seizilles *et al.* (2014) ($\ell_d/L_{drag} \approx 0.01$).

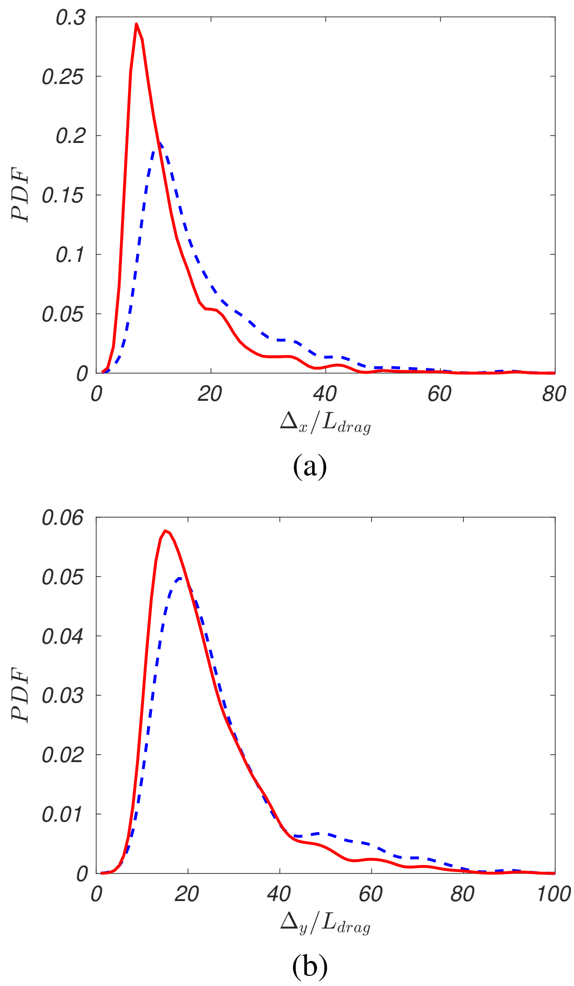

Fig. 4.7: PDFs of the total (a) transverse and (b) longitudinal distances, Δ_x and Δ_y, respectively, normalized by L_{drag} for case q in Table 4.1. Dashed blue lines correspond to grains that migrated to the horns and solid red lines to all other grains.

We computed also the total transverse (Δ_x) and longitudinal (Δ_y) distances traveled by the tracers that migrated to horns as well as by the other tracers, in both the evolving and the developed cases. Probability density functions (PDFs) in Figs. 4.7(a) and 4.7(b) show, respectively, Δ_x/L_{drag} and Δ_y/L_{drag} for case q in Table 4.1, where the dashed blue lines correspond to the grains that migrated to the horns, and solid red lines to all the other grains. We observe a significant transverse component in the movement of grains, with higher values for grains migrating to horns in comparison to the others. By considering the most probable values of distributions for the cases listed in Table 4.1, we found $10 \leq \Delta_x/L_{drag} \leq 12$ for the grains migrating to horns, three orders of magnitude greater than the diffusion length ℓ_d proposed by Seizilles *et al.* (2014), and $6 \leq \Delta_x/L_{drag} \leq 8$ for all the other grains. We found also that the ratio between the transverse and the longitudinal distances, Δ_x/Δ_y, is around 0.5 for the grains migrating to horns and 0.4 for all the other grains. These values corroborate the importance of transverse movements in the subaqueous case.

4.3.2 Origin of grains migrating to horns

A suitable method for identifying the locations whence the grains migrate to the horns is the use of radial and angular coordinates with the origin at the dune centroid. For this, we identified the initial position of each tracer that migrated to the horns in polar coordinates $(|r_1 - r_c|, \phi)$, where r_1 is the initial position of the tracer, r_c is the instantaneous position of the dune centroid, and ϕ is the angle with respect to the transverse direction. With the initial positions, we computed the probability density functions and frequencies of occurrence for all tested conditions.

Figure 4.8 shows the probability density functions of the initial position of grains migrating to horns as functions of the normalized radial position $|r_1 - r_c|/R$ and Fig. 4.9 shows their frequencies of occurrence with respect to the transverse direction, for all tested conditions listed in Table 4.1, corresponding then to both evolving and developed barchans. For cases j to r, the centroid position is as shown in Fig. 4.2(d), while for cases a to i, the centroid is originally the center of the initial circle (horizontal projection of the initial pile), with small relative changes from the beginning to the end of the tests as the bedform evolves. The PDFs were computed using a kernel smoothing function (Bowman & Azzalini, 1997) in Fig. 4.8 and the water flow direction is 270° in Fig. 4.9.

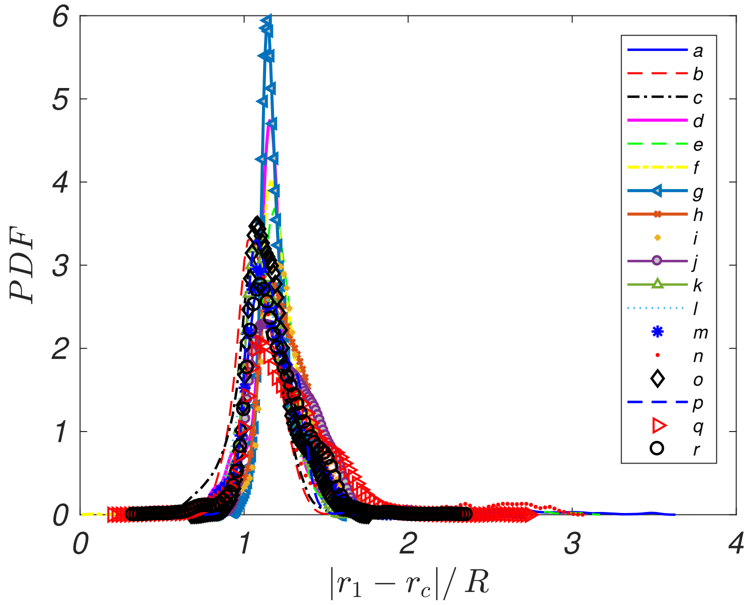

Fig. 4.8: PDFs of the original position of the tracers that migrated to horns for both evolving and developed dunes. Cases listed in the key are presented in Table 4.1.

Regardless of the dune condition (evolving or developed), initial mass of the pile, grain size, and water flow rate, many of the grains going to horns come from upstream regions on the periphery of the pile or dune, $|r_1 - r_c|/R > 1$ and $15^\circ \leq \phi \leq 70^\circ$ and $120^\circ \leq \phi \leq 170^\circ$. We note that asymmetries in the plots in Fig. 4.9 are due to dispersions in our experiments.

Figure 4.9 shows that some of the grains migrating to horns have their origin at the lateral flanks ($\phi \approx 0^\circ$ and $\phi \approx 180^\circ$), with lower frequencies of occurrence, however, than grains that originate at upstream positions. Another portion of the grains that were originally at the lateral flanks is carried away downstream from the dune by the water flow, as can be seen in the movies available in the Supplemental Material of Alvarez & Franklin (2019). We note also in these movies a region consisting of a monolayer of grains on the periphery of the bedform, with the exceptions of the lee side and inner part of the horns. Because most of the grains migrating to horns come from upstream regions on the periphery of the dune, many of them thus come from the monolayer region.

Based on the present data, we can conclude that, within the range of parameters of the present study, grains going to the horns of both evolving and developed subaqueous barchans describe circular paths while moving by rolling and sliding. This is different from the picture reported for the aeolian case, where the bed load is characterized by salting grains that effec-

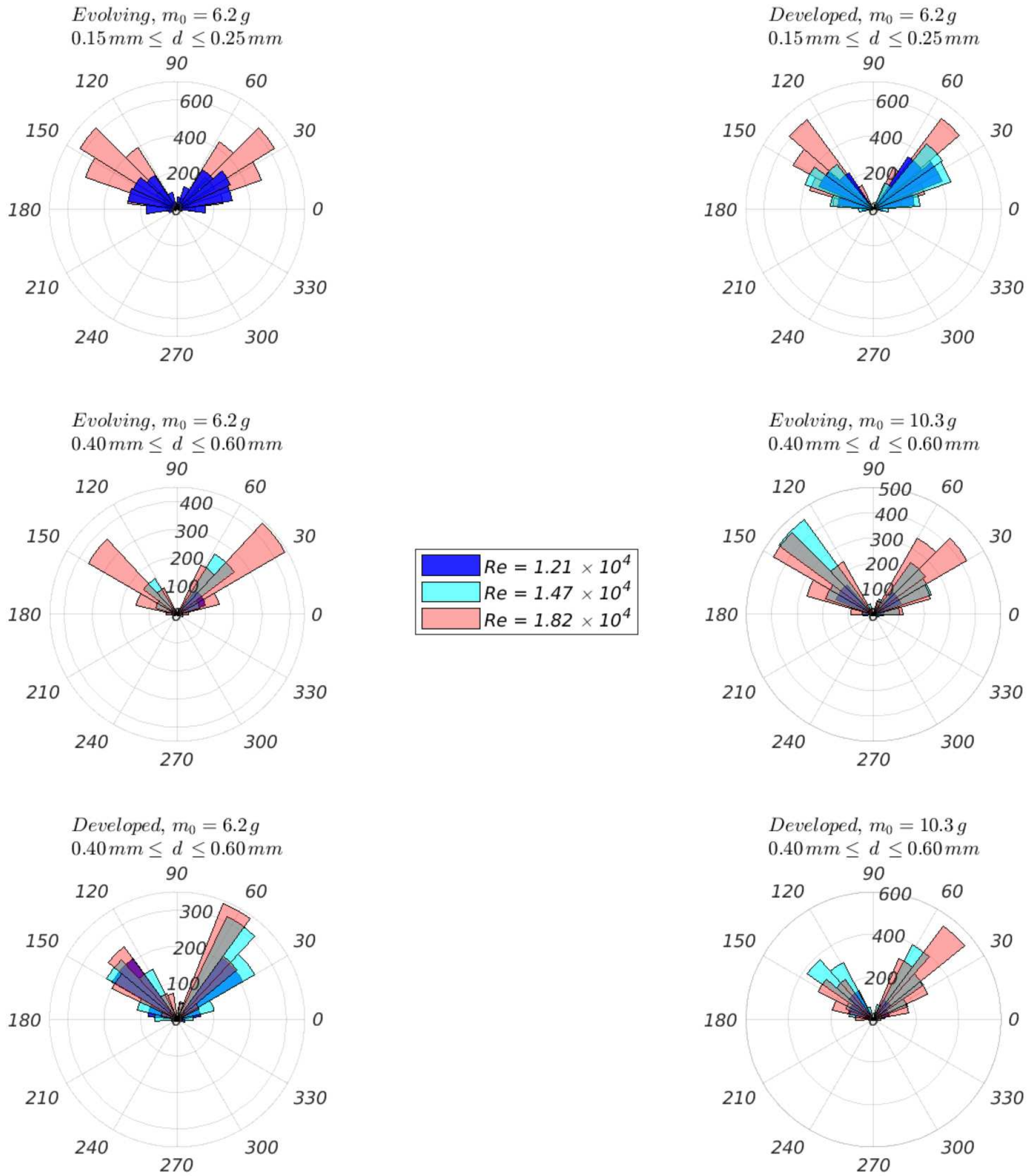

Fig. 4.9: Frequencies of occurrence of the initial position of tracers migrating to the horns as a function of the angle with respect to the transverse direction. The water flow direction is 270°. The tips of horns point to angles of approximately 240° and 300°. All cases listed in Table 4.1 are shown.

tuate ballistic flights in the wind direction, impacting in many instances onto the dune surface (Hersen, 2004; Schwämmle & Herrmann, 2005; Andreotti *et al.*, 2006). In the aeolian case, horns would form from grains originating at the lateral flanks of the initial pile and, thereafter, would be maintained by grains coming from the lateral flanks of the developed barchan, but trajectories of grains and horns formation in the aeolian case remain to be investigated.

4.3.3 Velocity distributions of grains migrating to horns

We computed the instantaneous transverse and streamwise velocities, V_x and V_y, for all tracers that migrated to the horns. The velocities were computed by time differentiation of trajectories, based on algorithms described in Kelley & Ouellette (2011). The number of moving particles varies with the water flow rate and the inverse of the grain diameter; therefore, the statistics for θ = 0.14 take into account a larger number of grains than those for smaller values of θ. However, the velocity distributions that we obtained showed the same behavior for all tested conditions.

Figures 4.10(a) and 4.10(b) present PDFs of the transverse velocities of tracers migrating to the barchan horns for cases n and b (Table 4.1), respectively. These PDFs are roughly symmetrical about V_x = 0 and could be fitted by a Gaussian function. However, the distributions are too peaked to be adjusted in this manner and are better fitted by an exponential law. We note that the exponential fitting is rather poor for the higher velocities, as shown in the insets in Figs. 4.10(a) and 4.10(b), but the region of poor fitting corresponds to lower probabilities, of the order of 10^{-3}. The PDFs obtained for the other cases are similar.

The distributions of the streamwise velocities of the grains migrating to horns have some small negative values corresponding to grains trapped in the recirculation region, which affects some grains at the inner lateral flank of the horns (see Supplemental Material of Alvarez & Franklin (2019) for movies showing the displacements of grains). Because the negative values have small magnitudes and very low probabilities, we did not consider them in our PDFs. Figures 4.11(a) and 4.11(b) present PDFs of the V_y of tracers migrating to the barchan horns for cases n and b (Table 4.1), respectively. As for V_x, the distributions of V_y can be fitted by an exponential law, noting that fittings are rather poor for the higher velocities, as shown in the insets in Figs. 4.11(a) and 4.11(b). Again, as in the case for V_x, the region of poor fitting corresponds to lower probabilities, of the orders of 10^{-4} and 10^{-3}, and the PDFs obtained for the other cases are similar.

We note that the PDFs of velocity distributions that we have obtained by considering only the grains going to horns resemble those obtained by Lajeunesse *et al.* (2010), Roseberry *et al.* (2012), Seizilles *et al.* (2014), and Heyman *et al.* (2015) for bed load over flat beds, even if for the latter case the transverse displacement of grains is only of a diffusive nature.

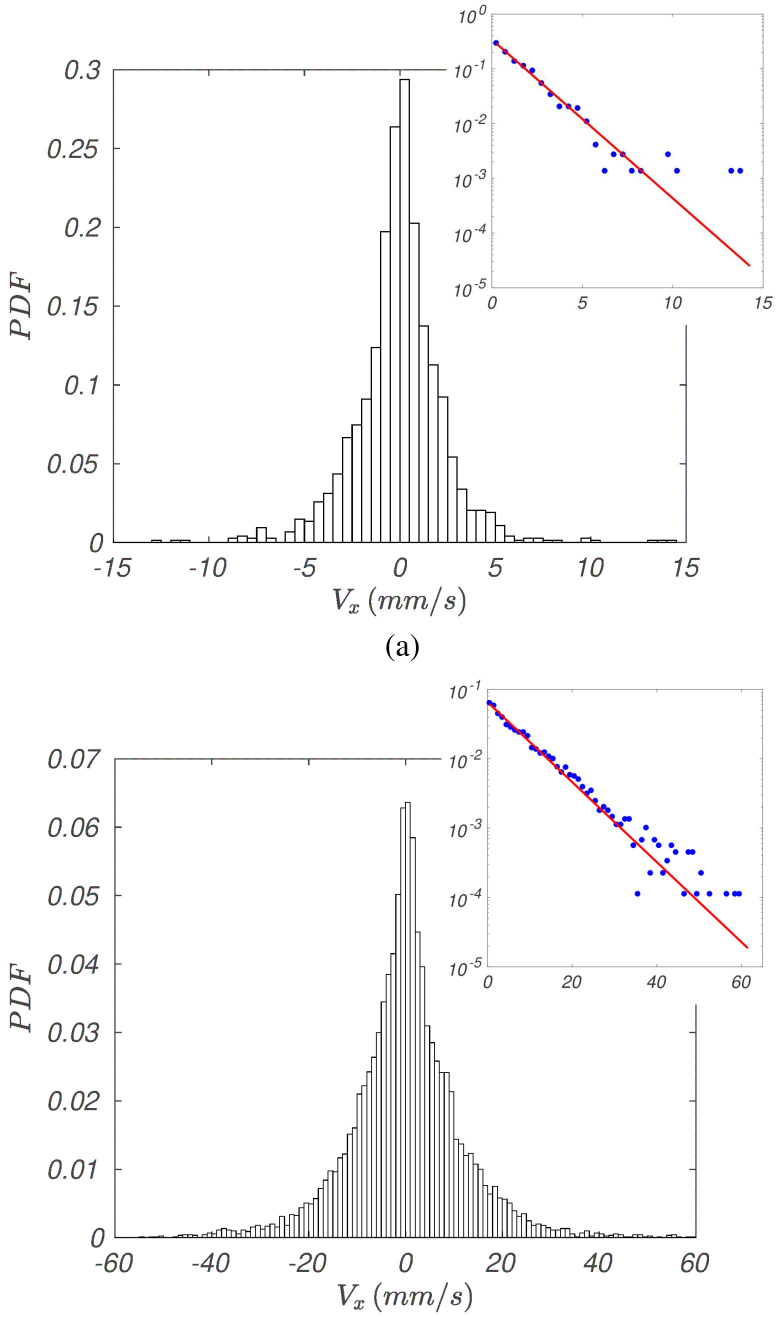

(b)

Fig. 4.10: PDFs of transverse velocities V_x of tracers migrating to horns. Insets; Semilog plots of PDFs for $V_x > 0$, where the solid line corresponds to a straight-line fit for this part of the distribution. (a) Case n and (b) case b from Table 4.1.

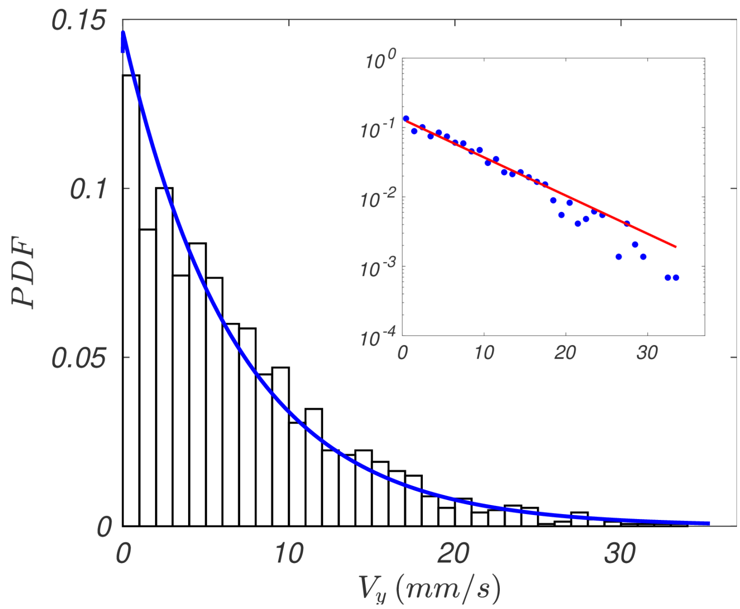

(a)

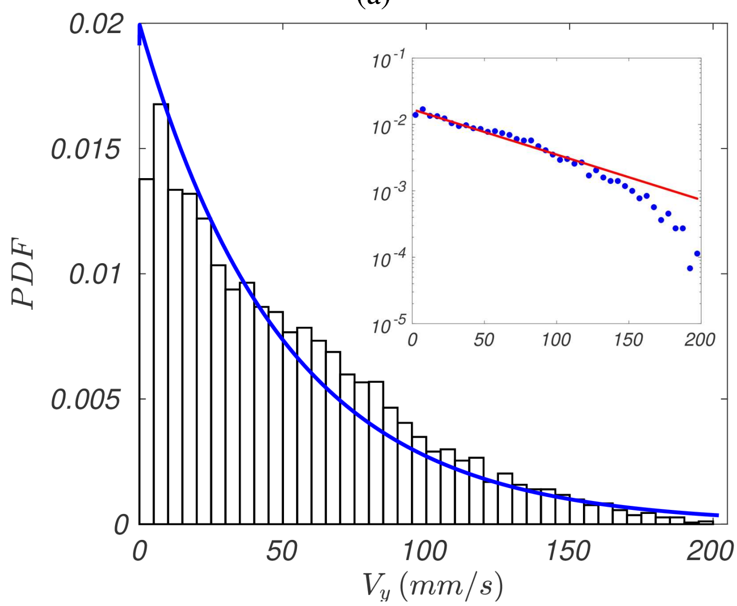

(b)

Fig. 4.11: PDFs of streamwise velocities V_y of tracers migrating to horns. Insets: Semilog plots of PDFs, where the solid line corresponds to a straight-line fit. (a) Case n and (b) case b from Table 4.1.

4.3.4 Residence time of moving grains leaving the horns of developed barchans

We investigate next the residence time of moving grains whose initial positions were on the horns of developed barchans. For this, we computed the time interval t that each tracer took to leave the horns once they started moving as well as the traveled distance δ. This concerns tracers that had stopped over the horns or that were previously buried and suddenly exposed by erosion. Therefore, we employ here the term *residence time of moving grains* to make it clear that we are not dealing with the characteristic time of residence of grains within the horns, but with the time that, once moving, they take to leave the horns. This is different from the concept of residence time computed by Zhang *et al.* (2014), who investigated numerically the residence time of grains in the entire barchan before their ejection at the tips of horns. Zhang *et al.* (2014) found that the residence time in the barchan is given by the surface of the longitudinal central slice of the dune divided by the input sand flux.

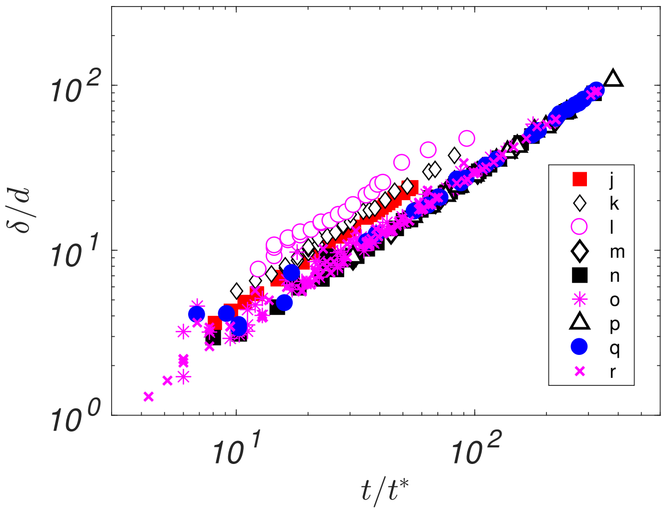

Fig. 4.12: Traveled distance normalized by the grain diameter, δ/d, as a function of the residence time of moving grains leaving the horns normalized by the settling time, t/t^*. A quasilinear relationship is verified for all tested cases. The cases listed in the key are presented in Table 4.1.

Figure 4.12 presents δ normalized by the grain diameter as a function of t normalized by a settling time t^* defined as

$$t^* = \left(\frac{\rho\, d}{(\rho_s - \rho) g} \right)^{1/2}, \tag{4.5}$$

on log-log scales, for all moving tracers that originate on the horns. Independently of the flow rate and grain size, δ/d varies quasilinearly with t/t^*, grains under higher Shields numbers remaining on the horns for shorter times (cases j, k, and l); these grains, dragged by a stronger fluid flow, travel longer distances in shorter times. An exponential fit of the data presented in Fig. 4.12 gives

$$\delta/d \sim (t/t^*)^{0.8702}, \tag{4.6}$$

with R^2 = 0.997, i.e., a quasilinear relation.

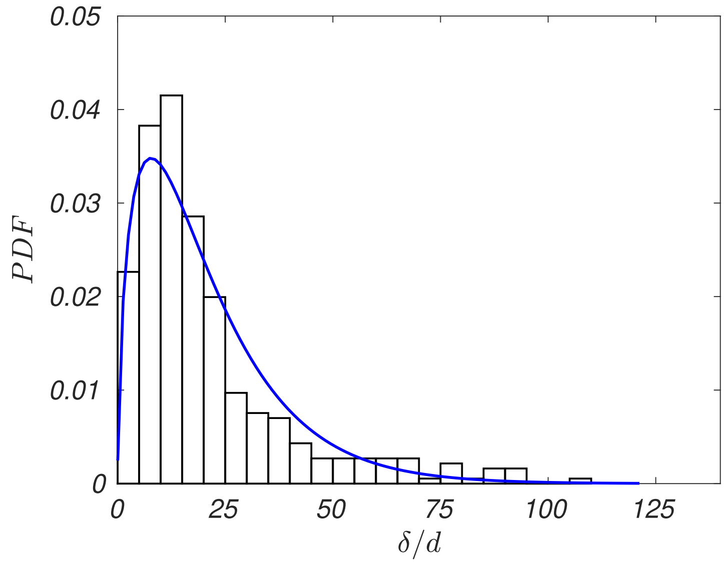

(a)

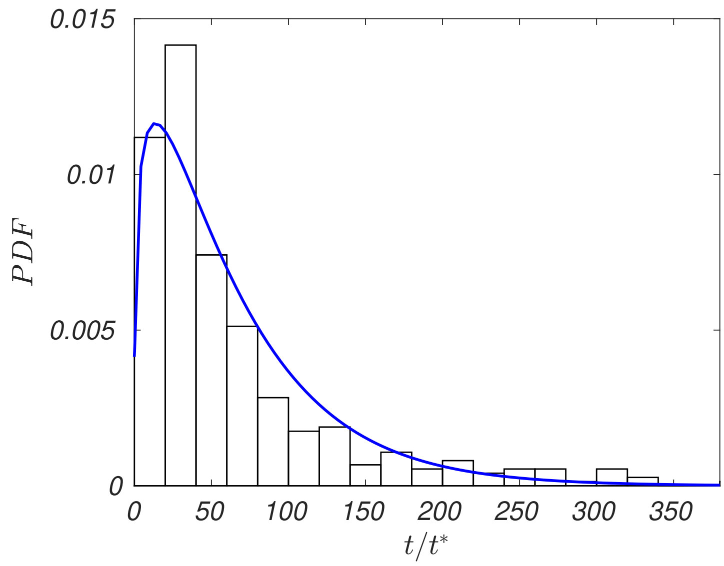

(b)

Fig. 4.13: PDFs of (a) the traveled distance normalized by the grain diameter, δ/d, and (b) the residence time of moving grains leaving the horns normalized by the settling time, t/t^*. Solid lines correspond to fittings using gamma functions. Cases j to r are included in these PDFs.

In **Chapter 3**, we found that for developed barchans the horn length is $L_h \approx 10L_{drag}$. Therefore, in the case of subaqueous barchans formed by glass beads $L_h \approx 25d$ and we expect that δ scales with this value. Figures 4.13(a) and 4.13(b) present the PDFs of the traveled distance normalized by the grain diameter, δ/d, and the residence time of moving grains normalized by the settling time, t/t^*, respectively, for cases j to r. The data presented in Figs. 4.13(a) and 4.13(b) were fitted by gamma functions, shown as solid lines in these figures. For these functions, the most probable value of δ is $15d$ (the mean value for the gamma fit being $20d$) and the most probable residence time is $35t^*$ (the mean value for the gamma fit being $65t^*$). The most probable value found for δ is of the expected order of magnitude. Concerning the most probable residence time, it corresponds to dimensional values of 0.13 s $\leq\ t\ \leq$ 0.20 s; therefore, the characteristic velocity of grains leaving the horns is 0.015 m/s $\leq\ \delta/t\ \leq$ 0.057 m/s, which corresponds to 6-16$\%$ of the cross-sectional mean velocity of the water. These values are in accordance with those of Lajeunesse *et al.* (2010), Roseberry *et al.* (2012), and Penteado & Franklin (2016), although these works concerned plane beds.

4.4 Chapter summary

In this chapter we have presented experimental results on the dynamics of grains migrating to horns of both evolving and developed subaqueous barchans. Our results showed that the majority of these grains do not come from the lateral flanks of the initial heap or dune, as usually asserted in the aeolian case. Instead, we show that in the subaqueous case most of the grains migrating to horns come from upstream regions of the bedform, exhibiting significant transverse displacements. For these grains, irrespective of their size and the strength of the water flow, we found that the distributions of transverse and streamwise velocities are given by exponential functions, with the probability density functions of their magnitudes being similar to results obtained from previous studies on flat beds. We have computed the residence time of moving grains, which we defined as the time taken by moving grains whose initial positions were on the horns of developed barchans to leave them, and the corresponding length. We found that the residence time and traveled distance are related following a quasi-linear relation, and that their most probable values are 35 times the settling time and 15 grain diameters, respectively. In addition, we have shown that the characteristic velocity of these grains is of the same order as velocities reported for subaqueous bed load on plane beds. Our results change the way in which the crescentic shape of subaqueous barchans is explained. However, the physical mechanisms underlying the shape of barchan dunes, which we have identified for the subaqueous case, cannot be precluded for bedforms found on terrestrial deserts and other planetary environments. Therefore, further numerical and experimental investigations on aeolian dunes are necessary to shed more light on the physical mechanisms leading to the formation of barchans in different environments.

5 SHAPE EVOLUTION OF NUMERICALLY OBTAINED SUBAQUEOUS BARCHAN DUNES†

In addition to the scales of bedforms, the transport of grains presents significant differences according to the nature of the entraining fluid, so that the growth of barchans is still not fully understood. Given the smaller length and time scales of the aquatic case, subaqueous barchans are the ideal object to study the growth of barchan dunes. In this chapter, we reproduce numerically the experiments presented in ***Chapters 3 and 4*** *on the shape evolution of barchans from their initiation until they have reached a stable shape. We computed the bed evolution by using the computational fluid dynamics - discrete element method, where we coupled the discrete element method with large eddy simulation (LES) for the same initial and boundary conditions of the experiments. Our simulations captured well the evolution of the initial pile toward a barchan dune in both the bedform and grain scales, with the same characteristic time and lengths observed in experiments. This shows that the present method is appropriate for numerical computations of bedforms, opening new possibilities for accessing data that are not available from current experiments.*

5.1 Introduction

Under the action of a fluid flow, granular beds may give rise to ripples and dunes. Among the different bedforms, barchan dunes are strong attractors that can be found in highly diverse environments such as rivers, oil pipelines, open channels, terrestrial deserts, and even other planetary environments (Bagnold, 1941; Hersen *et al.*, 2002; Claudin & Andreotti, 2006; Parteli & Herrmann, 2007). Barchans are usually formed when grains are transported as bed load by a one-directional fluid flow, and they are characterized by a crescentic shape with horns pointing downstream (Bagnold, 1941; Hersen *et al.*, 2002). Although robust, this shape presents different scales according to the environment the barchans are in, varying from the decimeter and minute under water (Franklin & Charru, 2009, 2011) to the kilometer and millennium on Mars (Claudin & Andreotti, 2006; Parteli & Herrmann, 2007).

† This chapter is based on C. A. Alvarez and E. M. Franklin, Phys. Rev. E 101, 012905 (2020). (Alvarez & Franklin, 2020)

Besides the bedform scales, the transport of grains is different according to the nature of the entraining fluid. In liquids, bed load is characterized by grains that move by rolling and sliding over each other (Penteado & Franklin, 2016), and occasionally by small jumps with distances of the order of a few grain diameters (Bagnold, 1956, 1973), while in gases bed load is characterized by ballistic flights over distances much larger than the grain diameter (Bagnold, 1941, 1956). Because of shape and transport differences, a general explanation for the growth of barchans is still lacking.

Given the smaller length and time scales of the aquatic case, subaqueous barchans are the ideal object to study the growth of barchan dunes. For this reason, many studies carried out experiments in water tanks and channels in order to obtain the length and time scales of barchans (Hersen *et al.*, 2002; Endo *et al.*, 2004; Franklin & Charru, 2011; Hori *et al.*, 2007; Alvarez & Franklin, 2017a) and typical trajectories and velocities of moving grains (Alvarez & Franklin, 2018b, 2019). The smaller and faster scales of the subaqueous case have allowed the establishment of relations and scaling factors crucial to understand the dynamics of much larger and slower barchans found in other environments (Hersen *et al.*, 2002; Claudin & Andreotti, 2006; Parteli & Herrmann, 2007).

Another way to investigate the dynamics of barchans is by carrying out numerical simulations. The first numerical works computing large-scale dunes employed continuum models for the grains (Sauermann *et al.*, 2001; Herrmann & Sauermann, 2000; Kroy *et al.*, 2002a,b, 2005; Schwämmle & Herrmann, 2005; Parteli *et al.*, 2014) and considered that saltation was the mode of entrainment, occurring mainly in the longitudinal direction, with some transverse diffusion. Therefore, those models are suitable to simulations of Aeolian and Martian dunes consisting of a large number of salting grains, in which, indeed, they succeeded. However, the transverse displacements of grains in the subaqueous case are, on average, comparable to the longitudinal ones, as shown recently by Alvarez & Franklin (2018b, 2019), a situation different from what is generally conjectured for the Aeolian and Martian cases. If we consider that subaqueous barchans measure a few decimeters, consisting of only some tens of thousands of grains, and that saltation is not the preferable mode of entrainment, then continuous models are not well justified in the aquatic case, although they may give reasonable results if the transverse diffusion is tuned appropriately or if bed load is considered to follow more closely the fluid. For example, Khosronejad & Sotiropoulos (2017) succeeded in computing fields of subaqueous barchans by using a continuum model for the grains. They coupled a large eddy simulation (LES) model for the water and water-suspension mixture with a continuum model involving the entrainment and Exner equations for the granular bed, obtaining morphological characteristics of bedforms during the evolution of an initially flat bed toward a barchan field. However, the dynamics at the grain scale is not accessible with this method.

More recently, simulations of bed load as a discrete medium by using Euler-Lagrange methods, such as the computational fluid dynamics - discrete element method (CFD-DEM), succeeded in capturing the main features of bed load (Schmeeckle, 2014; Kidanemariam & Uhlmann, 2014b; Liu *et al.*, 2016; Sun & Xiao, 2016; Pähtz & Durán, 2017) and bedforms (Kidanemariam & Uhlmann, 2014a, 2017). Schmeeckle (2014) presented a model coupling DEM with LES based on the open source codes CFDEM (Goniva *et al.*, 2012) (www.cfdem.com), OpenFOAM (www.openfoam.org), and LIGGGHTS (Kloss & Goniva, 2010; Berger *et al.*, 2015), that was used to compute sand transport by water. The author carried out computations for different flow strengths over initially flat beds, being interested essentially in the entrainment of grains by the water flow. His results showed that bed-load grains move generally in contact with the bed and that saltation is of lesser importance in the subaqueous case, with most of the grains being dislodged directly by the water flow. Pähtz & Durán (2017) investigated numerically the mechanisms of the entrainment of grains by using DEM coupled with Reynolds-averaged Navier-Stokes equations (RANS). The authors examined the conditions for entrainment directly by the fluid (fluid entrainment) and particle-bed impacts (impact entrainment), and they found that fluid entrainment is important only for viscous cases, the impact entrainment being more important in all the other cases. For a given range of flows, Schmeeckle (2014) and Pähtz & Durán (2017) present contrasting results with respect to grain entrainment.

Kidanemariam & Uhlmann (2014a,b, 2017) numerically investigated bed load and the growth of bedforms in the subaqueous case. The authors used direct numerical simulations (DNS) for the fluid, DEM for the grains, and immersed boundary (IB) for the coupling between fluid and grains. Their simulations showed that bed load is computed properly by the proposed method, and wavelengths, amplitudes, and celerities of bedforms are well captured, being in agreement with experimental data available in the literature. The proposed methodology is currently the most accurate, avoiding the use of turbulence models for the fluid, capturing all the scales of turbulence down to the Kolmogorov scale, and fully solving the flow around each grain. However, the computational cost is exceedingly high, so that the time required for obtaining developed bedforms is seldom reached (Colombini, 2014).

Although some numerical investigations succeeded in capturing the formation of subaqueous barchans, they did not report detailed measurements in the bedform and grain scales, namely the evolution of lengths and times of bedforms and the trajectories of individual grains over barchans. In addition, the role of water in the direct entrainment of grains is still a subject of debate. Detailed morphological evolution, local characteristics of the water flow, and trajectories of individual grains obtained from numerical computations are important to evaluate the suitability of numerical methods and provide information not accessible from reported experiments, such as the mode of entrainment and resultant forces on grains.

In this chapter, we reproduce numerically some of the experimental results presented in **Chapter 3 and 4** on the shape evolution of barchans, from their initiation until they have reached a stable shape, and the trajectories of grains migrating to horns. Besides the evolution of the bedform morphology and the trajectory of grains, we obtained numerically the local water flow over a single barchan, which we compare with the experiments of Charru & Franklin (2012). Our simulations were performed by using CFD-DEM to compute numerically the formation of single barchans from initially conical piles, where the fluid was computed with LES and the grains by solving linear and angular momentum equations applied to each particle. LES, although needing subgrid turbulence models, is able to compute the flow around bedforms including recirculation regions and some large turbulence structures, with a much lower computational cost than DNS. Our simulations captured not only the formation of barchans, but also their length scale, the time scale t_c for the growth of horns, and the trajectories of grains migrating to horns. Our results show that the used method is appropriate to numerical computations of subaqueous bedforms, opening new possibilities for accessing data not available from current experiments.

5.2 Model description

Our numerical investigation was conducted with CFD-DEM, where the dynamics of each individual particle was computed by DEM (Cundall & Strack, 1979) using the resulting forces and torques on each particle, the fluid flow was computed by LES, and momentum coupling was made between solids and fluid.

5.2.1 Grains

The solid particles are treated in a Lagrangian framework, with the dynamics of each particle being computed by the linear and angular momentum equations, given by Eqs. 5.1 and 5.2, respectively,

$$m_p \frac{d\vec{u}_p}{dt} = \vec{F}_{fp} + \vec{F}_c + m_p \vec{g} \tag{5.1}$$

$$I_p \frac{d\vec{\omega}_p}{dt} = \vec{T}_c \tag{5.2}$$

where $\vec{g}$ is the acceleration of gravity and, for each particle, m_p is the mass, $\vec{u}_p$ is the velocity, I_p is the moment of inertia, $\vec{\omega}_p$ is the angular velocity, $\vec{F}_{fp}$ is the resultant of fluid forces on grains, $\vec{F}_c$ is the resultant of contact forces between solids, and $\vec{T}_c$ is the resultant of contact torques between solids. In the balance of angular momentum, Eq. 5.2, we neglect momentum variations caused by the fluid because the term due to contacts is much higher (Tsuji *et al.*, 1992, 1993; Liu *et al.*, 2016). In the present study, we consider that the resultant of fluid forces acting on each particle is made up of components given by the fluid drag, fluid stresses and added mass:

$$\vec{F}_{fp} = \vec{F}_D + \vec{F}_{stress} + \vec{F}_{am} \tag{5.3}$$

where $\vec{F}_D$ is the drag force caused by the fluid on grains, $\vec{F}_{stress}$ = $V_p\left[-\nabla P + \nabla \cdot \vec{\vec{\tau}}\right]$ is the force caused by fluid stresses and $\vec{F}_{am}$ is the added mass force, V_p being the volume of one solid particle, P the fluid pressure and $\vec{\vec{\tau}}$ the deviatoric stress tensor of the fluid. In Eq. 5.3, we neglect the Basset, Saffman and Magnus forces as they are usually considered of lesser importance in CFD-DEM simulations (Zhou *et al.*, 2010).

The contact forces and torques are the result of contacts between particles and between particles and the wall. They can be expressed, respectively, by Eqs. 5.4 and 5.5,

$$\vec{F}_c = \sum_{i \neq j}^{N_c} \left(\vec{F}_{c,ij}\right) + \sum_{i}^{N_w} \left(\vec{F}_{c,iw}\right) \tag{5.4}$$

$$\vec{T}_c = \sum_{i \neq j}^{N_c} \vec{T}_{c,ij} + \sum_{i}^{N_w} \vec{T}_{c,iw} \tag{5.5}$$

where $\vec{F}_{c,ij}$ and $\vec{F}_{c,iw}$ are the contact forces between particles and between particles and the wall, respectively, $\vec{T}_{c,ij}$ is the torque due to the tangential component of the contact force between particles i and j, and $\vec{T}_{c,iw}$ is the torque due to the tangential component of the contact force between particle i and the wall, N_c - 1 being the number of particles in contact with particle i, and N_w the number of particles in contact with the wall.

5.2.2 Fluid

The fluid is the continuous phase and is treated in an Eulerian framework. For an incompressible flow, mass and momentum equations are given by Eqs. 5.6 and 5.7, respectively,

$$\nabla \cdot \vec{u}_f = 0 \tag{5.6}$$

$$\frac{\partial \rho_f \vec{u}_f}{\partial t} + \nabla \cdot (\rho_f \vec{u}_f \vec{u}_f) = -\nabla P + \nabla \cdot \vec{\vec{\tau}} + \rho_f \vec{g} - \vec{f}_{fp} \tag{5.7}$$

where $\vec{u}_f$ is the fluid velocity, ρ_f is the fluid density (equal to 10^3 kg/m^3 in the present case), and $\vec{f}_{fp}$ is the resultant of fluid forces acting on each grain, $\vec{F}_{fp}$, by unit of fluid volume, representing the momentum transfer from the fluid to the solids.

5.3 Numerical setup

In the present study, we used the open source code CFDEM (Goniva *et al.*, 2012) (www.cfdem.com) for our CFD-DEM computations. CFDEM links the open source code OpenFOAM, which computes the fluid flow based on the finite volume method (FVM), with the open source code LIGGGHTS (Kloss & Goniva, 2010; Berger *et al.*, 2015), which computes the dynamics of grains.

Concerning the grains, we considered a Hertzian model for which we set up the coefficient of restitution e as approximately 0.1 because collisions are expected to be viscous damped (Schmeeckle, 2014). The friction coefficient μ_{fr} was considered as 0.6 (Schmeeckle, 2014; Liu *et al.*, 2016), and Young's modulus E and the Poisson ratio σ were obtained from Tsuji *et al.* (1992, 1993). Young's modulus used in the simulations is considerably smaller than real values in order to reduce the DEM time step without affecting significantly the numerical outputs (Tsuji *et al.*, 1993). The main parameters used in our simulations are listed in Table 5.1.

Table 5.1: DEM parameters

Particle diameter d (mm)	0.5
Particle density ρ_p (kg/m^3)	2500
Young's Modulus E (MPa)	5
Poisson ratio σ	0.45
Restitution coefficient e	0.1
Friction coefficient μ_{fr}	0.6
Initial number of particles N	4×10^4
Time step (s)	5×10^{-6}

For the fluid, we used LES with subgrid stresses given by the wall-adapting local eddy-viscosity (WALE) model (Nicoud & Ducros, 1999). The domain was set to $0.3 \times 0.05 \times 0.16$ m divided into 150, 150 and 160 segments in the streamwise, x, wall-normal, y, and spanwise, z, directions, respectively. The dimensions in $y = 2\delta$ and z directions are the same as those of the previous experiments (**Chapter 3 and 4**). The segments in the x and z directions are uniform in size, whereas in the y direction they are unevenly spaced. Details of the grid and Reynolds numbers employed in our simulations are summarized in Table 5.2, where $Re = U2\delta\nu^{-1}$ is the channel Reynolds number based on the cross-sectional mean velocity and $Re_* = u_*\delta\nu^{-1}$ is the Reynolds number based on the shear velocity, ν being the kinematic viscosity (equal to 10^{-6} m^2/s in the present case).

Table 5.2: Computational grid and Reynolds numbers. Δx^+ and Δz^+ are the grid spacings Δx and Δz in the streamwise and spanwise directions, respectively, scaled in inner wall units, νu_*^{-1}. Δy_1^+ and Δy_c^+ are the grid spacing in the wall-normal direction at the first and center points, respectively, scaled in inner wall units. $Re = U2\delta\nu^{-1}$ and $Re_* = u_*\delta\nu^{-1}$, where U is the cross-sectional mean velocity.

	Case 1	Case 2
Δx^+	33.6	40.4
Δy_1^+	0.91	1.10
Δy_c^+	17.18	20.65
Δz^+	16.80	20.20
Re	1.47×10^4	1.82×10^4
Re_*	420	506

In Eq. 5.7, the term of momentum transfer between the fluid and solids is computed as $\vec{f}_{fp} = \vec{F}_{fp}/V_{cell}$, where V_{cell} is the volume of the considered computational cell. The drag force in Eq. 5.3 is computed as in Eq. 5.8,

$$\vec{F_D} = A_p C_D \rho_f (\vec{u_f} - \vec{u_p}) \left| \vec{u_f} - \vec{u_p} \right| \tag{5.8}$$

where A_p is the particle cross sectional area and C_D is a drag coefficient obtained from the Gidaspow model (Gidaspow, 1994).

Prior to CFD-DEM simulations, single phase flows were computed in the computational domain, corresponding to a rectangular cross-sectional channel. Periodic conditions were considered in streamwise and spanwise directions, and the final realization was saved to be used as

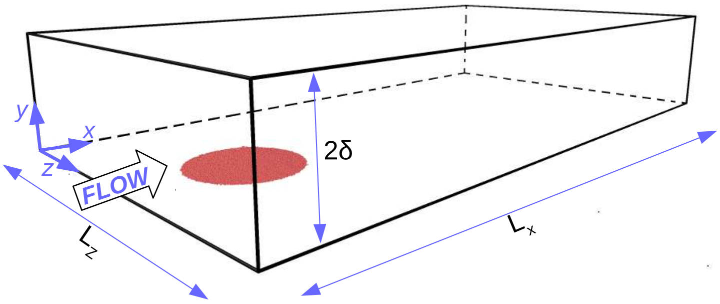

Fig. 5.1: Layout of the computational setup. In the simulations, L_x = 0.3 m, 2δ = 0.05 m and L_z = 0.16 m.

the fluid initial condition for the CFD-DEM simulations with grains.

Also prior to starting the simulations, the water flow was set to zero velocity and the grains were poured from above, falling freely in water at a longitudinal location 0.05 m from the domain inlet and centered in the transverse direction. After a period for the grains to settle, we obtained an initially conical pile with radius R = 0.025 m, similar to Alvarez & Franklin (2017a, 2018a,b), and the center at 0.05 m from the domain inlet. Once the initial condition for the grains was reached, we imposed the final realization of the single-phase LES computations as the initial condition for water. The boundary conditions for the fluid were impermeability and no-slip conditions at the top and bottom walls of the channel, and periodic conditions in the longitudinal and transverse directions. The boundary conditions for the solid particles were solid walls at the top and bottom walls, free exit at the outlet, and no mass entering at the inlet, so that the barchan decreased slightly in size while migrating, in the same manner as in Alvarez & Franklin (2017a, 2018b). Figure 5.1 shows a layout of the computational domain.

The resulting conditions for sediment transport are s = 2.5, Ga = 43, Im = 74, and θ = 0.04 and 0.06, where $s = \rho_p/\rho_f$ is the density ratio, $Ga = \sqrt{(s-1)\,gd^3}/\nu$ the Galileo number, $\theta = u_*^2/\left((s-1)\,gd\right)$ the Shields number, and $Im = Ga\sqrt{s+0.5}$ the impact number proposed by Pähtz & Durán (2017) to account for the importance of impact entrainment on bed load and saltation. In the present case $3 \leq \theta \times Im \leq 4$ and $Im > 20$, placing the bed-load conditions in the limit between fluid and impact entrainment, according to Pähtz & Durán (2017). The experiments reported by Alvarez & Franklin (2017a, 2018b) showed grains rolling and sliding following closely the mean water flow, pointing in the direction of direct entrainment by the fluid.

The tracking of bedforms and individual grains, as well as computations of morphology characteristics and grain trajectories, were carried out in the same manner as in our previous experiments (Alvarez & Franklin, 2017a, 2018b), making use of scripts written for this purpose based on Kelley & Ouellette (2011), Alvarez (2016), and Alvarez & Franklin (2017b).

5.4 Results and discussion

5.4.1 Single water flow

Computations of single-phase channel flows were necessary to be used as the initial condition for the simulations with solid particles. In order to evaluate our LES computations, the single phase simulations for Re_* = 420 were compared with the DNS results of Moser *et al.* (1999) for Re_* = 395. For that, we averaged 1,000 velocity fields in time (the last of 3,000 fields) and in the x and z directions, obtaining the profiles of mean velocity and Reynolds stress, which were compared afterward with Moser *et al.* (1999).

Figures 5.2(a) and 5.2(b) present, respectively, the profiles of the longitudinal component of the mean velocity in the traditional log-normal scales and of the components of the Reynolds stress, normalized by the inner scales, where solid lines correspond to the present LES results and dashed lines to the DNS results of Moser *et al.* (1999). In these figures, u is the longitudinal component of the mean velocity, u^+ = u/u_*, k is the turbulent kinetic energy, and u', v' and w' are the longitudinal, vertical and transverse components of velocity fluctuations, respectively. In the case of velocity fluctuations and turbulent kinetic energy, the superscript $+$ means division by u_*^2, overbar means temporal averages, and $<>$ refers to spatial averages in the x and z directions. Figure 5.2(a) presents also the law of the wall with κ = 0.41 and B = 5.2.

In Fig. 5.2(a) we can observe that in the viscous region the mean profile obtained with LES shows a good agreement with both the law of the wall and DNS results of Moser *et al.* (1999),

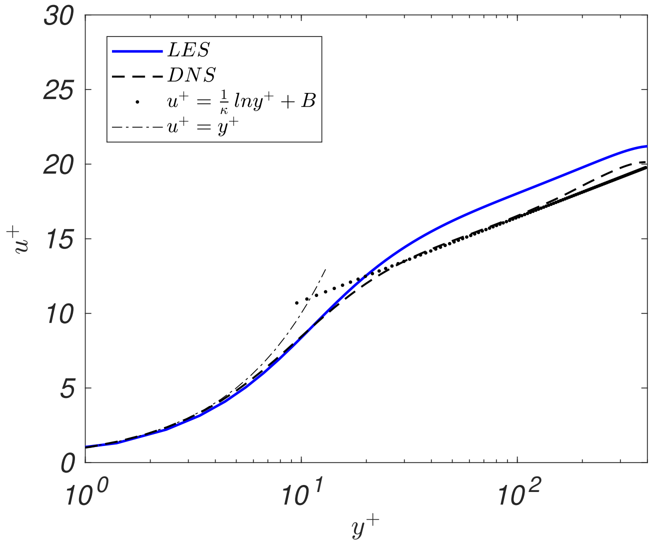

(a)

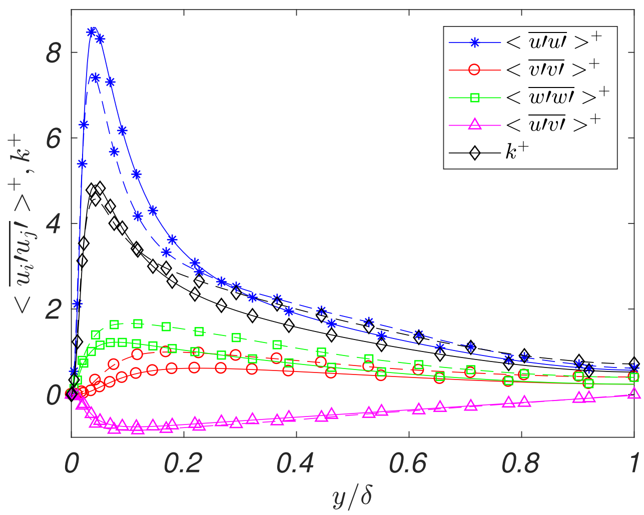

(b)

Fig. 5.2: Single-phase flow in the channel. a) Profile of the longitudinal component of the mean velocity u in the traditional log-normal scales, normalized by the inner scales. b) Profiles of the components of the Reynolds stress and turbulent kinetic energy normalized by the inner scales. Continuous lines correspond to the present LES results and dashed lines to the DNS results of Moser *et al.* (1999). Figure (a) presents also the law of the wall with κ = 0.41 and B = 5.2.

while in the overlap region LES results are shifted upwards with the same slope when compared with both the law of the wall and DNS. LES results could have a better agreement with DNS if we further refined the mesh; however, we are not carrying out particle-resolved simulations, so that the present results are adequate for the purpose of initial conditions for simulations with bed load. Figure 5.2(b) shows a good agreement between second-order moments obtained by LES and DNS. Finally, we observe that two-dimensional measurements with particle image velocimetry (PIV) in a channel with the same dimensions provided similar results (Franklin *et al.*, 2014; Cúñez *et al.*, 2018).

5.4.2 Simulations with bed load

Morphology of bedforms

With the grains settled in the channel, forming an initially conical pile, the output of the LES simulation for the single-phase flow was imposed as the initial condition for the fluid. Once the simulations started, with periodic conditions for the fluid in the x and z directions, the turbulent flow was sustained and the grains entrained by the water flow, deforming the initial pile in a barchan dune, as can be seen in Fig. 5.3.

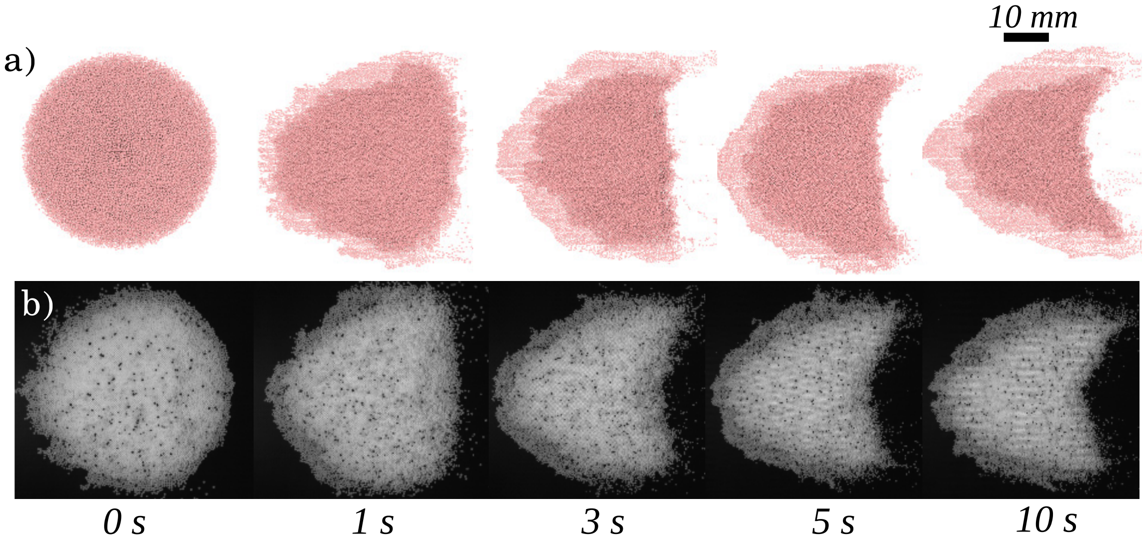

Fig. 5.3: Top views of an initially conical heap deformed by a turbulent water flow at different times. The flow is from left to right. a) Numerical results. b) Experiments of Alvarez & Franklin (2018b). Re = 1.82×10^4, d = 0.5 mm, and ρ_p = 2500 kg/m^3.

Figure 5.3 shows top views of the bedform as it is deformed from a conical heap in a barchan dune by the water flow. Figure 5.3(b) corresponds to images from experiments for Re = 1.82×10^4, d = 0.5 mm, and ρ_p = 2500 kg/m^3, and Fig. 5.3(a) consists of snapshots of our numerical simulations for the same conditions. We observe a similar evolution of bedforms in experiments and numerical simulations: once the water starts to flow, the pile is deformed, with the formation of a slip face and growing of horns. After some time, the bedform adopts a crescentic shape. The evolution of length and time scales is discussed next.

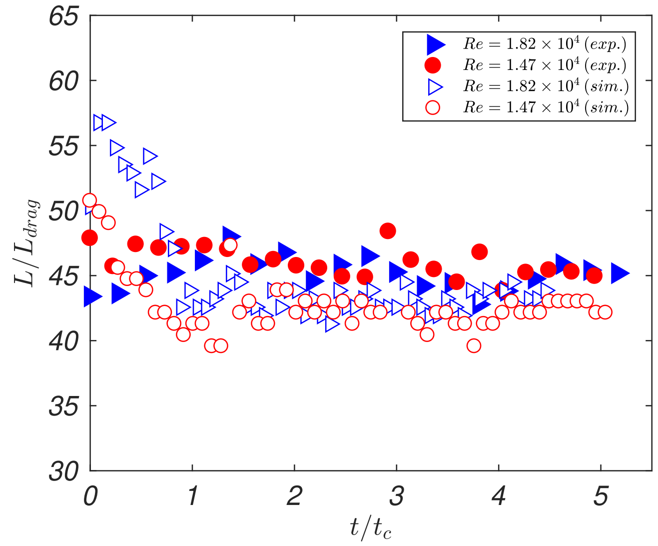

(a)

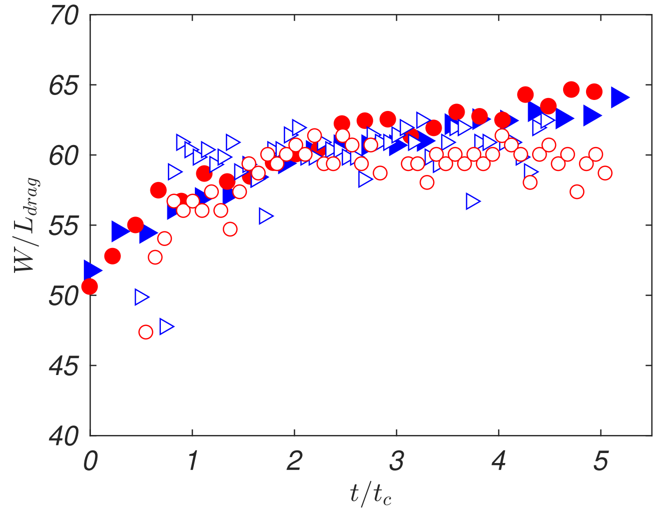

(b)

Fig. 5.4: (a) L/L_{drag} versus t/t_c and (b) W/L_{drag} versus t/t_c. The open symbols correspond to numerical results, solid symbols to the experimental results of Alvarez & Franklin (2017a, 2018b), and Reynolds numbers are listed in the key.

A direct comparison between experiments and numerical simulations for the evolutions of the length and width of barchans is presented in Fig. 5.4. Figures 5.4(a) and 5.4(b) show, respectively, the length L and width W of barchans normalized by the length scale L_{drag} as functions of time t normalized by the timescale t_c. The open symbols correspond to numerical results, solid symbols to the experimental results of Alvarez & Franklin (2017a, 2018b), and Reynolds numbers are listed in the key of Fig. 5.4(a). $L_{drag} = (\rho_s/\rho_f)d$ is an inertial length for the Aeolian case (Hersen *et al.*, 2002; Sauermann *et al.*, 2001), which is proportional to the length for the stabilization of sand flux, and $t_c = L_{eq}/C$ is the timescale for the barchan evolution (Alvarez & Franklin, 2017a), where L_{eq} is the barchan length once the crescentic shape is attained and C is the dune celerity.

For $t < t_c$, the numerically obtained values are different from the experimental ones, with, in addition, a different behavior for L, which decreases in the numerical results while it remains constant in the experiments. The difference in the initial behavior is due to slight differences in the initial conditions of numerical simulations when compared to experiments. In their turn, part of the differences in the initial conditions results from the pouring of grains on the bottom wall, where the friction coefficient between grains and wall is fixed in the numerical simulations, but is susceptible to variations and uncertainties in the experiments. In general, the bedforms in numerical simulations and experiments evolve in a similar manner, reaching roughly the same length and width for $t \geq t_c$, respectively.

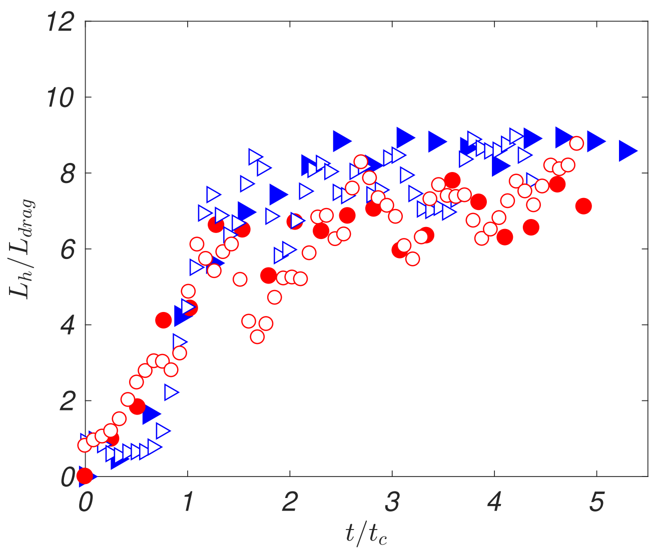

Fig. 5.5: L_h/L_{drag} versus t/t_c. The open symbols correspond to numerical results, solid symbols to the experimental results of Alvarez & Franklin (2017a, 2018b), and Reynolds numbers are listed in the key of Fig. 5.4(a).

The time evolution of the length of horns L_h is shown in Fig. 5.5, which presents L_h/L_{drag} as a function of t/t_c. The open symbols correspond to numerical results, solid symbols to the experimental results of Alvarez & Franklin (2017a, 2018b), and Reynolds numbers are listed in the key of Fig. 5.4(a). In the case of L_h, the numerical results show a good agreement with experiments, the length increasing with the same slope for $t < 2.5t_c$ and reaching the same constant value for $t \geq 2.5t_c$.

Arguing that the main feature of a barchan dune is its horns, we proposed in Alvarez & Franklin (2017a), based on the evolution of horns, that an initially conical pile deforms under the action of a water flow and reaches a stable crescentic shape when $t = 2.5t_c$. For $t \geq 2.5t_c$, the subaqueous barchan migrates keeping the same crescentic shape, being referred to in Alvarez & Franklin (2017a) as stable dunes. Because our numerical simulations predict the same evolution for horns at all times, and similar behaviors for the dune length and width for $t \geq t_c$, we consider that the present simulations capture well the morphology of evolving barchans.

Flow over single barchans

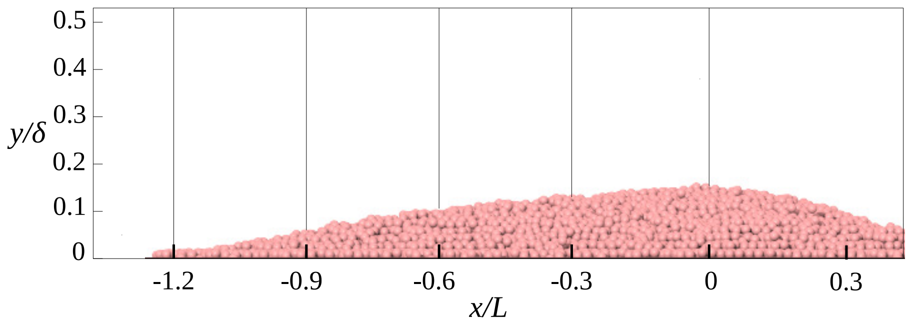

Fig. 5.6: Side view of a barchan dune, showing the adopted coordinate system for the flow over the dune. Vertical lines correspond to the longitudinal positions of the profiles plotted in Figs. 5.7 and 5.8.

Second-order moments for the flow over a barchan dune were obtained by time averaging 10,000 instantaneous fields (the last of 20,000 fields) in the vertical symmetry plane of the dune. Because the flow evolves along the dune, we present next only some profiles along the stoss side until reaching the dune crest. In order to obtain a significant number of fields while allowing a direct comparison with the PIV experiments reported in Charru & Franklin (2012), we artificially fixed the barchan dune by increasing considerably the density of grains at some point after $t = 2.5t_c$. This procedure is similar to that of Charru & Franklin (2012), where the fluid flow was reduced after $t = 2.5t_c$ in order to remain slightly below the threshold for bed load. Neglecting bed load in the subaqueous case is justified by its smaller effect on the water (feedback effect) when compared with the shape perturbation (Charru & Franklin, 2012; Franklin *et al.*, 2014). We adopted the same coordinate system as in Charru & Franklin (2012), with the origin of the longitudinal coordinate at the dune crest, as shown in Fig. 5.6, and the use of the displaced coordinate $y_d = y - h(x)$, where $h(x)$ is the local height of the barchan in its vertical symmetry plane.

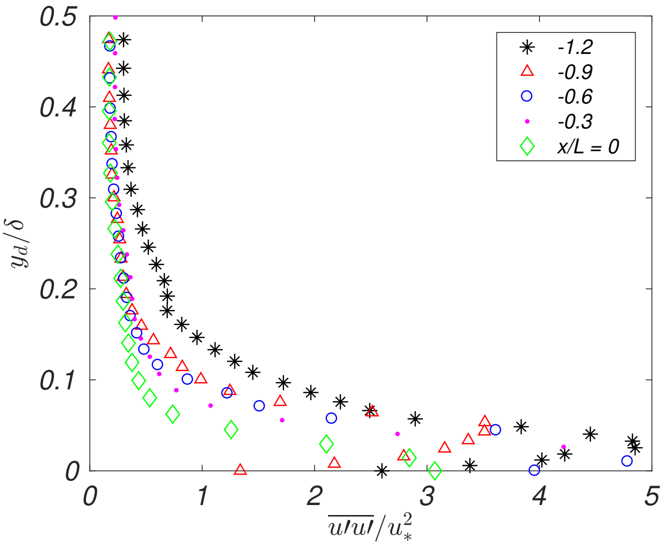

(a)

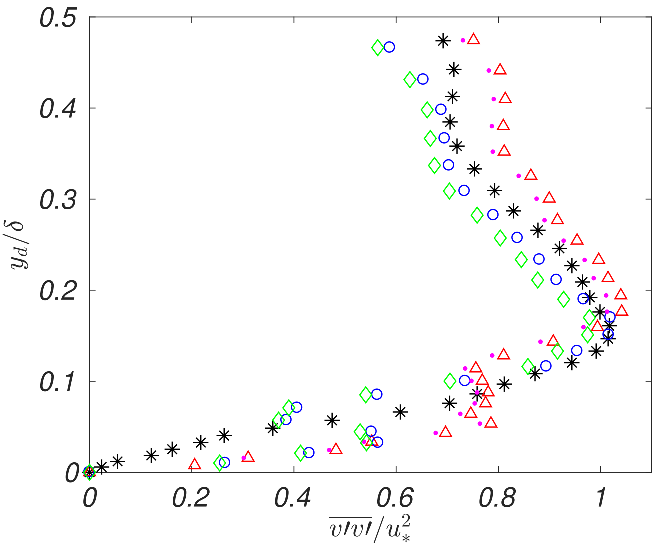

(b)

Fig. 5.7: Profiles of (a) $\overline{u'u'}$ and (b) $\overline{v'v'}$ normalized by u_*^2, using the displaced coordinate y_d normalized by δ. Each different symbol corresponds to a longitudinal position normalized by L, with origin at the dune crest, and listed in the key.

Figures 5.7 and 5.8 show the second-order moments for the flow over the barchan dune. Figures 5.7(a), 5.7(b) and 5.8 present some profiles of $\overline{u'u'}$, $\overline{v'v'}$ and $-\overline{u'v'}$, respectively, for

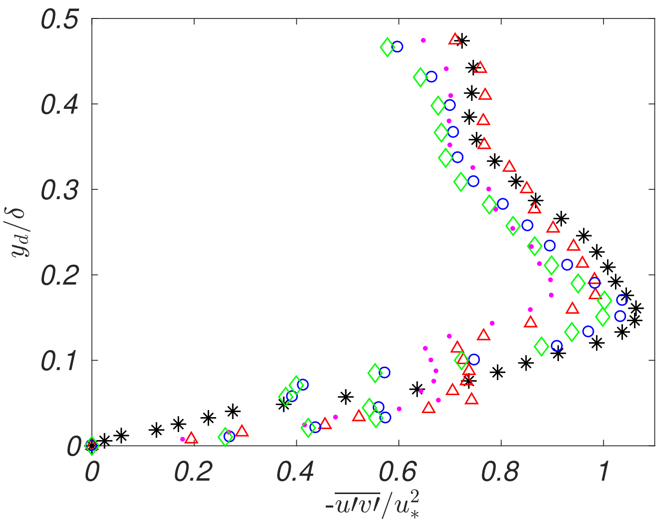

Fig. 5.8: Profiles of $-\overline{u'v'}$ normalized by u_*^2, using the displaced coordinate y_d normalized by δ. Each different symbol corresponds to a longitudinal position normalized by L, with origin at the dune crest, and listed in the key of Fig. 5.7(a).

different longitudinal positions. In these figures, the abscissa corresponds to $\overline{u'u'}$, $\overline{v'v'}$ or $-\overline{u'v'}$ normalized by u_*^2, the ordinate to the displaced coordinate y_d normalized by δ, and each different symbol to the longitudinal position normalized by L with the origin at the dune crest. The plotted positions are listed in the key of Fig. 5.7(a).

The profiles of Figs. 5.7 and 5.8 are very much like Figs. 16 and 17(b) of Charru & Franklin (2012). In particular, we note that the maximum value of $-\overline{u'v'}$ is attained within -1.2 $< x/L <$ -0.6, reaching values of approximately $1.1u_*^2$, just as measured experimentally. In summary, the evolution of second-order moments along the dune obtained from our LES simulations is in good agreement with the results of Charru & Franklin (2012), showing that the numerical setup adopted captures the mean features associated with the turbulent flow over the dune.

Trajectories of grains

In Alvarez & Franklin (2018b), we presented the trajectories of grains migrating to the horns of barchans during their growth from conical piles that consisted of 0.40 mm $\leq d \leq$ 0.60 mm glass beads. We present next the trajectories of grains that migrated to the growing horns of barchans obtained from numerical simulations. In the simulations, we tracked only grains moving over the dune (over a granular bed), because grains moving directly over the channel wall presented straighter trajectories when compared with experiments. This difference may be connected to the microstructure of the grain and wall surfaces, which are smoother in the numerical simulations, and, therefore, affect strongly grains rolling and sliding directly over the bottom wall. In our experiments, we expect that the channel wall was subject to small scratches caused by the grains in addition to other sources of microstructure uncertainties.

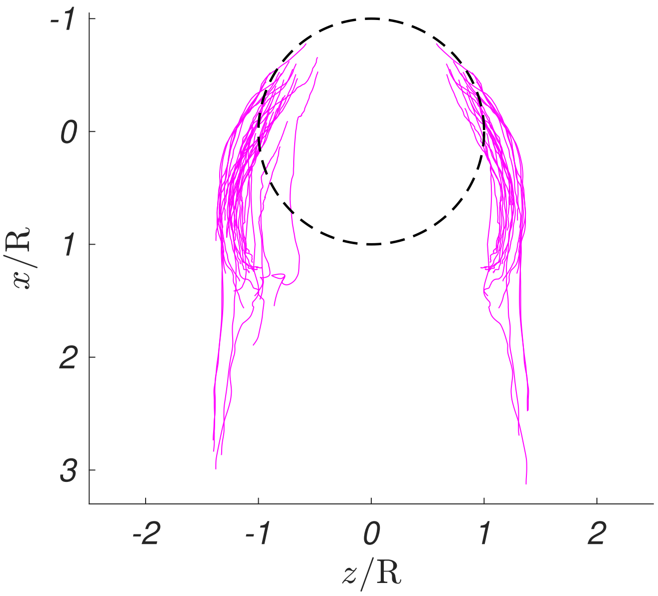

Fig. 5.9: Trajectories of some of the grains that migrated to horns during the growth of a barchan dune. The water flow is from top to bottom. Re = 1.82 $\times$ 10^4 and the black dashed circle represents the initial pile of radius R.

Figure 5.9 shows the pathlines of some grains that migrated to horns during the growth of a barchan dune from an initially conical pile for the numerical simulations with Re = 1.82 $\times$ 10^4. The abscissa and ordinate correspond, respectively, to the transverse and streamwise coordinates, z and x, normalized by R. In Fig. 5.9, the dashed black circle displays the initial pile. We observe a behavior similar to that noted in Alvarez & Franklin (2018b), with grains that migrate to horns describing circular paths, which implies significant transverse components. As verified experimentally by Alvarez & Franklin (2018b), these grains come from regions upstream of the dune centroid, moving around the central region of the barchan before reaching the horns.

In Alvarez & Franklin (2018b), we used radial and angular coordinates with the origin at the dune centroid in order to find the original positions of grains migrating to the growing horns, and afterward we computed their probability density functions (PDFs) and frequencies of occurrence. We make use here of the same method, in which we localize in polar coordinates the grains migrating to horns. The polar coordinates were defined as $(|r_1 - r_c|, \phi)$, in the same way as in Alvarez & Franklin (2018b), r_1 being the original position of grains, r_c the instantaneous position of the dune centroid, and ϕ the angle with respect to the transverse direction.

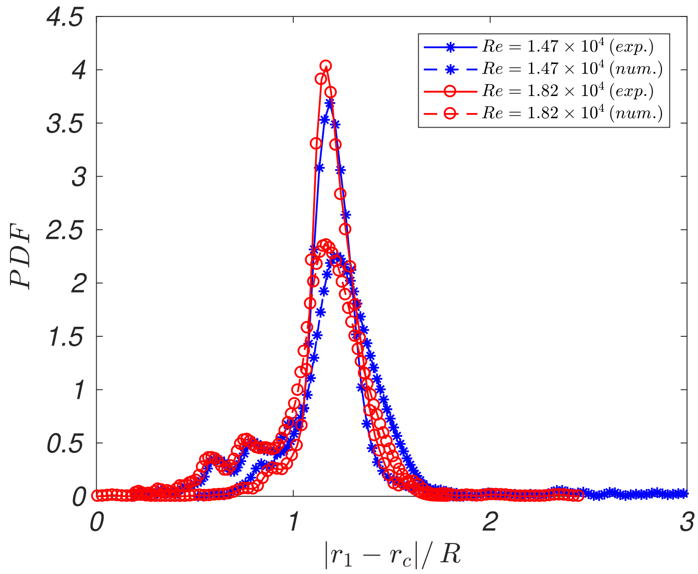

Fig. 5.10: PDFs of the original positions of the grains that migrated to horns during the growth of a barchan dune, obtained from numerical simulations and the experiments of Alvarez & Franklin (2018b). A kernel smoothing function was used in these plots (Bowman & Azzalini, 1997).

Figures 5.10 and 5.11 present the PDFs of the initial positions of grains migrating to horns as functions of $|r_1 - r_c|/R$ and their frequencies of occurrence as functions of ϕ, respectively, for both our numerical results and the experiments of Alvarez & Franklin (2018b). The PDFs of Fig. 5.10 were computed using a kernel smoothing function (Bowman & Azzalini, 1997) and the water flow direction in Fig. 5.11 is 270°. Figures 5.10 and 5.11 show a good agreement between experiments and numerical simulations, most of the grains that migrate to horns being originally within $|r_1 - r_c|/R > 1$ and $15° \leq \phi \leq 70°$ and $120° \leq \phi \leq 170°$, i.e., at upstream regions on the periphery of the pile.

We computed the total transverse (Δ_z) and longitudinal (Δ_x) distances traveled by the grains that migrated to horns. Figs. 5.12(a) and 5.12(b) present PDFs of Δ_z/L_{drag} and

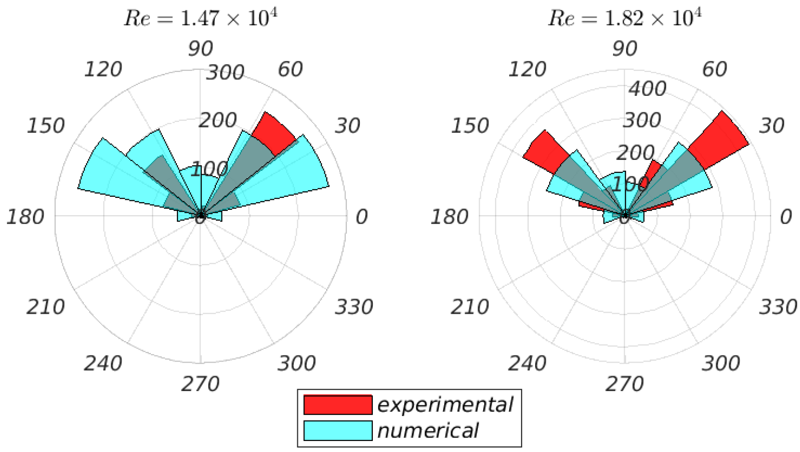

Fig. 5.11: Frequencies of occurrence of the initial positions of grains migrating to horns as functions of the angle with respect to the transverse direction (water flow direction is 270°), obtained from numerical simulations and the experiments of Alvarez & Franklin (2018b). The tips of appearing horns point to angles of approximately 240° and 300°.

Δ_x/L_{drag}, respectively, obtained from both the present simulations and the experiments of Alvarez & Franklin (2018b), and the cases are listed in the key of Fig. 5.12(a). For both the numerical simulations and experiments, we observe a significant transverse component in the movement of grains, corroborating the conclusion of Alvarez & Franklin (2018b) that in the subaqueous case grains migrating to horns describe circular paths with important transverse components. By considering the most probable values of the distributions, we find $11 \leq \Delta_z/L_{drag} \leq 13$ and $\Delta_z/\Delta_x \approx 0.5$ for the simulations, close to the values $10 \leq \Delta_z/L_{drag} \leq 12$ and $\Delta_z/\Delta_x \approx 0.5$ found for the experiments.

Granular flux

We present next the flux of grains along the subaqueous barchan, which still needs investigation even experimentally. For that, we computed the total number of grains crossing certain barchan cross sections (x planes) during specific periods. By using relatively short periods, we obtained *quasi-instantaneous* values for the flux.

Figure 5.13 presents the number of grains crossing certain barchan cross sections as a function of the normalized time t/t_c, where an interval of 0.13 s was used in the computations,

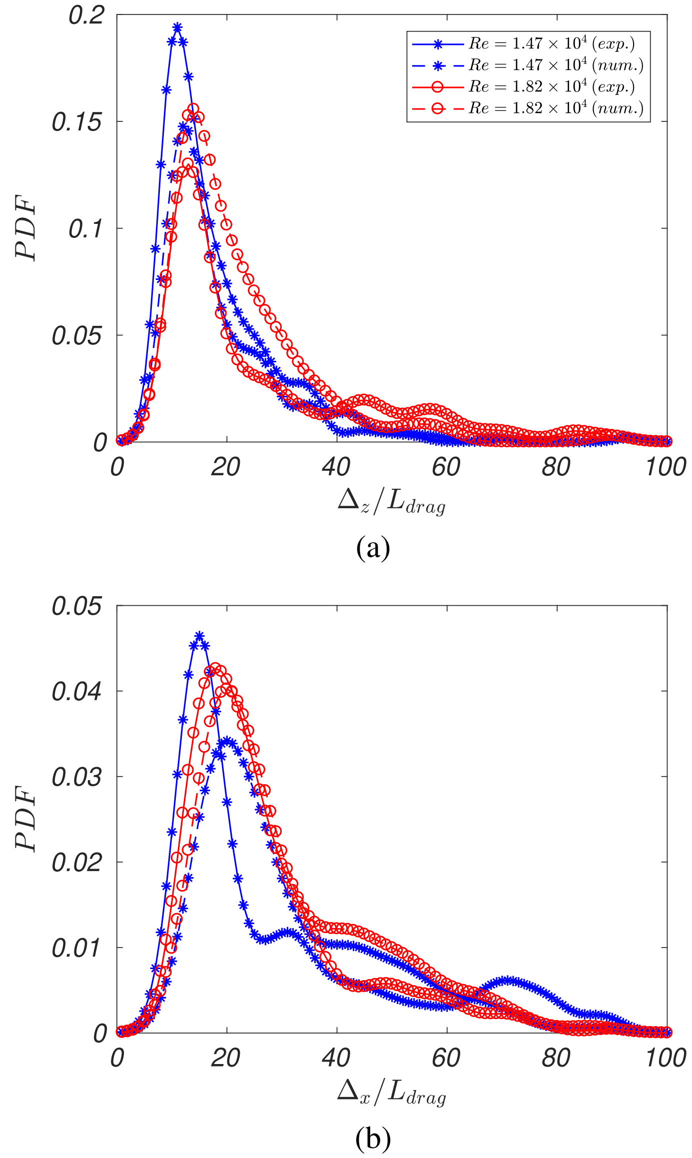

Fig. 5.12: PDFs of the total (a) transverse and (b) longitudinal distances, Δ_z and Δ_x, normalized by L_{drag} for numerical and experimental results, as listed in the key of figure (a).

corresponding to $0.016t_c$. Values presented in the ordinate can be converted to g by multiplying them by 1.64×10^{-4}, which corresponds to the grain mass in g. In spite of considerable dispersion, Fig. 5.13 shows that, locally, there seems to exist a transient in the flux of grains for $t/t_c \lesssim 1.5$ and afterward the flux is roughly constant. This is, in some measure, consistent with the characteristic time t/t_c = 2.5 for the growth of barchans proposed in the **Chapter 3**. In space, Fig. 5.13 shows that the flux is not saturated along the barchan, increasing toward the crest. Although it is known that the largest value should occur just upstream of the dune crest (Engelund & Fredsoe, 1982), we are not able to show that for the moment given the relatively high dispersion in obtained fluxes.

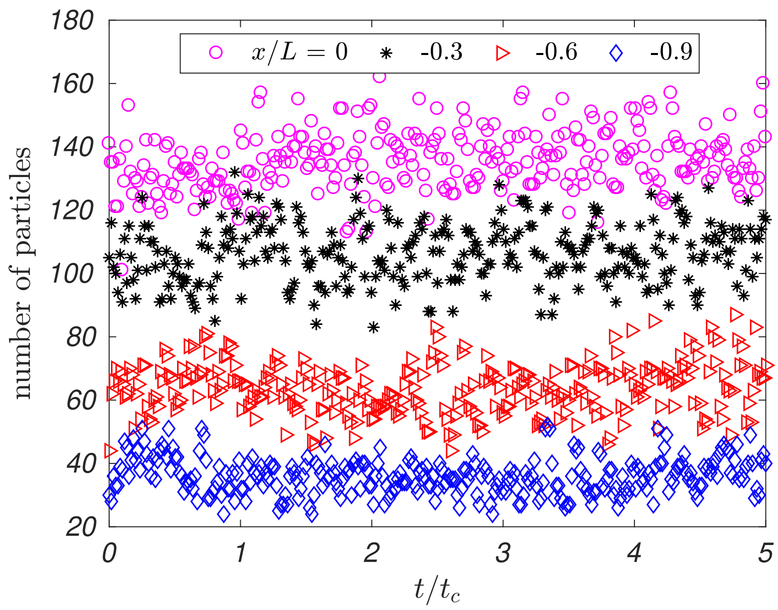

Fig. 5.13: Number of grains crossing certain barchan cross sections as a function of the normalized time t/t_c. The longitudinal positions of each considered cross section (x planes) are listed in the figure key (and shown in Fig. 5.6), and Re = 1.47×10^4. For these computations, a time interval of 0.13 s was used.

Forces on grains

The present simulations provide us with the resultant force acting on each grain, $\vec{F}_p$, corresponding to the right-hand side of Eq. 5.1, i.e., $\vec{F}_p = \vec{F}_{fp} + \vec{F}_c + m_p\vec{g}$. This information is difficult to access experimentally, and it is not available from current experiments. In this section we analyze the resultant force on grains along the barchan dune.

Figure 5.14 presents the resultant force on a tracked grain as it was entrained from an upstream region until the dune crest, and it is representative of the resultant force acting on grains migrating toward the crest. In Fig. 5.14, the solid blue line corresponds to the longitudinal component of the force, F_{px}, and the dashed red line to the transverse component of the force, F_{pz}. We observe that the grain experiences a varying force, in the transverse direction the instantaneous values varying around a zero average, while in the longitudinal direction the force has a positive average, with high peaks occurring in some occasions. These peaks are much higher than the mean value (in Fig. 5.14, the highest peak is one order of magnitude greater than the mean value). It is interesting to note that this specific grain took a time slightly longer than $1.5t_c$

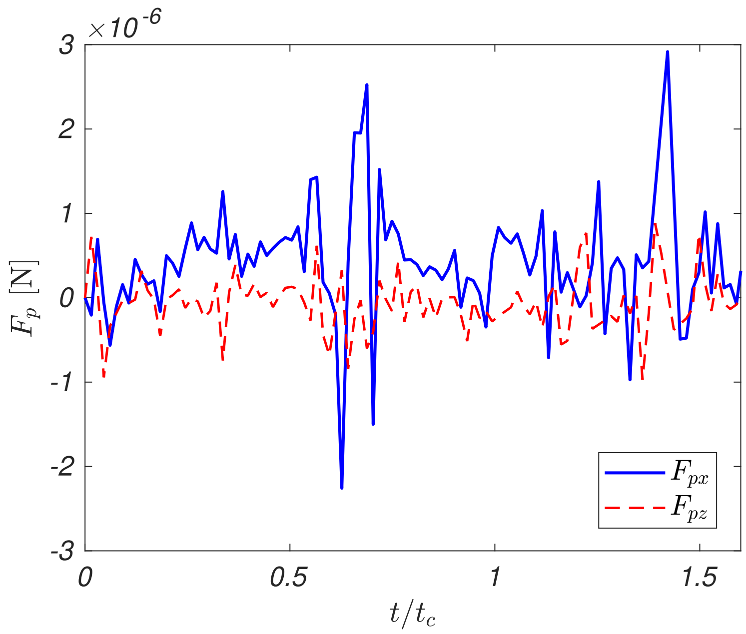

Fig. 5.14: Longitudinal and transverse components of the resultant force on a grain, F_{px} and F_{pz}, respectively, as a function of time. This specific grain was entrained from an upstream region toward the crest, and Re = 1.47×10^4.

to reach the dune crest, with the highest peak occurring just before reaching the crest.

Figures 5.15(a) and 5.15(b) present, respectively, PDFs of the longitudinal and transverse components of the resultant force acting on each grain crossing a given barchan cross section. Figure 5.15 shows that the resultant force acting on each grain has a longitudinal component that attains higher values on upstream regions and decays toward the crest, with a slightly broader distribution upstream, while the transverse component is always peaked at zero, also with a broader distribution upstream. Although the longitudinal component of the resultant force is lower at the crest, the granular flux increases toward the crest, as previously shown, due probably to the grain inertia. We expect that at the crest the granular flux is lower than that just upstream of it, but, as previously explained, the relatively high dispersion in computed fluxes does not allow us to prove that for the moment. The results on the resultant force, which have until now been only conjectured, help to explain the mechanism of upstream erosion and crest deposition that exists on barchan dunes.

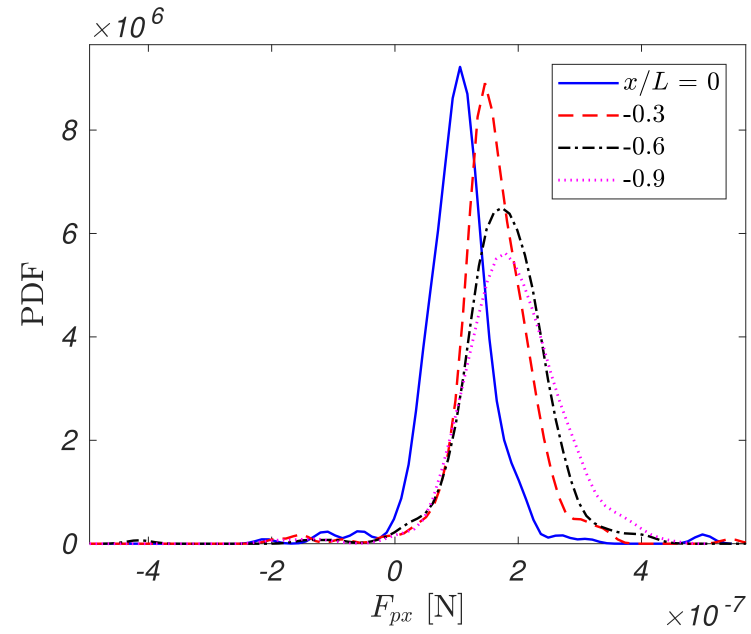

(a)

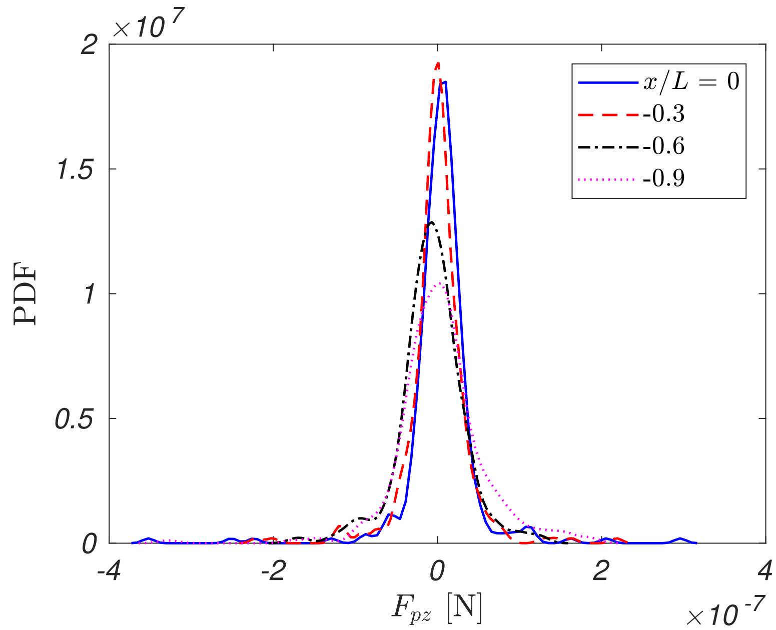

(b)

Fig. 5.15: PDFs of (a) the longitudinal and (b) transverse components of the resultant force acting on each grain crossing a given barchan cross section. The longitudinal positions of each considered cross section (x planes) are listed in the figure key and Re = 1.47×10^4.

5.5 Chapter summary

This chapter investigated numerically the formation and evolution of single barchans by using the computational fluid dynamics - discrete element method (CFD-DEM), where the DEM was coupled with the large eddy simulation (LES). The simulations reproduced numerically our experiments presented in Alvarez & Franklin (2017a, 2018b) and performed in a closed-conduit channel where initially conical heaps evolved to single barchans under the action of a turbulent water flow. The numerical setup used the same initial and boundary conditions of our experiments.

Our simulations captured well the evolution of the initial pile toward a barchan dune in both the bedform and grain scales. Concerning the bedform, the morphology obtained from our numerical simulations showed the same characteristic time and length observed in experiments: the horns grow and the dune width and length evolve until $t = 2.5t_c$, where t_c is a timescale proposed in Alvarez & Franklin (2017a), reaching a stable value for $t > 2.5t_c$. The evolution of the horn length, its final value, and that of the dune width and length are in excellent agreement with our experiments.

The water flow over a fixed barchan was compared with similar experiments reported in Charru & Franklin (2012). The evolution of second-order moments along the dune obtained from our LES simulations is in good agreement with the results of Charru & Franklin (2012), showing that the numerical setup adopted is able to capture the mean features associated with the turbulent flow over the dune.

We tracked the grains that migrated to the growing horns of barchans. We observed a behavior similar to that observed in Alvarez & Franklin (2018b), with grains that migrate to horns describing circular paths. Plots in polar coordinates centered at the dune centroid showed that these grains come from upstream regions on the periphery of the initial pile. In addition, computations of the total transverse and longitudinal distances traveled by the grains showed PDFs similar to experimental values and a ratio between the transverse and longitudinal distances of approximately 0.5, the same value obtained experimentally.

Finally, we obtained the local granular flux and the resultant force acting on each grain, the latter not yet previously measured nor computed. Concerning the granular flux, we showed that there exists a transient for $t/t_c \lesssim 1.5$ and that it is not saturated along the barchan. For the resultant force on each grain, we showed that its longitudinal component attains higher values on upstream regions and decays toward the crest. These results help to explain the mechanism of upstream erosion and crest deposition that exists on barchan dunes.

The good agreement between the numerical and experimental results shows that the present method is appropriate for numerical computations of bedforms, opening new possibilities for accessing data not available from current experiments, such as, for example, the instantaneous forces on each grain within the bed.

6 CONCLUSIONS

This work has shown that the formation of subaqueous barchan dunes from initially conical heaps in a rectangular channel can be associated with the appearance of their horns. Although the formation of barchan dunes has been studied for a long time, only a few works have carried out investigations on the behavior of their horns. In a novelty manner, we have associated the time scale for the horn growth with the formation of the whole barchan dune. Moreover, we have demonstrated that after a certain time, horns appear and grow, until an equilibrium length is reached. Our results showed the existence of a time scale for the appearance and equilibrium of horns. This time scale is given by a characteristic time t_c that scales with the grains diameter, gravity acceleration, densities of the fluid and grains, and shear and threshold velocities. Although we proposed t_c for the subaqueous case, our findings can be extrapolated to the formation of barchan dunes under more complex scenarios. We consider that our results are consistent and robust because in our experiments the more relevant variables involved in the grain transport were considered, i.e., different flow rates interacted with particles which diameters extended over a broad range, with both angular and round surfaces, two densities and that formed piles with different weights.

To the best of our understanding, we have presented an experimental investigation of the horn formation at the grain scale for the first time. Using a method of tracking at the grain scale, we have found that many of the grains accumulating in the front of an evolving or developed barchan travel around of it directly to its extremities to originate or fed up the horns. Our results clearly showed that the advance of the lateral dune flanks due to the scaling of migration velocity with the inverse of dune size is not the primary process leading to the barchan horns formation, as explained in previous conceptual models. Instead, the grains going to horns come from upstream regions traveling with significant transverse components. Furthermore, we calculated that for these grains, irrespective of their size and the strength of the water flow, the distributions of transverse and streamwise components of velocities are well described by exponential functions, with the probability density functions of their magnitudes being similar to results obtained from previous studies on flat beds. At least for the conditions tested in this work, our results change the way in which the growth of subaqueous barchan dunes is explained.

We have computed the bed evolution by using a coupling of computational fluid dynamics (CFD) and the discrete element method (DEM), employing an open-source code called CFDEM, which is extensively employed in systems involving particle-fluid interactions. The numerical setup was designed to reproduce the experimental conditions: geometrical features of the channel and statistically steady fully developed flow at its entrance, and the spherical particles had identical diameter and density as grains used in the experiments. Our numerical simulations have shown that the characteristics of a barchan dune, from its length, width, and horn length to its dynamic at the grain scale, are in good agreement with the experimental data both quantitatively and qualitatively.

For the single-phase channel flows, our LES reproduced with reasonable accuracy the velocity profile and the Reynolds stresses obtained by Moser *et al.* (1999); however, the author employed direct numerical simulation. Furthermore, our work is the first to simulate the evolution of a barchan dune and extract results about the dynamic of the grains traveling to growing horns. Detailed morphological evolution, local characteristics of the water flow and trajectories of individual grains obtained from numerical computations are essential to evaluate the suitability of numerical methods and provide information not accessible from reported experiments, such as, for example, the instantaneous forces on each grain within the bed.

The investigation carried out through this work is undoubtedly important for a broad range of physics and engineering communities. While it is difficult to claim that it is "opening a new field of research", it is certainly opening new directions/possibilities in the research of turbulent flows, granular matter, aeolian processes, pattern formation, etc.

Future works can be oriented to:

- Evaluate the formation of barchans under more complex scenarios, such as sand bars, large sand fields, and sand fields over complex topographies, for example.
- Perform experiments on the formation of granular patterns using a non-newtonian fluid in order to compare with the aquatic and aeolian cases.
- Investigate grain segregation, using tracking at the particle scale, in subaqueous dunes

formed by grains of different sizes.

- Carry out numerical simulations of the evolution of barchans employing the same computational setup presented in this work, but allowing interact grains coming from more than one pile.

References

AL-LABABIDI, S.; YAN, W. & YEUNG, H. Sand transportations and deposition characteristics in multiphase flows in pipelines. **Journal of Energy Resources Technology**, v. 134, n. 3, 034501, 2012.

AL-LABABIDI, S.; YAN, W.; YEUNG, H.; SUGARMAN, P. & FAIRHURST, C. Sand transport characteristics in water and two-phase air/water flows in pipelines. In **Proceedings of the Sixth North American Conference on Multiphase Technology**, pp. 159–174. 2008.

ALI, S.Z. & DEY, S. Impact of phenomenological theory of turbulence on pragmatic approach to fluvial hydraulics. **Physics of Fluids**, v. 30, n. 4, 045105, 2018.

ALVAREZ, C.A. Instabilidades de escoamentos gravitacionais de material granular em um tubo vertical. **MSc. Thesis, University of Campinas, Brazil**, 2016.

ALVAREZ, C.A. & FRANKLIN, E.M. Birth of a subaqueous barchan dune. **Physical Review E**, v. 96, n. 6, 062906, 2017a.

ALVAREZ, C.A. & FRANKLIN, E.M. Intermittent gravity-driven flow of grains through narrow pipes. **Physica A: Statistical Mechanics and its Applications**, v. 465, 725 – 741, 2017b.

ALVAREZ, C.A. & FRANKLIN, E.M. Experimental study on the formation of subaqueous barchan dunes in closed conduits. In **Experimental Fluid Mechanics 2017. EPJ Web of Conferences**, v. 180, p. 02002. 2018a.

ALVAREZ, C.A. & FRANKLIN, E.M. Role of transverse displacements in the formation of subaqueous barchan dunes. **Physical Review Letters**, v. 121, n. 16, 164503, 2018b.

ALVAREZ, C.A. & FRANKLIN, E.M. Horns of subaqueous barchan dunes: A study at the grain scale. **Physical Review E**, v. 100, n. 4, 042904, 2019.

ALVAREZ, C.A. & FRANKLIN, E.M. Shape evolution of numerically obtained subaqueous barchans. **Physical Review E**, v. 101, n. 1, 012905, 2020.

ANDREOTTI, B.; CLAUDIN, P. & DOUADY, S. Selection of dune shapes and velocities Part 1: Dynamics of sand, wind and barchans. **The European Physical Journal B-Condensed Matter and Complex Systems**, v. 28, n. 3, 321–339, 2002a.

ANDREOTTI, B.; CLAUDIN, P. & DOUADY, S. Selection of dune shapes and velocities Part 2: A two-dimensional modelling. **The European Physical Journal B-Condensed Matter and Complex Systems**, v. 28, n. 3, 341–352, 2002b.

ANDREOTTI, B.; CLAUDIN, P. & POULIQUEN, O. Aeolian sand ripples: experimental study of fully developed states. **Physical Review Letters**, v. 96, n. 2, 028001, 2006.

ANDREOTTI, B.; CLAUDIN, P. & POULIQUEN, O. Measurements of the aeolian sand transport saturation length. **Geomorphology**, v. 123, n. 3-4, 343–348, 2010.

ANDREOTTI, B.; FORTERRE, Y. & POULIQUEN, O. **Granular Media: Between Fluid and Solid**. Cambridge University Press, Cambridge, 2013.

BAGNOLD, R.A. **The Physics of Blown Sand and Desert Dunes**. Chapman and Hall, London, 1941.

BAGNOLD, R.A. The flow of cohesionless grains in fluids. **Philosophical Transactions of the Royal Society of London. Series A, Mathematical and Physical Sciences**, v. 249, n. 964, 235–297, 1956.

BAGNOLD, R.A. The nature of saltation and of 'bed-load'transport in water. **Proceedings**

of the Royal Society of London. A. Mathematical and Physical Sciences, v. 332, n. 1591, 473–504, 1973.

BERGER, R.; KLOSS, C.; KOHLMEYER, A. & PIRKER, S. Hybrid parallelization of the LIGGGHTS open-source DEM code. **Powder Technology**, v. 278, 234–247, 2015.

BOWMAN, A.W. & AZZALINI, A. **Applied Smoothing Techniques for Data Analysis: The Kernel Approach with S-Plus Illustrations**, v. 18. Oxford University Press, Oxford, 1997.

CHARRU, F. Selection of the ripple length on a granular bed sheared by a liquid flow. **Physics of Fluids**, v. 18, n. 12, 121508, 2006.

CHARRU, F.; ANDREOTTI, B. & CLAUDIN, P. Sand ripples and dunes. **Annual Review of Fluid Mechanics**, v. 45, 469–493, 2013.

CHARRU, F. & FRANKLIN, E.M. Subaqueous barchan dunes in turbulent shear flow. Part 2: Fluid flow. **Journal of Fluid Mechanics**, v. 694, 131–154, 2012.

CHARRU, F. & HINCH, E. Ripple formation on a particle bed sheared by a viscous liquid. part 1. steady flow. **Journal of Fluid Mechanics**, v. 550, 111–121, 2006.

CLAUDIN, P. & ANDREOTTI, B. A scaling law for aeolian dunes on Mars, Venus, Earth, and for subaqueous ripples. **Earth and Planetary Science Letters**, v. 252, n. 1-2, 30–44, 2006.

COLOMBINI, M. A decade's investigation of the stability of erodible stream beds. **Journal of Fluid Mechanics**, v. 756, 1–4, 2014.

CUNDALL, P.A. & STRACK, O.D. A discrete numerical model for granular assemblies. **Géotechnique**, v. 29, n. 1, 47–65, 1979.

CÚÑEZ, F.D.; DE OLIVEIRA, G.V.G. & FRANKLIN, E.M. Turbulent channel flow perturbed by triangular ripples. **Journal of the Brazilian Society of Mechanical Sciences and Engineering**, v. 40, n. 3, 138, 2018.

DEY, S. & ALI, S.Z. Advances in modeling of bed particle entrainment sheared by turbulent flow. **Physics of Fluids**, v. 30, n. 6, 061301, 2018.

ELBELRHITI, H.; CLAUDIN, P. & ANDREOTTI, B. Field evidence for surface-wave-induced instability of sand dunes. **Nature**, v. 437, n. 7059, 720, 2005.

ENDO, N.; KUBO, H. & SUNAMURA, T. Barchan-shaped ripple marks in a wave flume. **Earth Surface Processes and Landforms: The Journal of the British Geomorphological Research Group**, v. 29, n. 1, 31–42, 2004.

ENGELUND, F. Instability of erodible beds. **Journal of Fluid Mechanics**, v. 42, n. 2, 225–244, 1970.

ENGELUND, F. & FREDSOE, J. Sediment ripples and dunes. **Annual Review of Fluid Mechanics**, v. 14, n. 1, 13–37, 1982.

FRANKLIN, E.M. & CHARRU, F. Morphology and displacement of dunes in a closed-conduit flow. **Powder Technology**, v. 190, n. 1-2, 247–251, 2009.

FRANKLIN, E.M. & CHARRU, F. Subaqueous barchan dunes in turbulent shear flow. Part 1. Dune motion. **Journal of Fluid Mechanics**, v. 675, 199–222, 2011.

FRANKLIN, E.M.; DE FIGUEIREDO, F.T. & ROSA, E.S. The feedback effect caused by bed load on a turbulent liquid flow. **Journal of the Brazilian Society of Mechanical Sciences and Engineering**, v. 36, n. 4, 725–736, 2014.

GADAL, C.; NARTEAU, C.; DU PONT, S.C.; ROZIER, O. & CLAUDIN, P. Incipient bedforms in a bidirectional wind regime. **Journal of Fluid Mechanics**, v. 862, 490–516, 2019.

GERMANO, M.; PIOMELLI, U.; MOIN, P. & CABOT, W.H. A dynamic subgrid-scale eddy viscosity model. **Physics of Fluids A: Fluid Dynamics**, v. 3, n. 7, 1760–1765, 1991.

GIDASPOW, D. **Multiphase Flow and Fluidization: Continuum and Kinetic Theory Descriptions**. Academic press, 1994.

GONIVA, C.; KLOSS, C.; DEEN, N.G.; KUIPERS, J.A.M. & PIRKER, S. Influence of rolling friction on single spout fluidized bed simulation. **Particuology**, v. 10, n. 5, 582–591, 2012.

GROH, C.; REHBERG, I. & KRUELLE, C.A. How attractive is a barchan dune? **New Journal of Physics**, v. 11, n. 2, 023014, 2009.

GROH, C.; WIERSCHEM, A.; AKSEL, N.; REHBERG, I. & KRUELLE, C.A. Barchan dunes in two dimensions: Experimental tests for minimal models. **Physical Review E**, v. 78, n. 2, 021304, 2008.

GUIGNIER, L.; NIIYA, H.; NISHIMORI, H.; LAGUE, D. & VALANCE, A. Sand dunes as migrating strings. **Physical Review E**, v. 87, n. 5, 052206, 2013.

HERRMANN, H.J. & SAUERMANN, G. The shape of dunes. **Physica A: Statistical Mechanics and its Applications**, v. 283, n. 1-2, 24–30, 2000.

HERSEN, P. On the crescentic shape of barchan dunes. **The European Physical Journal B-Condensed Matter and Complex Systems**, v. 37, n. 4, 507–514, 2004.

HERSEN, P.; ANDERSEN, K.H.; ELBELRHITI, H.; ANDREOTTI, B.; CLAUDIN, P. & DOUADY, S. Corridors of barchan dunes: Stability and size selection. **Physical Review E**, v. 69, n. 1, 011304, 2004.

HERSEN, P.; DOUADY, S. & ANDREOTTI, B. Relevant length scale of barchan dunes. **Physical Review Letters**, v. 89, n. 26, 264301, 2002.

HEYMAN, J.; BOHÓRQUEZ, P. & ANCEY, C. Exploring the physics of sediment transport in nonuniform super-critical flows using a large dataset of particle trajectories. **Journal of Geophysical Research: Earth Surface**, v. 120, n. -, 2529–2551, 2015.

HINRICHSEN, H. & WOLF, D.E. **The Physics of Granular Media**. John Wiley & Sons, Germany, 2006.

HORI, N.; YAMADA, A.; OSHIRO, Y. & SANO, O. Formation of barchans and ripples due to steady viscous flow in an annular channel. **Journal of the Physical Society of Japan**, v. 76, n. 2, 024401, 2007.

KELLEY, D.H. & OUELLETTE, N.T. Using particle tracking to measure flow instabilities in an undergraduate laboratory experiment. **American Journal of Physics**, v. 79, n. 3, 267–273, 2011.

KHOSRONEJAD, A. & SOTIROPOULOS, F. On the genesis and evolution of barchan dunes: morphodynamics. **Journal of Fluid Mechanics**, v. 815, 117–148, 2017.

KIDANEMARIAM, A.G. & UHLMANN, M. Direct numerical simulation of pattern formation in subaqueous sediment. **Journal of Fluid Mechanics**, v. 750, 2014a.

KIDANEMARIAM, A.G. & UHLMANN, M. Interface-resolved direct numerical simulation of the erosion of a sediment bed sheared by laminar channel flow. **International Journal of Multiphase Flow**, v. 67, 174–188, 2014b.

KIDANEMARIAM, A.G. & UHLMANN, M. Formation of sediment patterns in channel flow: minimal unstable systems and their temporal evolution. **Journal of Fluid Mechanics**, v. 818, 716–743, 2017.

KLOSS, C. & GONIVA, C. LIGGGHTS: A new open source discrete element simulation software. In **Proceedings of 5th International Conference on Discrete Element Methods**.

London, UK, 2010.

KROY, K.; FISCHER, S. & OBERMAYER, B. The shape of barchan dunes. **Journal of Physics: Condensed Matter**, v. 17, n. 14, S1229, 2005.

KROY, K. & GUO, X. Comment on “relevant length scale of barchan dunes”. **Physical Review Letters**, v. 93, n. 3, 039401, 2004.

KROY, K.; SAUERMANN, G. & HERRMANN, H.J. Minimal model for aeolian sand dunes. **Physical Review E**, v. 66, n. 3, 031302, 2002a.

KROY, K.; SAUERMANN, G. & HERRMANN, H.J. Minimal model for sand dunes. **Physical Review Letters**, v. 88, n. 5, 054301, 2002b.

KUNDU, P.K.; DOWLING, D.R.; COHEN, I.M. & TRYGGVASON, G. **Fluid Mechanics**. Academic Press, the United States of America, 2016.

LAJEUNESSE, E.; MALVERTI, L. & CHARRU, F. Bed load transport in turbulent flow at the grain scale: Experiments and modeling. **Journal of Geophysical Research: Earth Surface**, v. 115, n. F4, F04001, 2010.

LÄMMEL, M.; RINGS, D. & KROY, K. A two-species continuum model for aeolian sand transport. **New Journal of Physics**, v. 14, n. 9, 093037, 2012.

LIU, D.; LIU, X.; FU, X. & WANG, G. Quantification of the bed load effects on turbulent open-channel flows. **Journal of Geophysical Research: Earth Surface**, v. 121, n. 4, 767–789, 2016.

MEYER-PETER, E. & MÜLLER, R. Formulas for bed-load transport. In **Proc. 2nd Meeting of International Association for Hydraulic Research**, pp. 39–64. 1948.

MOSER, R.D.; KIM, J. & MANSOUR, N.N. Direct numerical simulation of turbulent channel flow up to Reτ= 590. **Physics of Fluids**, v. 11, n. 4, 943–945, 1999.

NICOUD, F. & DUCROS, F. Subgrid-scale stress modelling based on the square of the velocity gradient tensor. **Flow, Turbulence and Combustion**, v. 62, n. 3, 183–200, 1999.

PÄHTZ, T. & DURÁN, O. Fluid forces or impacts: What governs the entrainment of soil particles in sediment transport mediated by a Newtonian fluid? **Physical Review Fluids**, v. 2, n. 7, 074303, 2017.

PÄHTZ, T.; KOK, J.F.; PARTELI, E.J.R. & HERRMANN, H.J. Flux saturation length of sediment transport. **Physical Review Letters**, v. 111, n. 21, 218002, 2013.

PARTELI, E.J.R.; ANDRADE, J.S. & HERRMANN, H.J. Transverse instability of dunes. **Physical Review Letters**, v. 107, n. 18, 188001, 2011.

PARTELI, E.J.R.; DURÁN, O.; BOURKE, M.C.; TSOAR, H.; PÖSCHEL, T. & HERRMANN, H. Origins of barchan dune asymmetry: Insights from numerical simulations. **Aeolian Research**, v. 12, 121–133, 2014.

PARTELI, E.J.R.; DURÁN, O. & HERRMANN, H.J. Minimal size of a barchan dune. **Physical Review E**, v. 75, n. 1, 011301, 2007.

PARTELI, E.J.R. & HERRMANN, H.J. Dune formation on the present Mars. **Physical Review E**, v. 76, n. 4, 041307, 2007.

PENTEADO, M.R.M. & FRANKLIN, E.M. Velocity fields of a bed-load layer under a turbulent liquid flow. **Experimental Thermal and Fluid Science**, v. 78, 220–228, 2016.

POPE, S.B. **Turbulent Flows**. Cambridge University Press, Cambridge, 2000.

PRANDTL, L. The mechanics of viscous fluids. **Aerodynamic Theory**, v. 3, 155–162, 1935.

ROSEBERRY, J.C.; SCHMEECKLE, M.W. & FURBISH, D.J. A probabilistic description of the bed load sediment flux: 2. Particle activity and motions. **Journal of Geophysical Research: Earth Surface**, v. 117, n. F3, F3032, 2012.

SAUERMANN, G. Modeling of wind blown sand and desert dunes. **Ph.D. Thesis, University of Stuttgart, Germany**, 2001.

SAUERMANN, G.; KROY, K. & HERRMANN, H.J. Continuum saltation model for sand dunes. **Physical Review E**, v. 64, n. 3, 031305, 2001.

SAUERMANN, G.; ROGNON, P.; POLIAKOV, A. & HERRMANN, H.J. The shape of the barchan dunes of Southern Morocco. **Geomorphology**, v. 36, n. 1-2, 47–62, 2000.

SCHAFLINGER, U.; ACRIVOS, A. & STIBI, H. An experimental study of viscous resuspension in a pressure-driven plane channel flow. **International Journal of Multiphase Flow**, v. 21, n. 4, 693–704, 1995.

SCHLICHTING, H. **Boundary-Layer Theory**. Springer, New York, 2000.

SCHMEECKLE, M.W. Numerical simulation of turbulence and sediment transport of medium sand. **Journal of Geophysical Research: Earth Surface**, v. 119, n. 6, 1240–1262, 2014.

SCHWÄMMLE, V. & HERRMANN, H. A model of barchan dunes including lateral shear stress. **The European Physical Journal E**, v. 16, n. 1, 57–65, 2005.

SEIZILLES, G.; LAJEUNESSE, E.; DEVAUCHELLE, O. & BAK, M. Cross-stream diffusion in bedload transport. **Physics of Fluids**, v. 26, n. 1, 013302, 2014.

SHIELDS, A. Anwendung der Ahnlichkeitsmechanik und der Turbulenzforschung auf die

Geschiebebewegung. **Mitteilungen der Preussischen Versuchsanstalt fur Wasserbau und Schiffbau**, v. 26, n. 3, 5–24, 1936.

SMAGORINSKY, J. General circulation model of the atmosphere. **Mon. Weather Rev**, v. 91, 99–164, 1963.

SOTIROPOULOS, F. & KHOSRONEJAD, A. Sand waves in environmental flows: Insights gained by coupling large-eddy simulation with morphodynamics. **Physics of Fluids**, v. 28, n. 2, 021301, 2016.

STEVENSON, P.; THORPE, R.; KENNEDY, J. & MCDERMOTT, C. The transport of particles at low loading in near-horizontal pipes by intermittent flow. **Chemical Engineering Science**, v. 56, n. 6, 2149–2159, 2001.

SUN, R. & XIAO, H. SediFoam: A general-purpose, open-source CFD-DEM solver for particle-laden flow with emphasis on sediment transport. **Computers & Geosciences**, v. 89, 207–219, 2016.

TSUJI, Y.; KAWAGUCHI, T. & TANAKA, T. Discrete particle simulation of two-dimensional fluidized bed. **Powder Technology**, v. 77, n. 1, 79–87, 1993.

TSUJI, Y.; TANAKA, T. & ISHIDA, T. Lagrangian numerical simulation of plug flow of cohesionless particles in a horizontal pipe. **Powder Technology**, v. 71, n. 3, 239–250, 1992.

WANG, C. & ANDERSON, W. Large-eddy simulation of turbulent flow over spanwise-offset barchan dunes: Interdune vortex stretching drives asymmetric erosion. **Physical Review E**, v. 98, n. 3, 033112, 2018.

WHITE, F. **Viscous Fluid Flow**, v. 3. McGraw-Hill, New York, 2006.

ZHANG, D.; YANG, X.; ROZIER, O. & NARTEAU, C. Mean sediment residence time in barchan dunes. **Journal of Geophysical Research: Earth Surface**, v. 119, n. 3, 451–463, 2014.

ZHOU, Z.Y.; KUANG, S.B.; CHU, K.W. & YU, A.B. Discrete particle simulation of particle–fluid flow: model formulations and their applicability. **Journal of Fluid Mechanics**, v. 661, 482–510, 2010.

ANNEX A – List of publications

Publications:

Alvarez, C.A. and Franklin, E.M. Shape evolution of numerically obtained subaqueous barchans. **Physical Review E**, v. 101, 012905, 2020.

Alvarez, C.A and Franklin, E.M. Horns of subaqueous barchan dunes: A study at the grain scale. **Physical Review E**, v. 100, 042904, 2019.

Alvarez, C.A. and Franklin, E.M. Role of transverse displacements in the formation of subaqueous barchan dunes. **Physical Review Letters**, v. 121, 164503, 2018.

Alvarez, C.A. and Franklin, E.M. Birth of a subaqueous barchan dune. **Physical Review E**, v. 96, 062906, 2017.

Conference Proceedings and Abstracts:

Alvarez, C.A. and Franklin, E.M. Bed-load characteristics over evolving and developed subaqueous barchan dunes. **Bulletin of the American Physical Society Division of Fluid Dynamics Meeting**, Seattle, USA, 2019.

Alvarez, C.A. and Franklin, E.M. Genesis of barchan dunes: Subaqueous case. **São Paulo School of Advanced Sciences on Nonlinear Dynamics**, São Paulo, Brazil, 2019.

Alvarez, C.A. and Franklin, E.M. A description at the grain scale of the growth of barchan dunes. **10th International Conference on Multiphase Flow - ICMF2019**, Rio de Janeiro, Brazil, 2019.

Alvarez, C.A. and Franklin, E.M. Characteristic times for the formation of subaqueous barchan dunes. **12th European Fluid Mechanics Conference - EFMC12**, Vienna, Austria, 2018.

Alvarez, C.A. and Franklin, E.M. Morphology of subaqueous barchan dunes in turbulent shear flows. **17th Brazilian Congress of Thermal Sciences and Engineering - ENCIT2018**, Águas de Lindóia, Brazil, 2018.

Alvarez, C.A. and Franklin, E.M. Formation and morphology of subaqueous barchan dunes. **24th ABCM International Congress of Mechanical Engineering - COBEM2017**, Curitiba, Brazil, 2017.

Franklin, E.M. and Alvarez, C.A. The growth and equilibrium of barchan dunes. **Bulletin of the American Physical Society Division of Fluid Dynamics Meeting**, Denver, USA, 2017.

Alvarez, C.A. and Franklin, E.M. Experimental study on the formation of subaqueous barchan dunes in closed conduits. **Experimental Fluid Mechanics - EFM2017**, Mikulov, Czech Republic, 2017.

Alvarez, C.A. and Franklin, E.M. Experimental study on the formation of barchan dunes in closed conduits. **9th World Conference on Experimental Heat Transfer, Fluid Mechanics and Thermodynamics - ExHFT9**, Foz do Iguaçú, Brazil, 2017.

APPENDIX A – Supplementary material of Chapter 3†

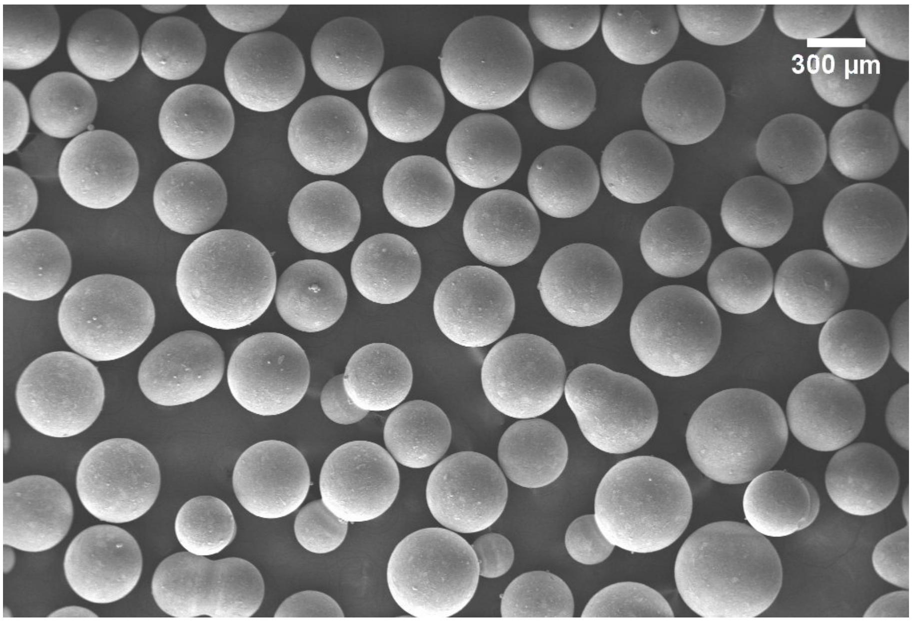

Fig. A.1: Image of scanning electron microscopy for the 0.25 mm $\leq d \leq$ 0.50 mm round glass beads.

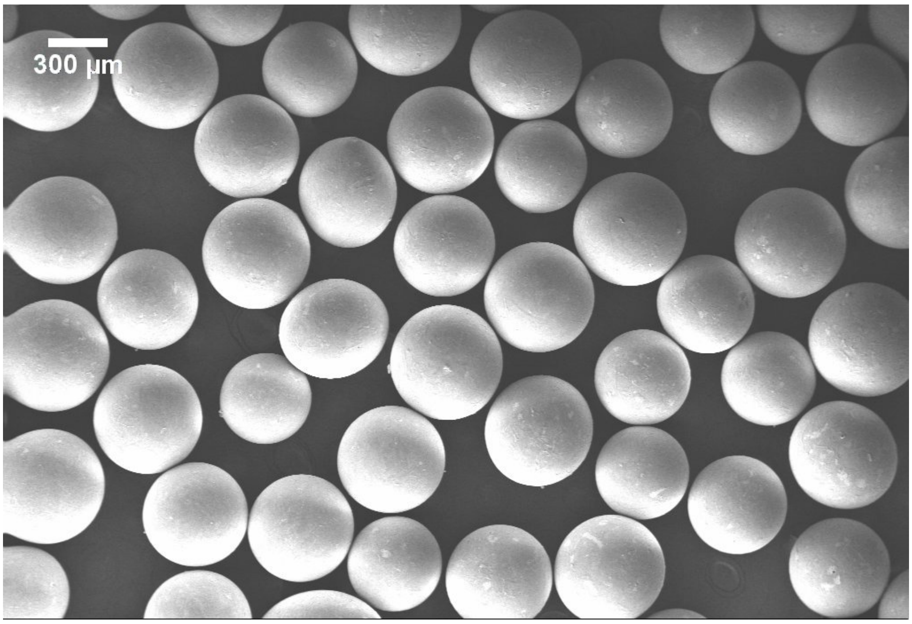

Fig. A.2: Image of scanning electron microscopy for the 0.40 mm $\leq d \leq$ 0.60 mm round glass beads.

† The information presented in this appendix was extracted from the Supplemental Material of C. A. Alvarez and E. M. Franklin, Phys. Rev. E. 96, 062906 (2017). (Alvarez & Franklin, 2017a)

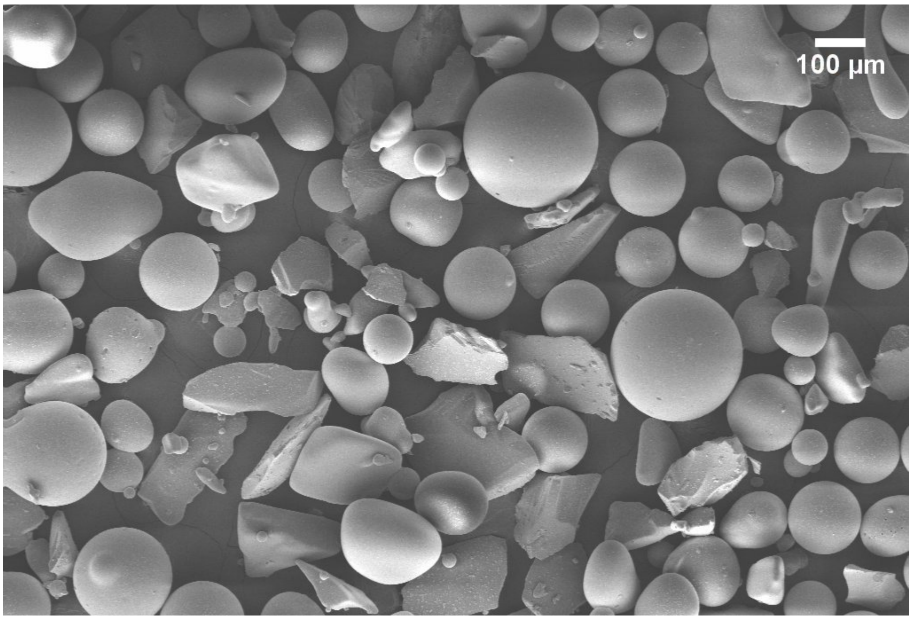

Fig. A.3: Image of scanning electron microscopy for the 0.21 mm $\leq d \leq$ 0.30 mm angular glass beads.

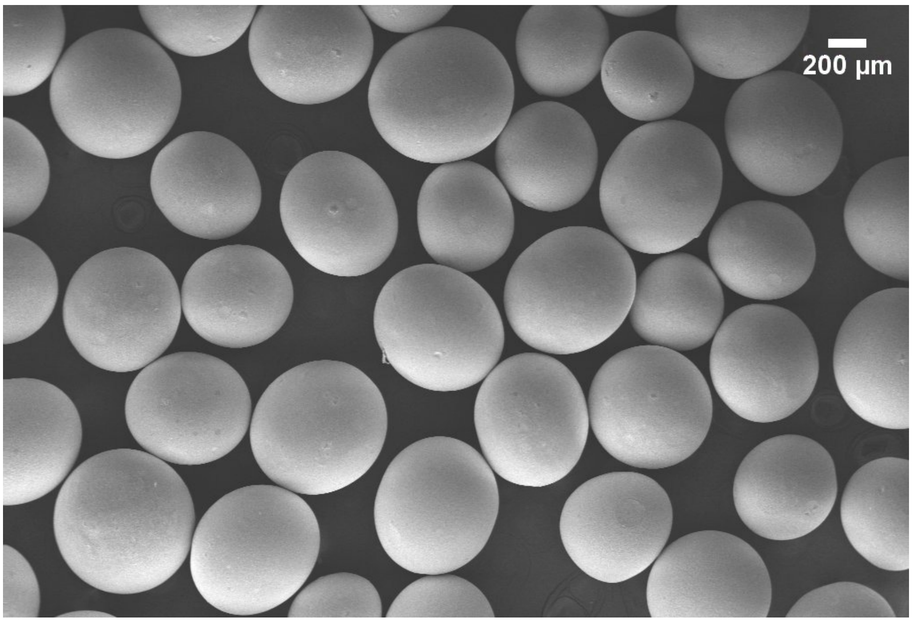

Fig. A.4: Image of scanning electron microscopy for the 0.40 mm $\leq d \leq$ 0.60 mm round zirconium beads.

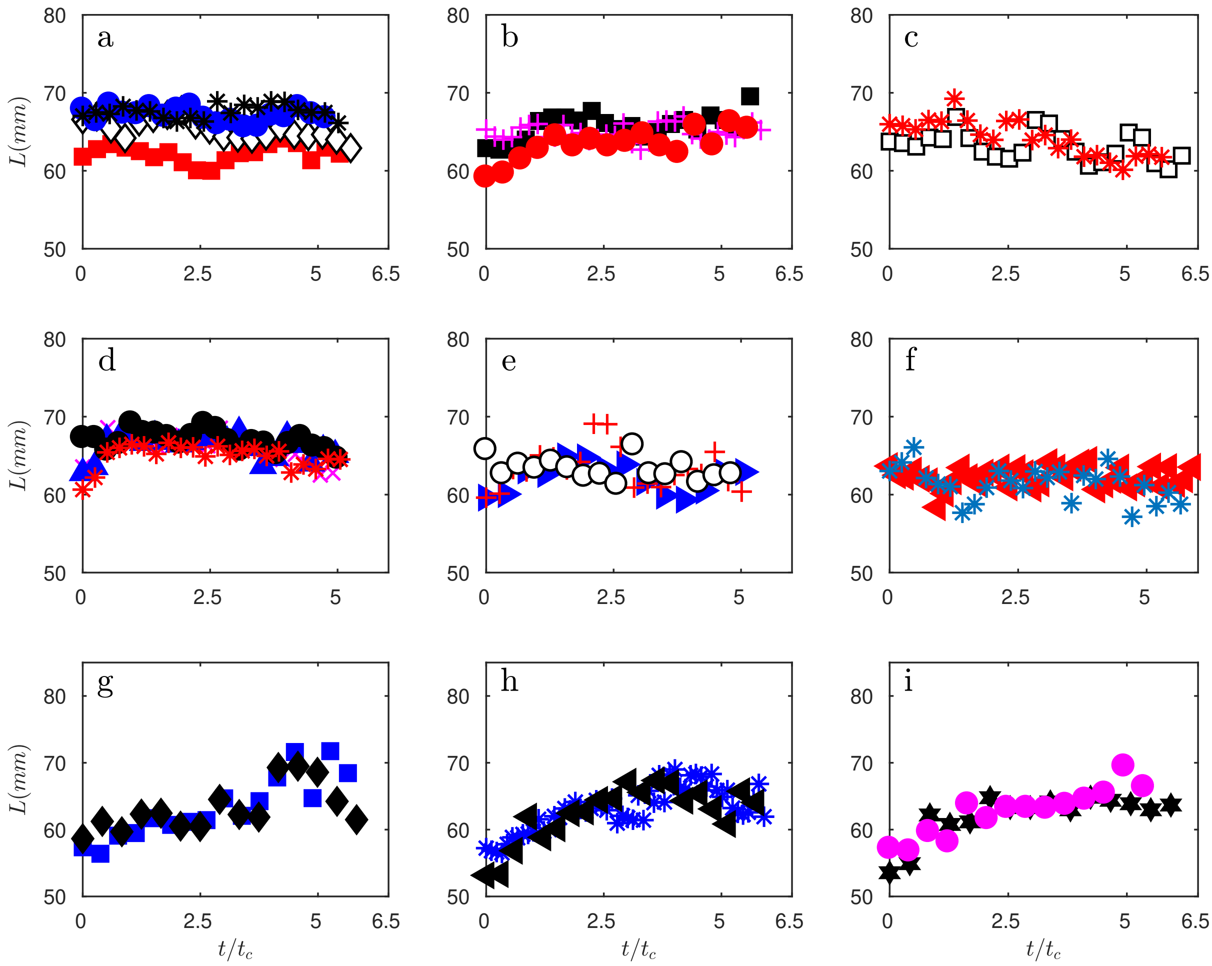

Fig. A.5: L versus t/t_c for glass beads under different flow conditions. The cases listed in the key are presented in Table 3.1, and each different symbol in each graphic corresponds to a different test run. This figure presents every n measurements for each experimental condition, where $5 \leq n \leq 15$.

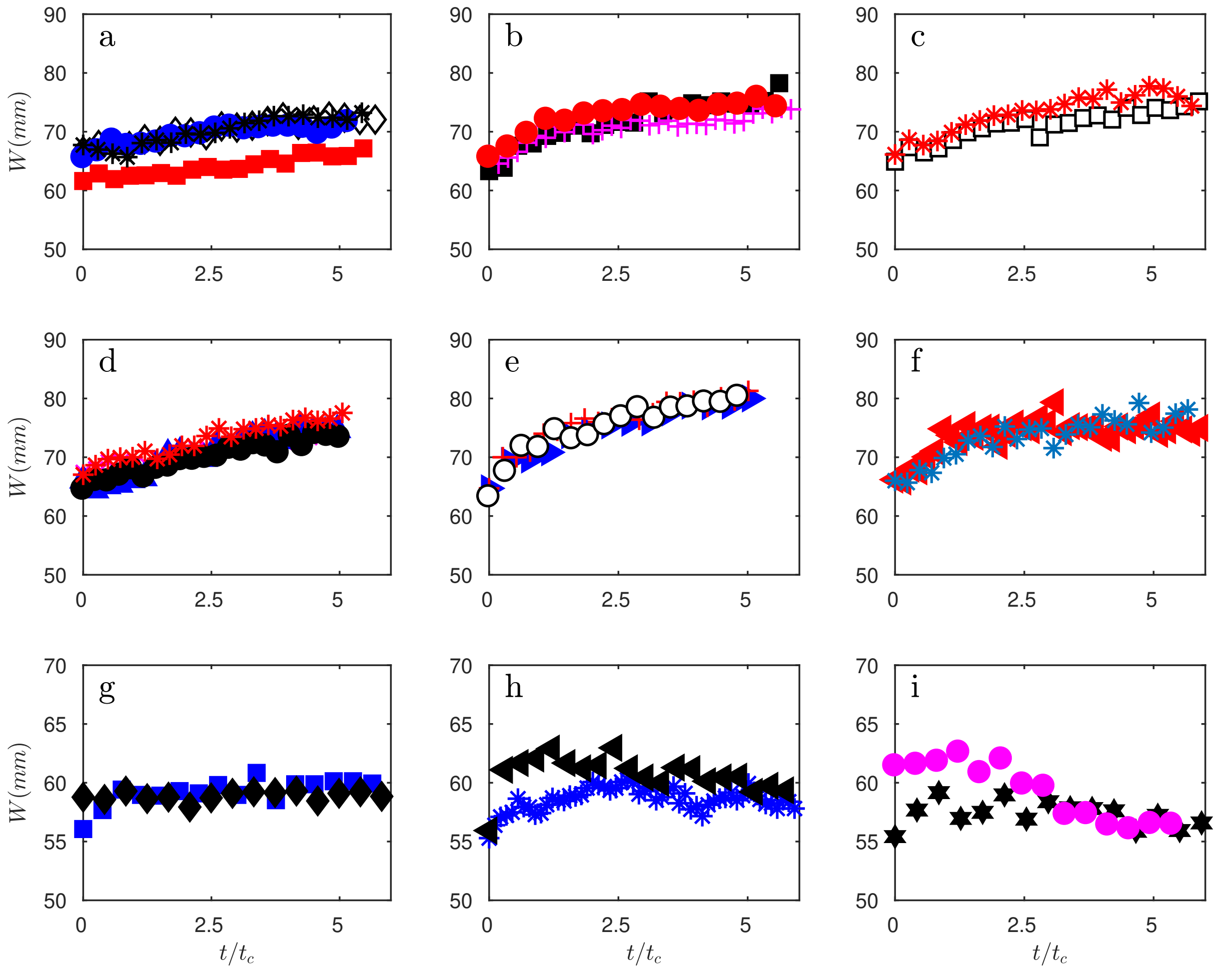

Fig. A.6: W versus t/t_c for glass beads under different flow conditions. The cases listed in the key are presented in Table 3.1, and each different symbol in each graphic corresponds to a different test run. This figure presents every n measurements for each experimental condition, where $5 \leq n \leq 15$.

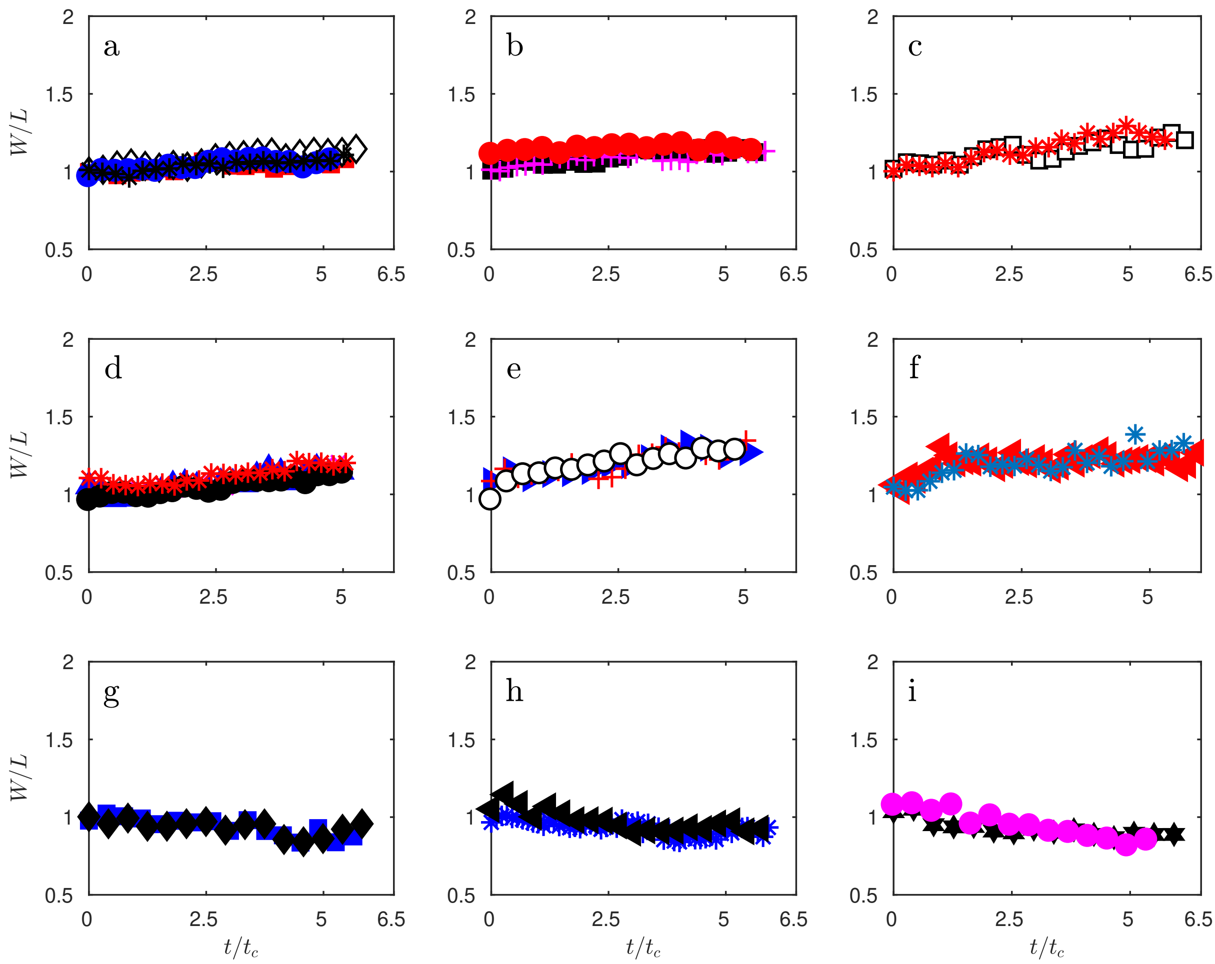

Fig. A.7: W/L versus t/t_c for glass beads under different flow conditions. The cases listed in the key are presented in Table 3.1, and each different symbol in each graphic corresponds to a different test run. This figure presents every n measurements for each experimental condition, where $5 \leq n \leq 15$.

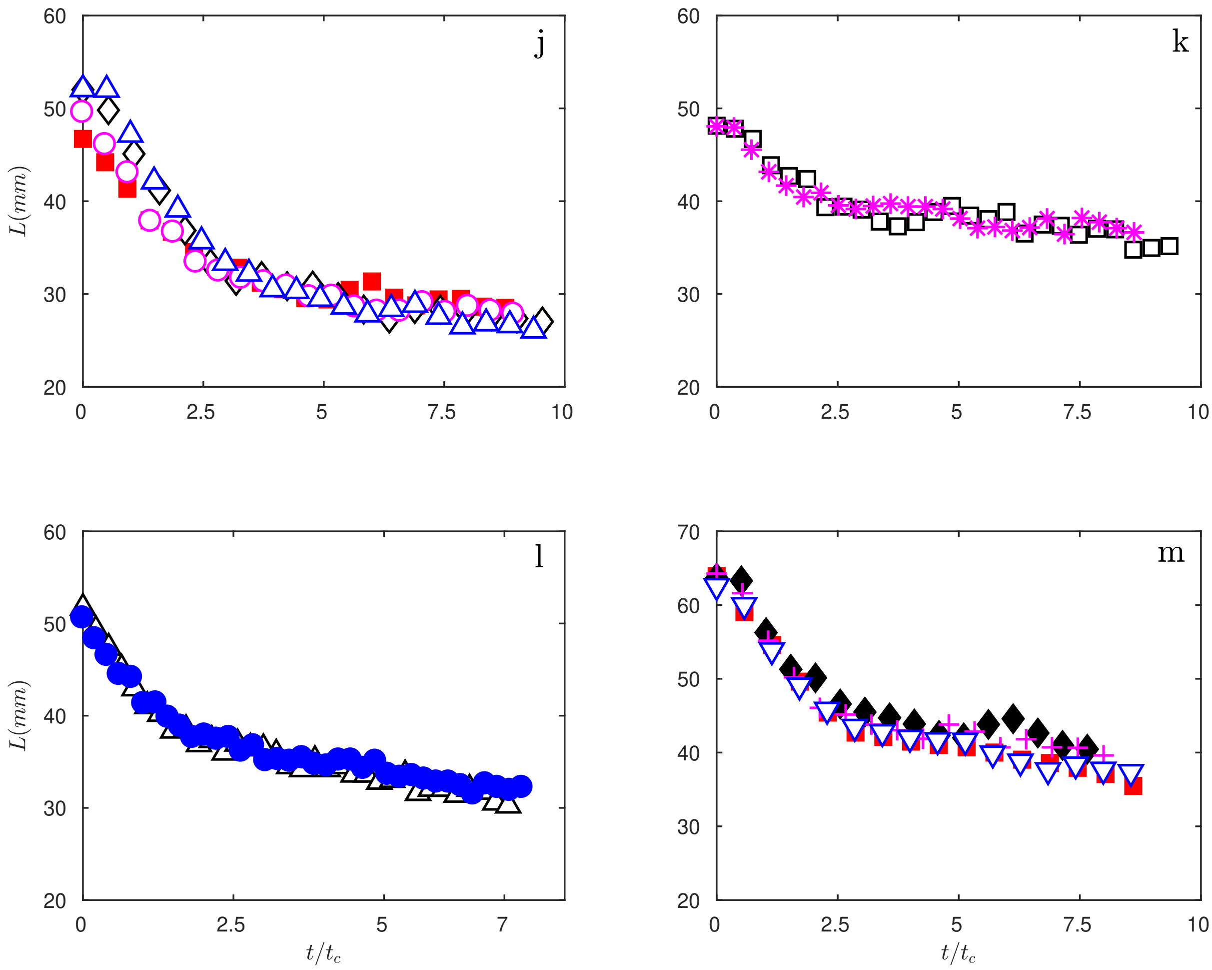

Fig. A.8: L versus t/t_c for zirconium beads under different flow conditions. The cases listed in the key are presented in Table 3.1, and each different symbol in each graphic corresponds to a different test run. This figure presents every n measurements for each experimental condition, where $5 \leq n \leq 15$.

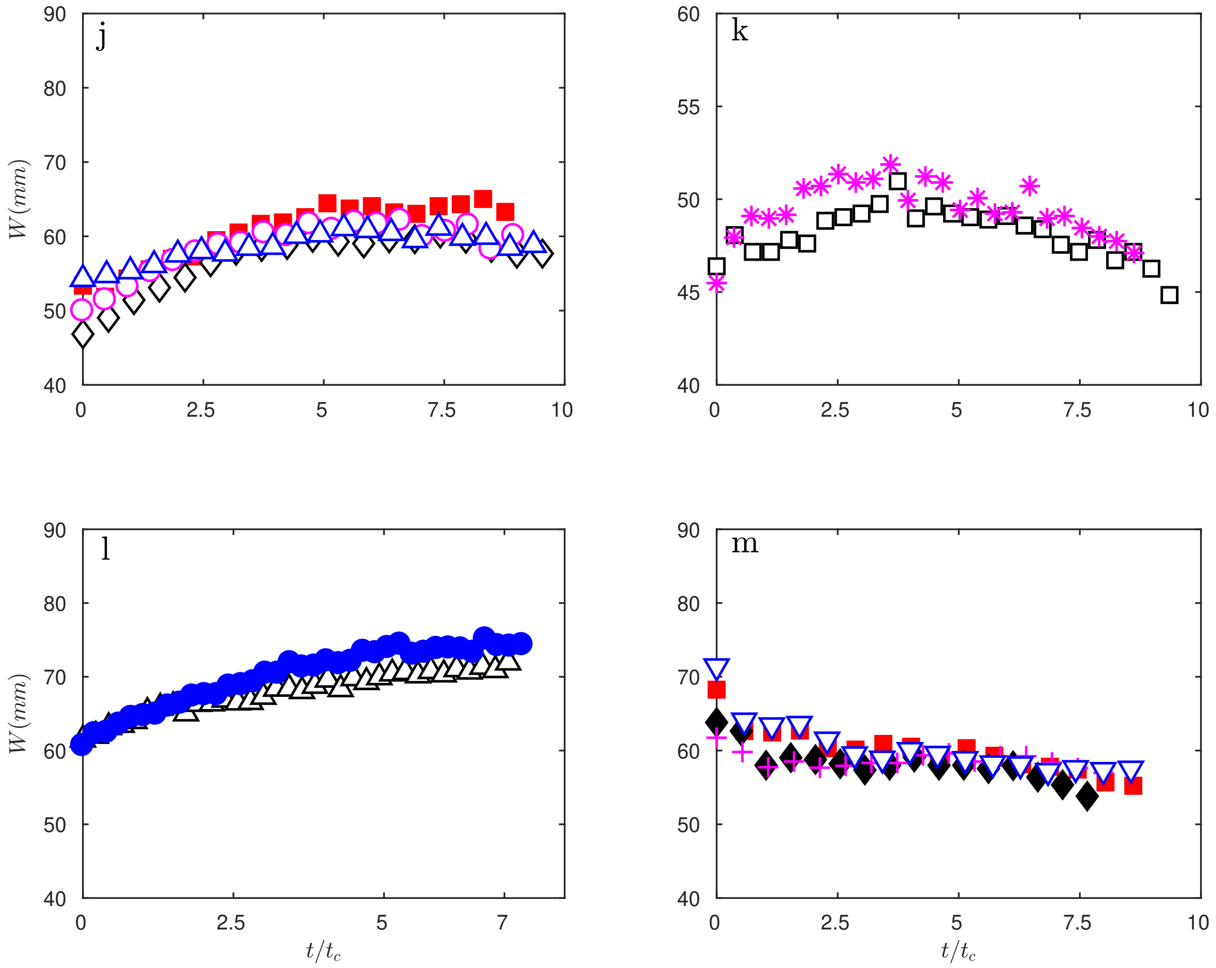

Fig. A.9: W versus t/t_c for zirconium beads under different flow conditions. The cases listed in the key are presented in Table 3.1, and each different symbol in each graphic corresponds to a different test run. This figure presents every n measurements for each experimental condition, where $5 \leq n \leq 15$.

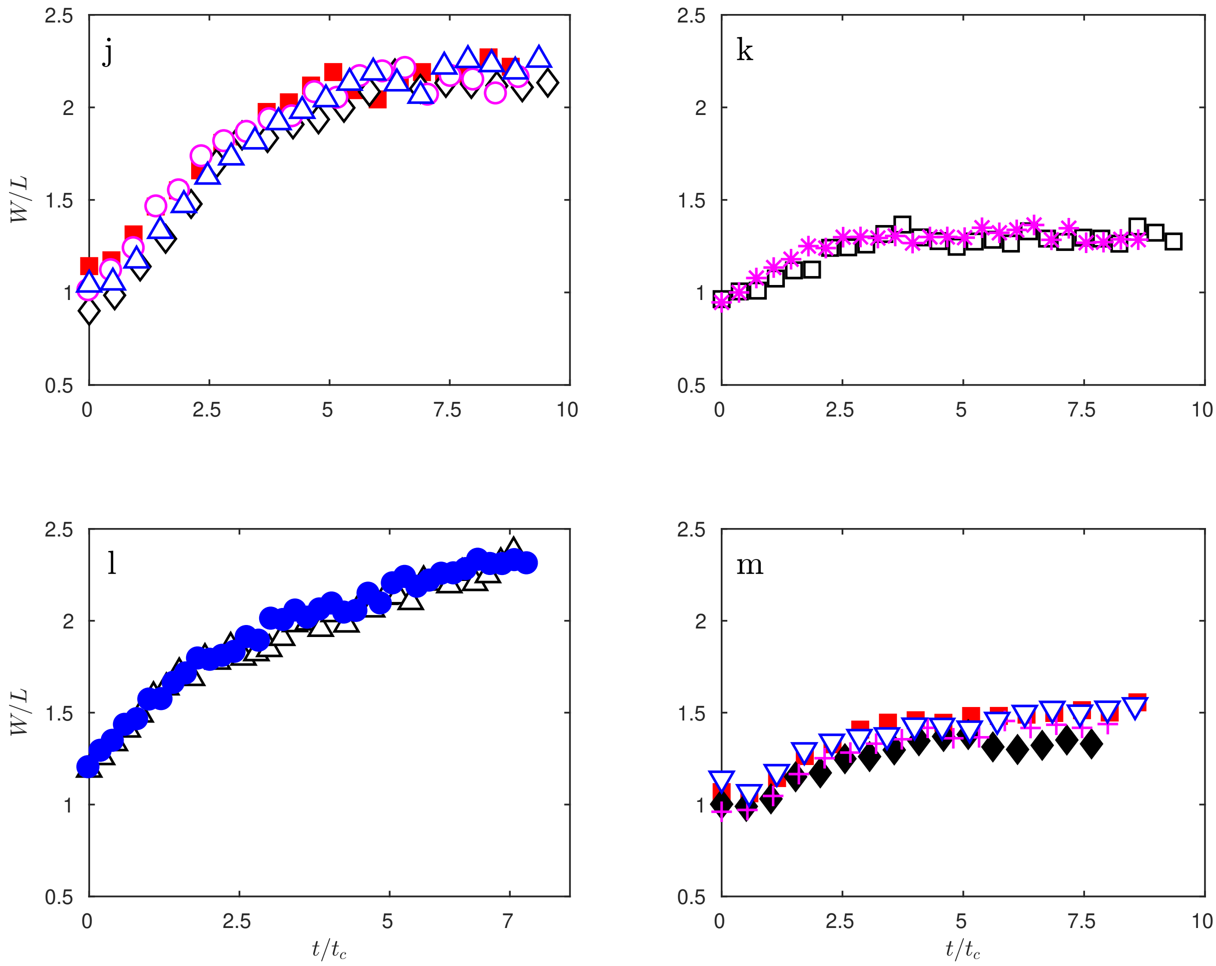

Fig. A.10: W/L versus t/t_c for zirconium beads under different flow conditions. The cases listed in the key are presented in Table 3.1, and each different symbol in each graphic corresponds to a different test run. This figure presents every n measurements for each experimental condition, where $5 \leq n \leq 15$.

APPENDIX B – Supplementary material of Chapter 4†

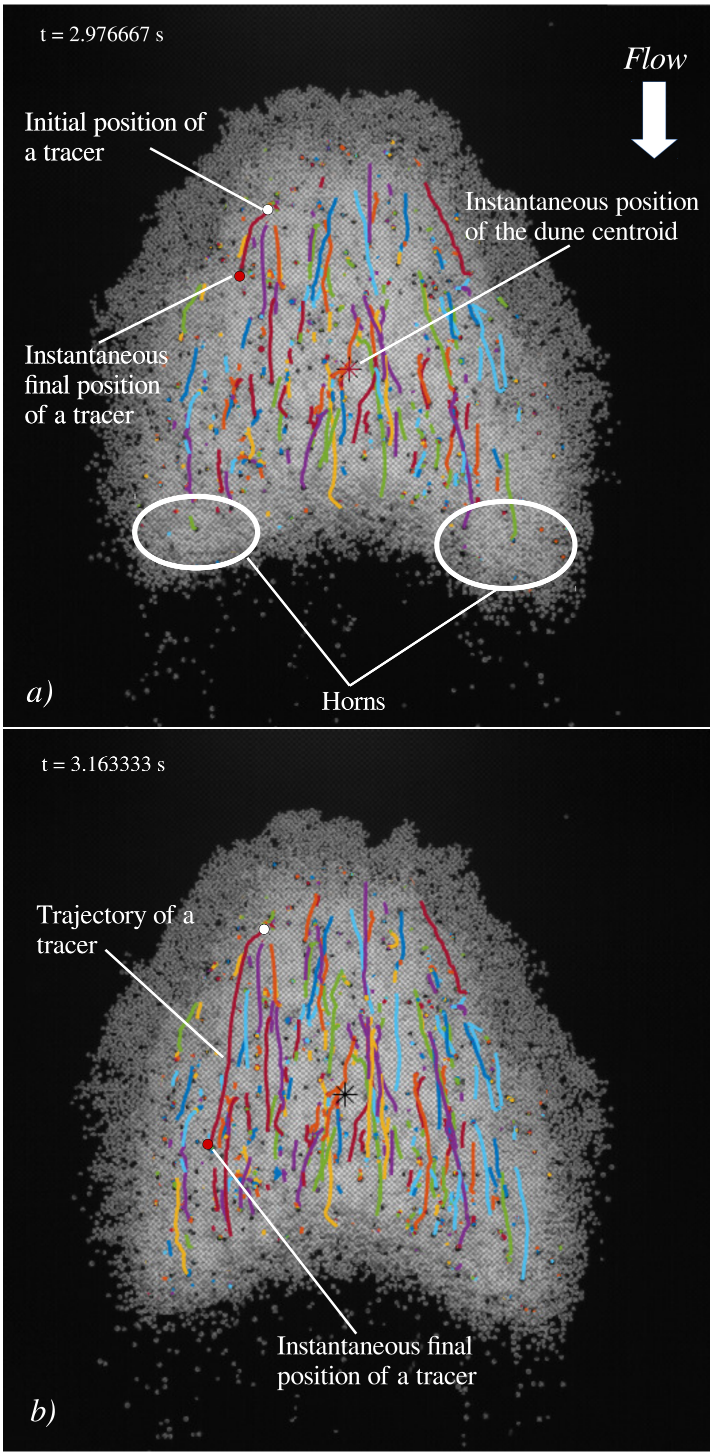

Fig. B.1: Some pathlines of tracers over a developed barchan made of 0.40 mm $\leq d \leq$ 0.60 mm glass beads superposed with a photograph of the barchan for (a) t = 2.98 s and (b) t = 3.16 s. The water flow is from top to bottom. $Re = 1.82 \times 10^4$ and the heap initial mass was 6.2 g.

† Parts of this appendix were extracted from Supplemental Materials of C. A. Alvarez and E. M. Franklin, Phys. Rev. Lett. 121, 164503 (2018), and of C. A. Alvarez and E. M. Franklin, Phys. Rev. E 100, 042904 (2019). (Alvarez & Franklin, 2018b, 2019)

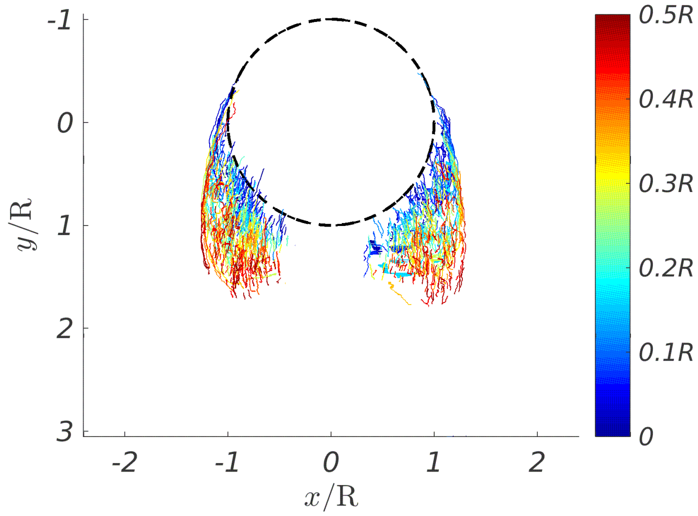

Fig. B.2: Pathlines of tracers that migrated to horns of a evolving barchan made of 0.15 mm $\leq d \leq$ 0.25 mm glass beads. The water flow is from top to bottom. Re = 1.21×10^4 and the heap initial mass was 6.2 g.

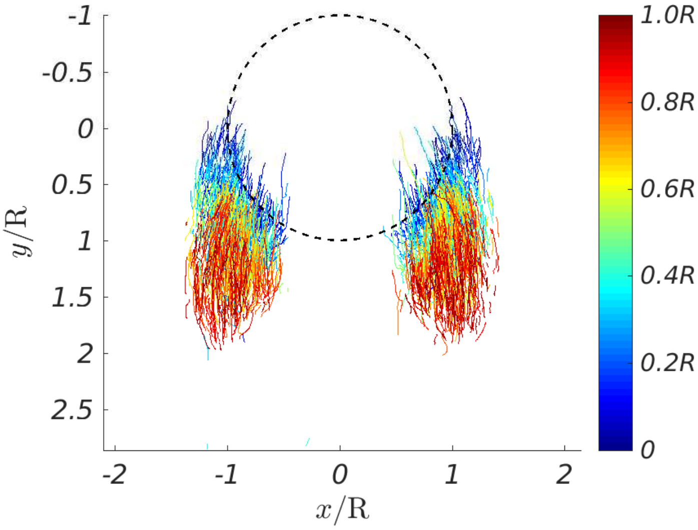

Fig. B.3: Pathlines of tracers that migrated to horns of a evolving barchan made of 0.15 mm $\leq d \leq$ 0.25 mm glass beads. The water flow is from top to bottom. Re = 1.47×10^4 and the heap initial mass was 6.2 g.

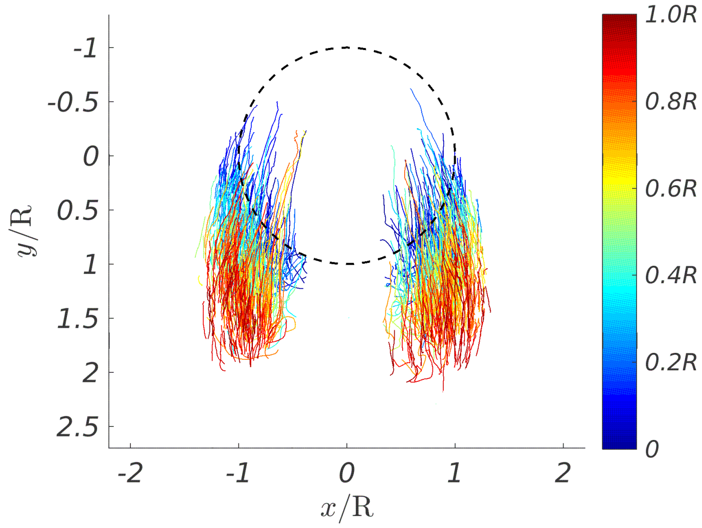

Fig. B.4: Pathlines of tracers that migrated to horns of a evolving barchan made of 0.15 mm $\leq d \leq$ 0.25 mm glass beads. The water flow is from top to bottom. Re = 1.82×10^4 and the heap initial mass was 6.2 g.

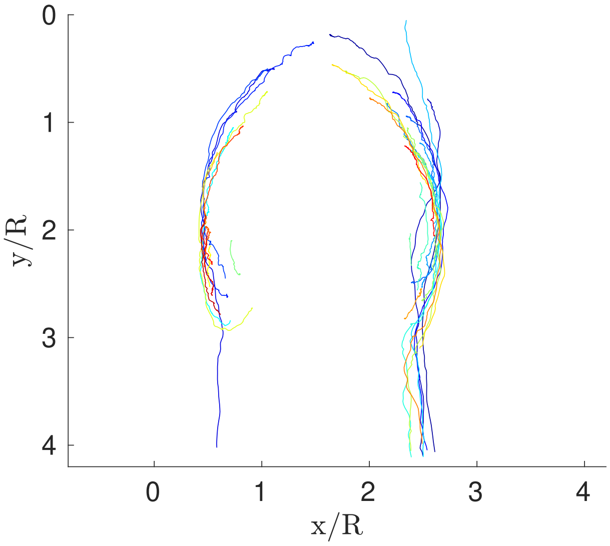

Fig. B.5: Pathlines of tracers that migrated to horns of a evolving barchan made of 0.40 mm $\leq d \leq$ 0.60 mm glass beads. The water flow is from top to bottom. Re = 1.21×10^4 and the heap initial mass was 6.2 g.

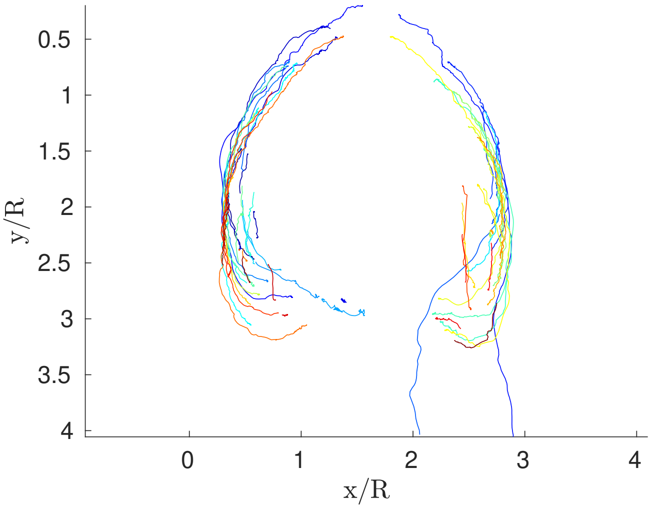

Fig. B.6: Pathlines of tracers that migrated to horns of a evolving barchan made of 0.40 mm $\leq d \leq$ 0.60 mm glass beads. The water flow is from top to bottom. Re = 1.21×10^4 and the heap initial mass was 10.3 g.

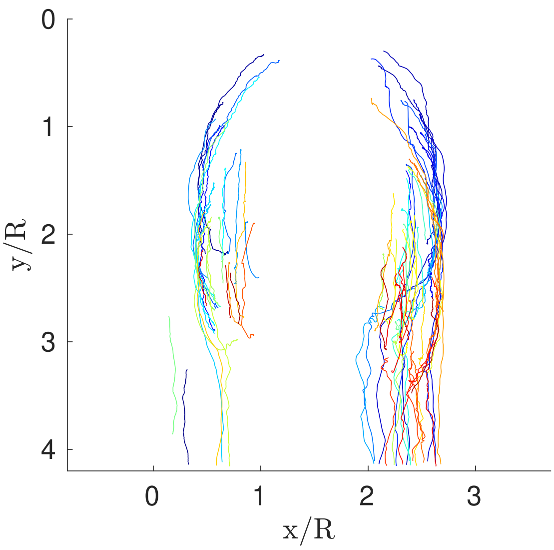

Fig. B.7: Pathlines of tracers that migrated to horns of a evolving barchan made of 0.40 mm $\leq d \leq$ 0.60 mm glass beads. The water flow is from top to bottom. Re = 1.47×10^4 and the heap initial mass was 6.2 g.

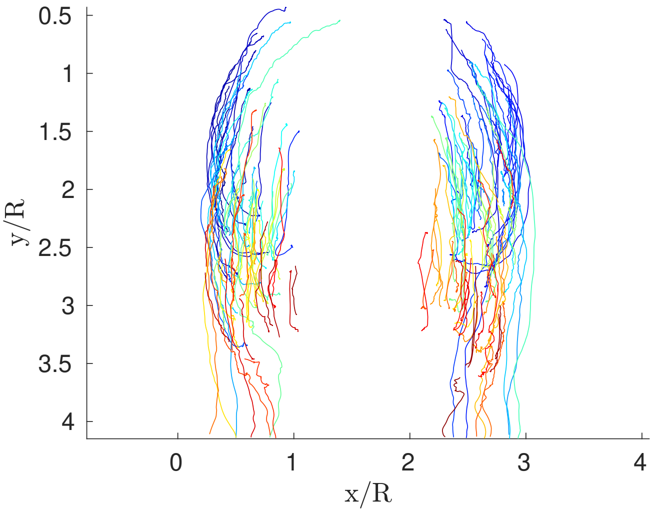

Fig. B.8: Pathlines of tracers that migrated to horns of a evolving barchan made of 0.40 mm $\leq\ d\ \leq$ 0.60 mm glass beads. The water flow is from top to bottom. Re = 1.47×10^4 and the heap initial mass was 10.3 g.

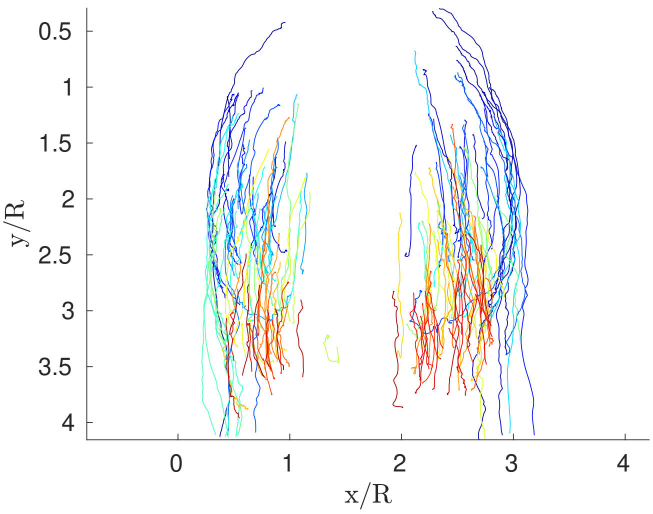

Fig. B.9: Pathlines of tracers that migrated to horns of a evolving barchan made of 0.40 mm $\leq\ d\ \leq$ 0.60 mm glass beads. The water flow is from top to bottom. Re = 1.82×10^4 and the heap initial mass was 10.3 g.

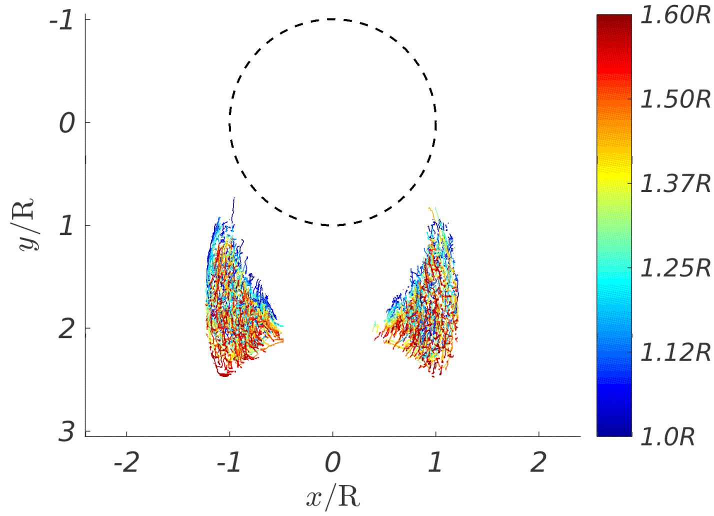

Fig. B.10: Pathlines of tracers that migrated to horns of a developed barchan made of 0.15 mm $\leq$ d $\leq$ 0.25 mm glass beads. The water flow is from top to bottom. Re = 1.21×10^4 and the heap initial mass was 6.2 g.

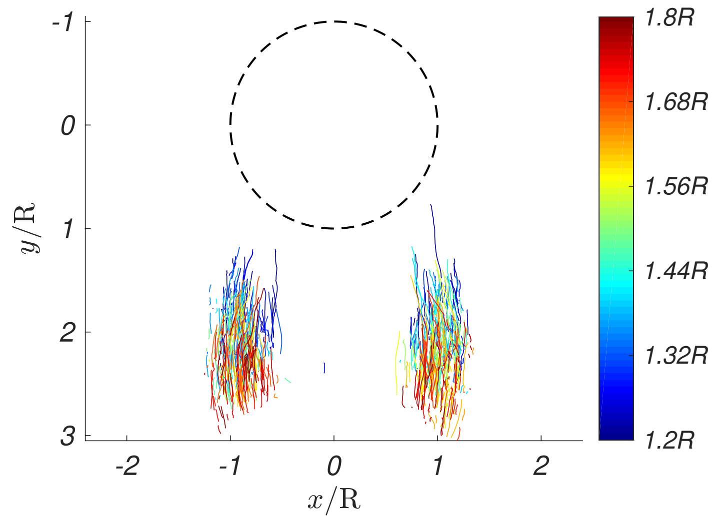

Fig. B.11: Pathlines of tracers that migrated to horns of a developed barchan made of 0.15 mm $\leq$ d $\leq$ 0.25 mm glass beads. The water flow is from top to bottom. Re = 1.47×10^4 and the heap initial mass was 6.2 g.

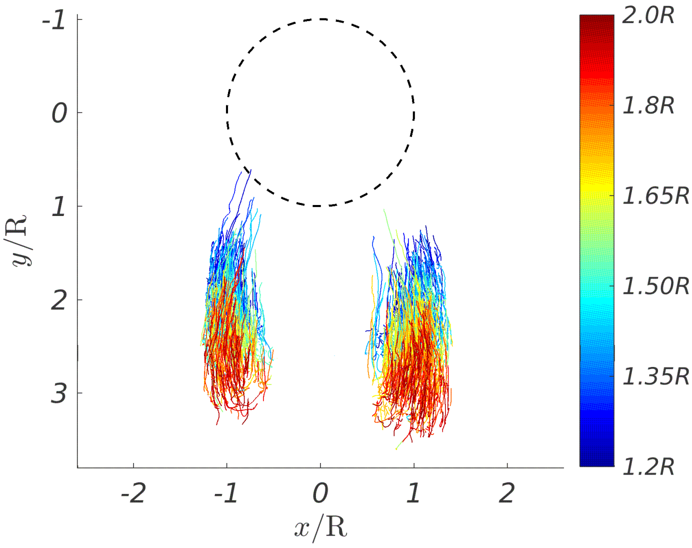

Fig. B.12: Pathlines of tracers that migrated to horns of a developed barchan made of 0.15 mm $\leq d \leq$ 0.25 mm glass beads. The water flow is from top to bottom. Re = 1.82×10^4 and the heap initial mass was 6.2 g.

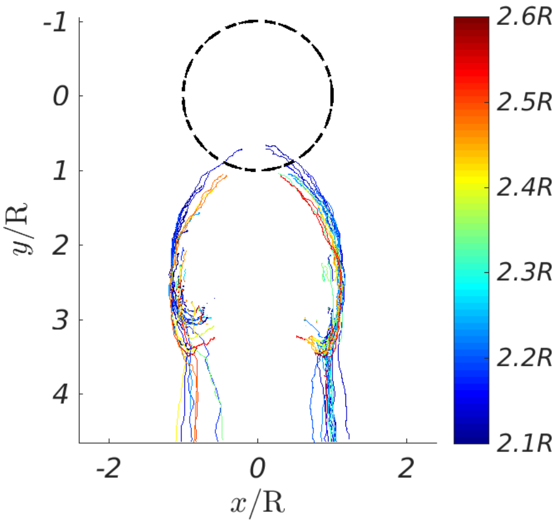

Fig. B.13: Pathlines of tracers that migrated to horns of a developed barchan made of 0.40 mm $\leq d \leq$ 0.60 mm glass beads. The water flow is from top to bottom. Re = 1.21×10^4 and the heap initial mass was 6.2 g.

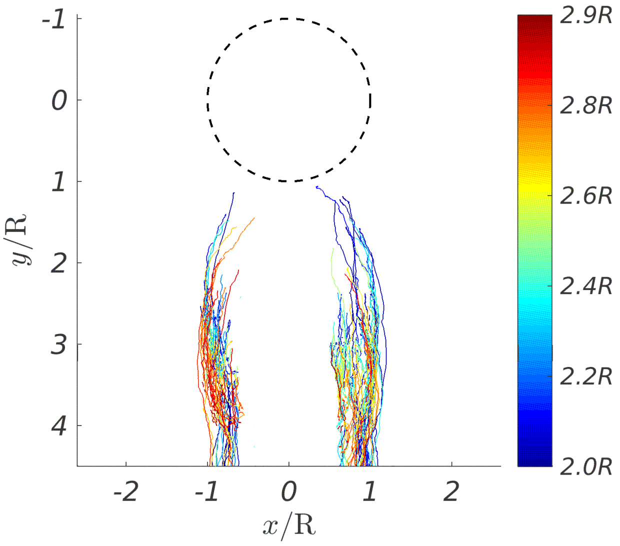

Fig. B.14: Pathlines of tracers that migrated to horns of a developed barchan made of 0.40 mm $\leq d \leq$ 0.60 mm glass beads. The water flow is from top to bottom. Re = 1.47×10^4 and the heap initial mass was 6.2 g.

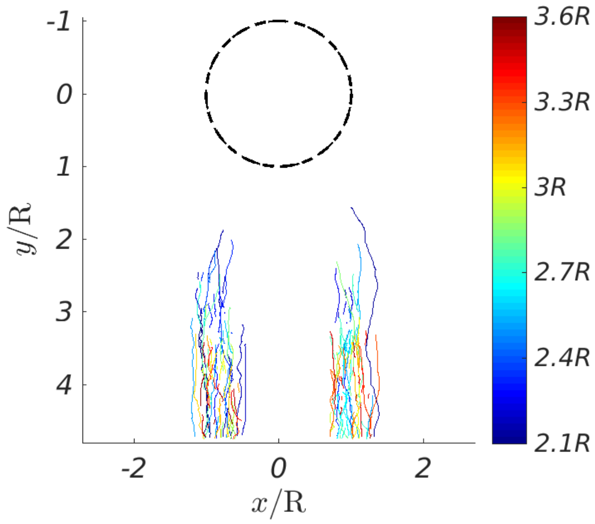

Fig. B.15: Pathlines of tracers that migrated to horns of a developed barchan made of 0.40 mm $\leq d \leq$ 0.60 mm glass beads. The water flow is from top to bottom. Re = 1.82×10^4 and the heap initial mass was 6.2 g.

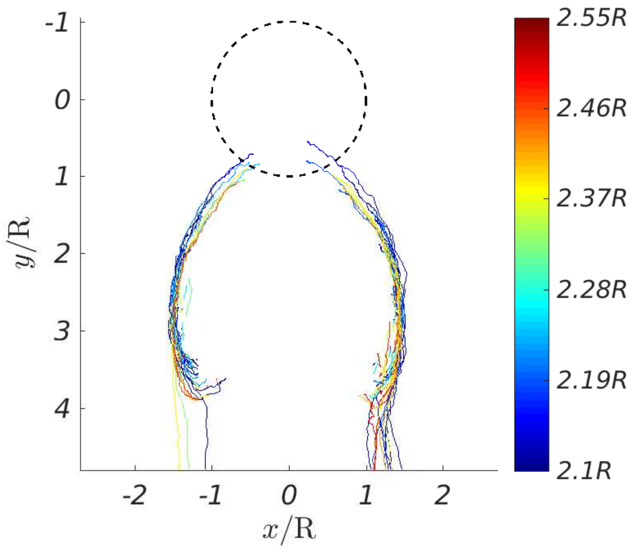

Fig. B.16: Pathlines of tracers that migrated to horns of a developed barchan made of 0.40 mm $\leq d \leq$ 0.60 mm glass beads. The water flow is from top to bottom. Re = 1.21×10^4 and the heap initial mass was 10.3 g.

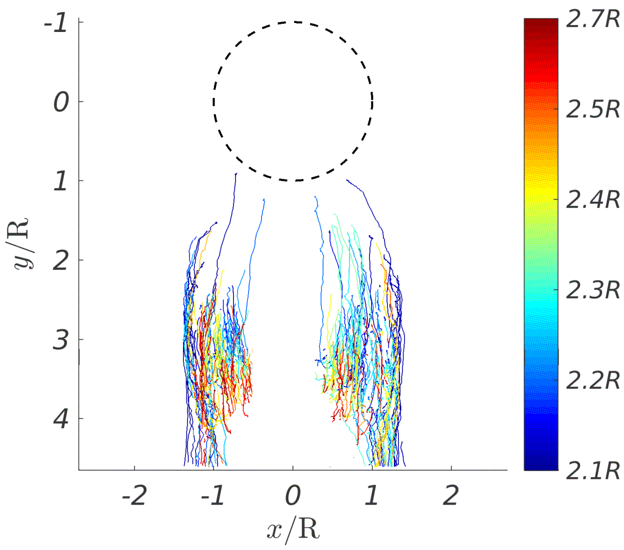

Fig. B.17: Pathlines of tracers that migrated to horns of a developed barchan made of 0.40 mm $\leq d \leq$ 0.60 mm glass beads. The water flow is from top to bottom. Re = 1.47×10^4 and the heap initial mass was 10.3 g.

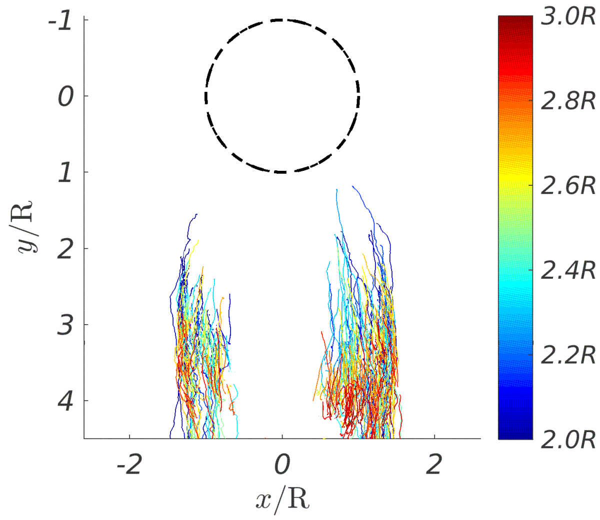

Fig. B.18: Pathlines of tracers that migrated to horns of a developed barchan made of 0.40 mm $\leq d \leq$ 0.60 mm glass beads. The water flow is from top to bottom. Re = 1.82×10^4 and the heap initial mass was 10.3 g.